12-14-2017 1:30 PM

Polarimetric Synthetic Aperture Radar (SAR) Application for Geological Mapping and Resource Exploration in the Canadian Arctic

Byung-Hun Choe
The University of Western Ontario

Supervisor
Osinski, Gordon R.
The University of Western Ontario Co-Supervisor
Neish, Catherine D.
The University of Western Ontario Co-Supervisor
Tornabene, Livio L.
The University of Western Ontario

Graduate Program in Geology
A thesis submitted in partial fulfillment of the requirements for the degree in Doctor of Philosophy

Abstract

The role of remote sensing in geological mapping has been rapidly growing by providing predictive maps in advance of field surveys. Remote predictive maps with broad spatial coverage have been produced for northern Canada and the Canadian Arctic which are typically very difficult to access. Multi and hyperspectral airborne and spaceborne sensors are widely used for geological mapping as spectral characteristics are able to constrain the minerals and rocks that are present in a target region. Rock surfaces in the Canadian Arctic are altered by extensive glacial activity and freeze-thaw weathering, and form different surface roughnesses depending on rock type. Different physical surface properties, such as surface roughness and soil moisture, can be revealed by distinct radar backscattering signatures at different polarizations. This thesis aims to provide a multidisciplinary approach for remote predictive mapping that integrates the lithological and physical surface properties of target rocks. This work investigates the physical surface properties of geological units in the Tunnunik and Haughton impact structures in the Canadian Arctic characterized by polarimetric synthetic aperture radar (SAR). It relates the radar scattering mechanisms of target surfaces to their lithological compositions from multispectral analysis for remote predictive geological mapping in the Canadian Arctic. This work quantitatively estimates the surface roughness relative to the transmitted radar wavelength and volumetric soil moisture by radar scattering model inversion. The SAR polarization signatures of different geological units were also characterized, which showed a significant correlation with their surface roughness. This work presents a modified radar scattering model for weathered rock surfaces. More broadly, it presents an integrative remote predictive mapping algorithm by combining multispectral and polarimetric SAR parameters.

Keywords

Polarimetric SAR, physical surface properties, radar scattering mechanism, surface parameter inversion, polarization signature, multispectral analysis, remote predictive geological mapping, meteorite impact structures, Canadian Arctic.

Co-Authorship Statement

Chapter 2. Remote predictive mapping of the Tunnunik impact structure in the Canadian Arctic using multispectral and polarimetric SAR data fusion: All data were collected and processed by Byung-Hun Choe and Dr. Livio L. Tornabene. The manuscript was written by Byung-Hun Choe. Dr. Livio L. Tornabene, Dr. Gordon R. Osinski, and Jennifer D. Newman contributed to interpretations on image processing and sample collection and analysis, and provided editorial suggestions and comments. It is currently in revision in *Canadian Journal of Remote Sensing* for publication titled 'Remote predictive mapping of the Tunnunik impact structure in the Canadian Arctic using multispectral and polarimetric SAR data fusion'.

Chapter 3. A modified semi-empirical radar scattering model for weathered rock surfaces: All data were collected and processed by Byung-Hun Choe, and the manuscript was written by Byung-Hun Choe. Dr. Gordon R. Osinski, Dr. Catherine D. Neish, and Dr. Livio L. Tornabene contributed to interpretations with editorial suggestions and comments. It is currently in preparation to be submitted to *IEEE Transactions on Geoscience and Remote Sensing* for publication titled 'A modified semi-empirical radar scattering model for weathered rock surfaces'.

Chapter 4. Polarimetric SAR signatures for characterizing geological units in the Canadian Arctic: All data were collected and processed by Byung-Hun Choe, and the manuscript was written by Byung-Hun Choe. Dr. Gordon R. Osinski, Dr. Catherine D. Neish, and Dr. Livio L. Tornabene contributed to interpretations with editorial suggestions and comments. It is currently in preparation to be submitted to *IEEE Transactions on Geoscience* *and Remote Sensing* for publication titled ‘Polarimetric SAR signatures for characterizing geological units in the Canadian Arctic’.

Dedication

I can do all this through him who gives me strength.

-Philippians 4:13-

Acknowledgments

Now I finally have a chance to thank my amazing supervisors for their encouragement and support throughout my Ph. D. study. First of all, I am grateful to Dr. Gordon Osinski for bring me into the Canadian Arctic and impact cratering studies. Dr. Catherine Neish, thank you for infecting me with her RADAR love. My little RADAR background could be advanced through insightful discussions with her. Dr. Livio Tornabene, thank you for guiding and teaching me multispectral remote sensing from the bottom up. They are really a perfect combination for my thesis. Also, I need to gratefully acknowledge the financial and logistical supports for this work provided by Canadian Space Agency (CSA) through Science Operational Applications Research (SOAR), Natural Resource Canada (NRCan) through Polar Continental Shelf Program (PCSP), and Polar Knowledge Canada through Northern Scientific Training Program (NSTP).

I would like to thank the 2015/2016 Arctic field expedition crews, Shamus Duff, Etienne Godin, Taylor Haid, Elise Harrington, Jean Filion, Cassandra Marion, Robert Misener, Jennifer Newman, Alexandra Pontefract, Racel Sopoco, Michael Zanetti, and William Zylberman for their support making the field works successful. Also, many thanks to the space rocks lab and CPSX members for sharing their expertise and enthusiasm on planetary sciences.

I would like to extend my thanks to my former M. Sc. supervisor, Dr. Duk-jin Kim and SATGEO lab members at Seoul National University for helping me get started on this path and for encouraging me to be a better scientist every time I meet them at conferences.

I cannot forget to thank my parents and parents-in-law for believing and supporting me with love and patience. Special thanks to my mother-in-law for her dedicated support going back and forth between Canada and South Korea whenever I was away for fields and needed a hand, without whom I would not have completed this in time.

Last but not least, I truly thank my lovely wife, Ji Yeon Lim, without whom I would not be where I am today. Thank you for being my lifetime partner with endless love and support. I have truly enjoyed the journey with you, and expect much more for the rest of our journey with the amazing kids, Aine and Ian. I love you.

Table of Contents

List of Tables

List of Figures

List of Appendices

List of Acronyms

AST	Advanced Spaceborne Thermal Emission and Reflection Radiometer (ASTER)
ASU	Arizona State University
DEM	Digital Elevation Model
DN	Digital Number
ENVI	Environment for Visualizing Image software
ETM+	Landsat7 Enhanced Thematic Mapper plus
GEM	Geo-mapping for Energy and Minerals
HH	Horizontally-polarized transmitting and Horizontally-polarized receiving
HV	Horizontally-polarized transmitting and Vertically-polarized receiving
HIS	Hue-Intensity-Saturation
IEM	Integral Equation Method
InSAR	Interferometric SAR
L8	Landsat8
LUT	Look up table
MNF	Minimum Noise Fraction
MS	RADARSAT-2 Multiple Scattering
OLI	Landsat8 Operational Land Imager
PCA	Principal Component Analysis
PDH	Pedestal Height
PolSARpro	Polarimetric SAR Data Processing and Education Tool
RGB	Red-Green-Blue
RMS	Root Mean Square

ROI	Region of Interest
RPM	Remote Predictive Mapping
RS2	RADARSAT-2
SAM	Spectral Angle Mapper
SAR	Synthetic Aperture Radar
SDLP	Standard Deviation of Linear Polarizations
SFF	Spectral Feature Fitting
SWIR	Short Wavelength Infrared
TIR	Thermal Infrared
TOA	Top of Atmosphere
VH	Vertically-polarized transmitting and Horizontally-polarized receiving
VNIR	Visible Near Infrared
XRD	X-Ray Diffraction

Chapter 1

1 Introduction

The Canadian Arctic remains underexplored when compared to most other regions of Canada and other developed nations on Earth. Presently, it is only mapped at the reconnaissance level or regional scale (e.g., at a map scale of 1:250,000). Rapid climate change in the Arctic is resulting in a significant decrease in the extent of the cryosphere including sea ice, glaciers, and ice sheets, and formerly ice-covered land has been thawing and emerging (Overpeck et al., 1997). Geological mapping of the underlying strata will be critical to support land management at national, regional, and local levels, and support the decision-making processes of public and private sectors related to sustainable resource development and management. An increase of ice-free shipping channels and longer snow-free summers are the near-term prospect, and the huge potential for untapped resources in the Canadian Arctic highlights the need for more spatial and temporal mapping (Borgerson, 2008). However, limited access to the Arctic due to its remoteness, extreme weather, and short summers, and the expense of conducting field investigations all present substantial obstacles to a traditional boots-on-the-ground approach to mapping. In addition, it is hard to regularly update the map products. These concerns motivated the Remote Predictive Mapping (RPM) project in 2004 as a part of Geo-mapping for Energy and Minerals (GEM) program of Natural Resources Canada, which is based on orbital datasets to provide rapid access and broad spatial coverage of these remote northern and Arctic regions (see Harris et al., 2011, and references therein). Such work can facilitate and mitigate the time and expense spent on field investigations and supplement traditional geological field mapping over several field seasons.

Multi and hyperspectral orbital sensors (e.g., ASTER, Landsat, SPOT, and, Hyperion) are widely used for geological remote sensing as they can diagnose what minerals and lithologies are present based on spectral characteristics (Drury, 1993; van Der Meer et al., 2012). Extensive laboratory measurements have been collected of mineral and rock spectra (Christensen et al., 2000; Cooper et al., 2002; Hunt, 1977; Salisbury and D'Aria, 1992), and a variety of spectral parameters (e.g., band ratios, false colour composites, and principal component analysis (PCA) bands) have been proposed to characterize specific minerals and lithologies (Cloutis, 1996; Drury, 1993; Goetz and Rowan, 1981; Harris et al., 2014; Rowan et al., 1977; van Der Meer et al., 2012). Accordingly, mineral and lithological maps from various geological settings have been produced using multi and hyperspectral remote sensing data (Harris et al., 2011; Rowan et al., 2003; Rowan and Mars, 2003; Sabins, 1999; Tornabene et al., 2005).

This thesis hypothesizes that the extreme Arctic weathering, glacial erosion, and frost-shattering processes alter surfaces in different ways depending on rock types. The different physical surface properties can be readily characterized by SAR, which can play an important role in defining geological units with spectral mapping. Thus, the subsequent sections give an overview of SAR systems and SAR remote sensing and review SAR applications for geological mapping. An impact structure-based mapping approach is introduced with the geological settings of impact structures chosen for this work. The research objectives on how to pave the way for polarimetric SAR capabilities for remote predictive mapping are followed with an outline for each chapter.

1.1 SAR systems

Unlike passive optical sensors relying on the sun for their light source, synthetic aperture radar (SAR) is an active remote sensing system with its own microwave source, so it can acquire imagery day and night independent of sunlight. Also, the longer wavelengths in the microwave regime (e.g., X-band (2.5~4.0cm), C-band (4~8cm), S-band (8~15cm), L-band (15~30cm), P-band (30~100cm)) are not disturbed by cloud coverage and atmospheric noise, which is a great advantage for variable weather conditions like those found in the Arctic (Running et al., 1999).

The first spaceborne imaging radar for scientific studies was the earth-orbiting SEASAT SAR launched in 1978, which was operated at L-band (1.275 GHz, ~23.5cm in wavelength) with a single polarization of HH (i.e., transmitted and received through the horizontally polarized channel) (Born et al., 1979). This was followed by several single polarization airborne and spaceborne SAR sensors (e.g., SIR-A/B, ERS-1/2, JERS-1, and RADARSAT-1) (Lee and Pottier, 2009), in addition to several single polarization planetary SAR sensors (e.g., Pioneer-Venus, Venera 15, Magellan, Cassini) (Neish and Carter, 2014). The first polarimetric SAR imager for scientific studies was the L-band (1.225GHz, ~24.5cm in wavelength) AIRSAR launched in 1988 with a quad polarization system that transmits and receives radar signals through the horizontally polarized and vertically polarized channels (i.e., HH, HV, VH and VV) (Lee and Pottier, 2009). Since then, many dual or quad polarization airborne (e.g., Convair-580 C/X-SAR, E-SAR, PI-SAR, and UAVSAR) and spaceborne (e.g., SIR-C/X-SAR, ENVISAT ASAR, ALOS PALSAR-1/2, COSMO-SkyMed, TerraSAR/TanDEM-X, RADSATSAT-2, and Sentinel-1) SAR sensors have been launched. A polarimetric SAR sensor has even been sent to the Moon (e.g., Mini-RF) (Raney et al., 2011). In addition, a number of new SAR missions are scheduled to be launched in the near future (e.g., RADARSAT Constellation Mission (RCM), SAOCOM, TanDEM-L, Biomass, and NISAR), that would also utilize polarimetric imaging.

SAR is a side-looking system that transmits and receives radar signals in slant range with an incidence angle (or look angle) to avoid the ambiguity of the backscattering signals from targets at an equal range (vs. nadir-looking spectral sensors) (Brown and Porcello, 1969, Fig. 1.1). However, the slant range imaging results in geometrical distortions such as foreshortening, layover, and radar shadow depending on the incidence angle of a sensor and the slope of a target (Lee and Pottier, 2009).

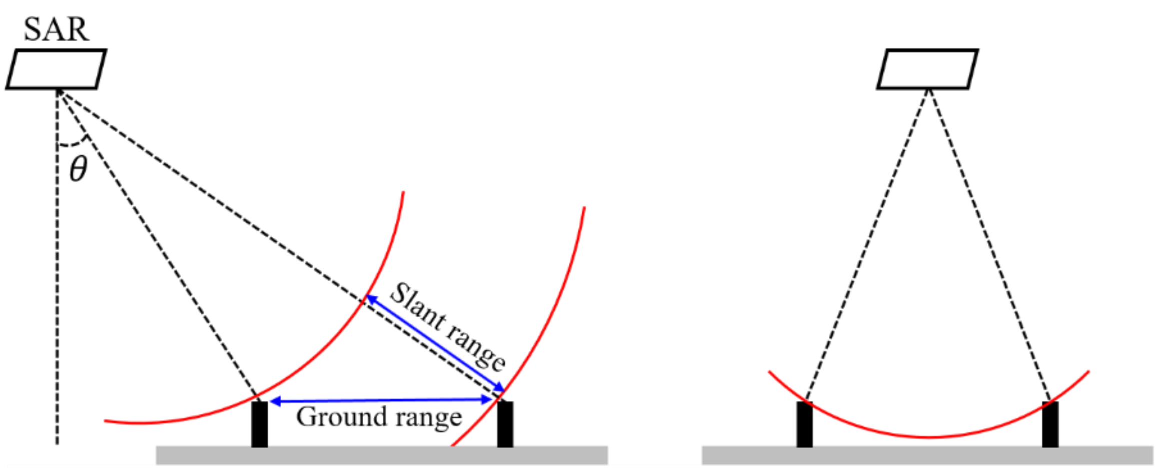

Figure 1.1. SAR side-looking imaging geometry (left; θ: incidence angle, ground range=slant range/$\boldsymbol{sin\theta}$) and nadir-looking geometry (right). Figure modified from Elachi et al. (1982).

The transmitted and received radar signals are recorded as a complex electric field vector ($\boldsymbol{E}$) and can be written in the form of the Jones vector as follows,

$$\boldsymbol{E} = \begin{bmatrix} \boldsymbol{E_x} \\ \boldsymbol{E_y} \end{bmatrix} = \begin{bmatrix} |\boldsymbol{E_x}|e^{i\boldsymbol{\delta}_x} \\ |\boldsymbol{E_y}|e^{i\boldsymbol{\delta}_y} \end{bmatrix} \tag{1.1}$$

where $|\boldsymbol{E_x}|$ and $|\boldsymbol{E_y}|$ are amplitude terms, and $\boldsymbol{\delta_x}$ and $\boldsymbol{\delta_y}$ are phase terms of the x and y components of an electric field vector at a fixed z, respectively (Jones, 1941). It can be written with the real part and the imaginary part by Euler's formula as follows (Fig. 1.2),

$$\boldsymbol{E} = \begin{bmatrix} |\boldsymbol{E_x}|(cos\boldsymbol{\delta_x} + isin\boldsymbol{\delta_x}) \\ |\boldsymbol{E_y}|(cos\boldsymbol{\delta_y} + isin\boldsymbol{\delta_y}) \end{bmatrix} \tag{1.2}$$

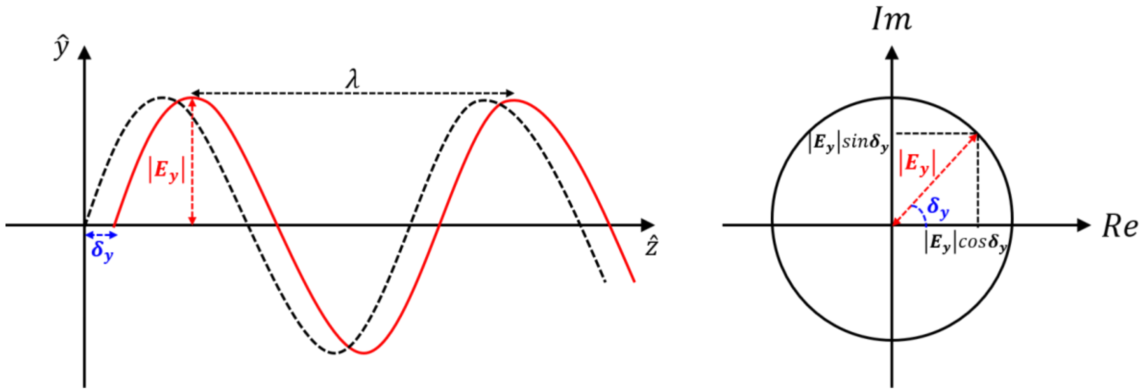

Figure 1.2. Sinusoidal wave of the $\boldsymbol{E_y}$ component of an electric field vector (left; λ: wavelength, $|\boldsymbol{E_y}|$: amplitude, and $\boldsymbol{\delta_y}$: phase) and its expression on the complex plane (right).

The radar backscattering coefficient (sigma naught, σ^0) is determined by the ratio of the power of the received vector $\boldsymbol{E_s}$ to the power of the transmitted vector $\boldsymbol{E_i}$ as follows,

$$\sigma^0 = \frac{4\pi r^2}{A_0}\frac{|\boldsymbol{E_s}|^2}{|\boldsymbol{E_i}|^2} \tag{1.3}$$

where r is the distance between the radar sensor and the target, and A_0 is the area of the radar cross section (i.e., illuminated area) (Lee and Pottier, 2009). The backscattering coefficients are associated with only the amplitude term, not the phase term. The backscattering coefficients show the intensity of the backscattering from a target surface (Fig. 1.3).

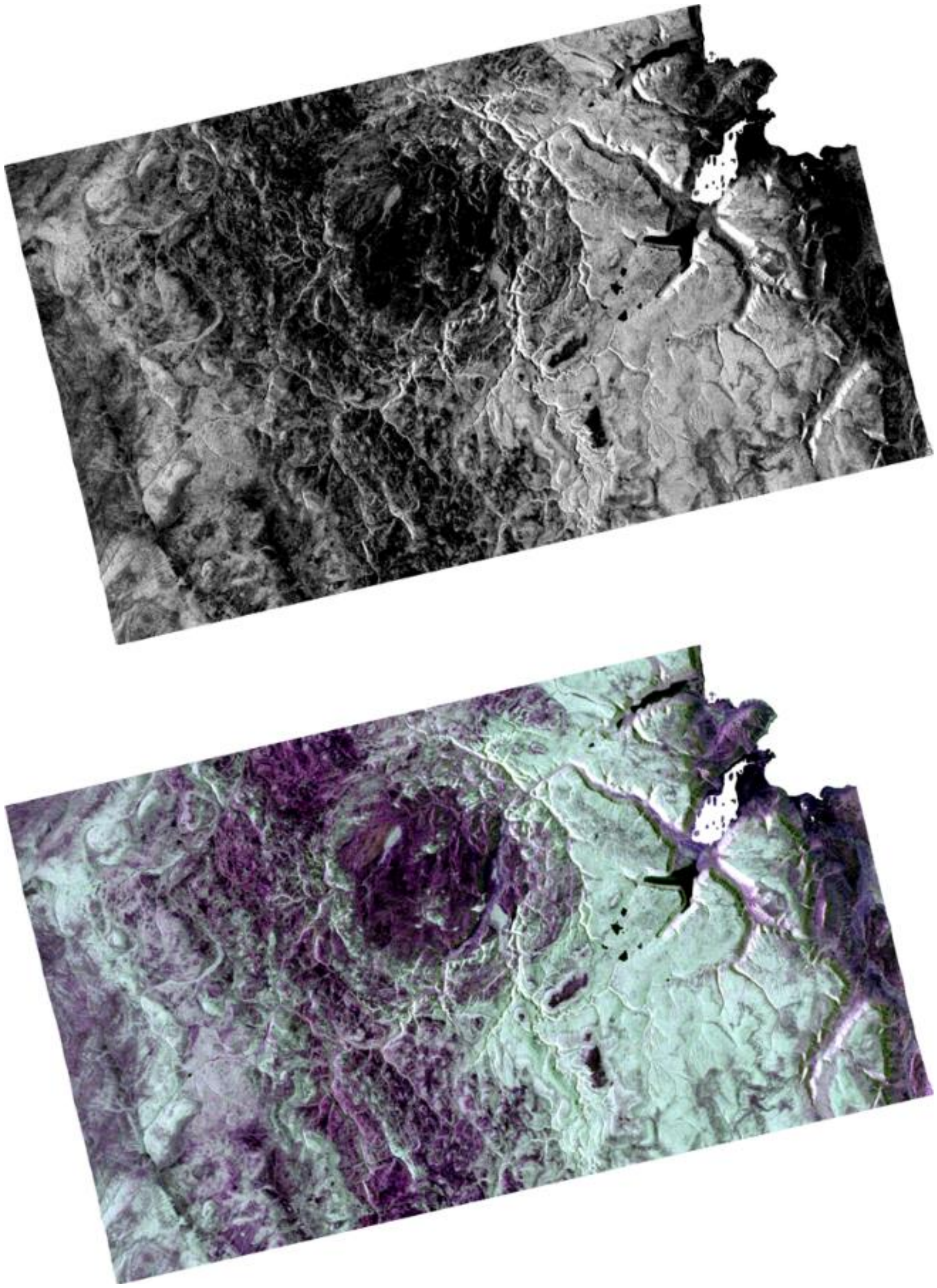

Figure 1.3. RADARSAT-2 (FQ19W mode) backscattering coefficient (σ^0) images of the Haughton impact structure (upper: HH single polarization, lower: RGB composite of HH (red), HV (green), and VV (blue) polarizations). Brighter areas have higher radar backscattering coefficients. Radar backscatter is a function of a surface's physical properties: its roughness, structure, and dielectric constant.

Polarimetric SAR generates the 2 by 2 complex scattering matrix ($\boldsymbol{S}$) from transmitted and received radar signals through horizontally and vertically polarized channels as follows,

$$\boldsymbol{E_s} = \frac{e^{-ikr}}{r}\,\boldsymbol{S}\,\boldsymbol{E_i} = \frac{e^{-ikr}}{r}\begin{bmatrix} S_{hh} & S_{hv} \\ S_{vh} & S_{vv} \end{bmatrix}\boldsymbol{E_i} \tag{1.4}$$

where S_{ij} are the complex scattering coefficients from the transmitted and received vectors of the quad polarimetric channels (i.e., HH, HV, VH, VV) and e^{-ikr}/r is the radar attenuation effect term according to the distance between the radar and the target (r) and the radar wavenumber ($k=2\pi/\lambda$) (Lee and Pottier, 2009).

1.2 SAR remote sensing

SAR remote sensing utilizes the amplitude and phase information derived from radar backscattering signals. The phase difference (or phase shift) between two or more SAR acquisitions is exploited for a variety of interferometric SAR (InSAR) applications relating to topographic height (e.g., digital elevation model (DEM) generation) or movement of a target (e.g., ground moving target velocity measurement and surface displacement monitoring) (Hanssen, 2001). The intensity (or power) of the radar backscattering coefficient, which is the square of the amplitude, is largely affected by the physical nature of a target such as its surface roughness, structure, and dielectric properties (Ulaby et al., 1982). As a result, these data are widely applied for characterizing distinct target features (e.g., ship detection (Touzi et al., 2015), oil spill detection (Kim et al., 2010), sea ice and iceberg detection (Denbina and Collins, 2012; Kim et al., 2012; Scheuchl et al., 2004), oyster habitat mapping (Choe et al., 2012), and crop monitoring (Huang et al., 2017; McNairn et al., 2002)) and for estimating the surface roughness and/or dielectric properties of a target region (e.g., Fung et al., 1992; Hajnsek et al., 2003; Oh, 2004). However, the physical properties inferred from SAR are often neglected in characterizing and classifying geological units compared to their mineral and lithological properties, and few studies have taken these SAR capabilities into consideration in geological remote mapping. Geological surfaces in the Arctic are altered by weathering, erosion, and deposition processes through extensive glacial activity and recurrent freeze-thaw cycles (Dredge, 1992; Hudec, 1973). Different rocks are weathered in different ways depending on their resistance to weathering, and form different surface expressions accordingly (Hudec, 1998; McCarroll and Nesje, 1996). Since Arctic surfaces have the advantage of minimal vegetation (dense vegetation such as shrubs and bushes can affect the radar backscattering from a target surface for relatively short wavelength X- and C-band radars), weathering, frost shattering, and depositional features can be readily imaged by polarimetric SAR. In this work, we argue that this information should be incorporated into remote predictive mapping algorithms.

1.3 SAR applications for geological mapping

The SEASAT SAR mission launched in 1978 was dedicated to oceanographic observations and only operated for about 3 months, but also provided interesting results for geological application (Born et al., 1979; Elachi et al., 1982). SEASAT SAR images captured the textural variation between the Tertiary limestones of karst topography (fine texture) and the pre-Eocene igneous and metamorphic rocks (coarse texture) in the region of the Blue Mountains in eastern Jamaica and the northeast part of the Dominican Republic (Elachi et al., 1982). Blom and Daily (1982) combined SEASAT and Landsat for lithological mapping of San Rafael Swell, Utah, US, and showed that the textual variation in the SAR image can greatly contribute to rock type discrimination. Schaber et al. (1980) reported that different radar brightness in the SP Mountain volcanic field, Arizona, US, depends on the surface roughness of lava flows. Also, lineament feature mapping for sand dunes (Blom and Elachi, 1981), glacial landforms (e.g., drumlines, moraines) (Ford, 1984), and mountainous areas (Ford, 1980), and structural mapping for mining districts (Pour and Hashim, 2014; Singhroy and Molch, 2004) were conducted using radar backscattering characteristics sensitive to the slope and orientation of a target relative to the radar illumination.

With the recent launches of polarimetric SAR systems, a number of cutting edge polarimetric SAR analysis techniques and polarimetric SAR-derived parameters relating to the physical nature of targets have been developed. Over the years, however, there have been only several studies aimed at applying polarimetric SAR capabilities to the geological mapping of northern and Arctic Canada (summarized in Table 1.1). Early studies with single polarization data mainly focused on extracting lineament features and observing the variation in radar backscattering properties from different geological units. Graham and Grant (1991) identified faults, fractures, and glacial lineament features in the Red Indian Lake area, central Newfoundland, and confirmed that radar backscattering brightness and texture depends on surface roughness and is capable of revealing moraines, boulders, and stony tills. Budkewitsch and D'Iorio (1997) observed the difference of radar backscattering brightness between rough limestone and smooth siltstone folds in Bathurst Island, Nunavut. Smith et al. (1999) extracted radial and circumferential fracturing features of five complex impact structures (i.e., Mistastin, Charlevoix, Clearwater, Manicouagan, and Haughton) in northern and Arctic Canada. They suggested that the different appearance in radar backscattering observed in the five impact structures is related to the degree of erosion and their different lithologies. In particular, impact melt rocks and the evaporite-rich Bay Fiord formation of the Arctic Platform showed distinctively low radar backscattering characteristics. Grunsky (2002) showed that the components derived from a Principal Component Analysis (PCA) of multiple RADARSAT-1 images acquired at different incidence angles can be related to surface roughness, moisture, topography, and the types of surficial materials in northeastern Alberta. Mei and Paulen (2009) also showed that arithmetical combinations of multiple RADARSAT-1 images at different incidence angles can highlight glacial landforms, meltwater channels, sand dune ridges, and fluvial deposits in the Mt. Watt and Meander River area, northwest Alberta. Grunsky et al., (2006) attempted to combine RADARSAT-1 with Landsat 7 ETM+ and DEM data based on a maximum likelihood supervised classifier and mapped surficial materials (i.e., bedrock, boulders, sand and gravel, glacial tills, and organic deposits) in the Schulz Lake area, Nunavut. Similarly, Pavlic et al. (2008) produced a surficial material map of the upper Mackenzie Valley, N.W.T., by Hue-Intensity-Saturation (HIS) based image fusion of RADARSAT-1, Landsat 7 ETM+, and DEM, and it was well correlated with glacial tills, glaciofluvial, colluvial, and organic deposits. Wall et al. (2010) monitored the change of surface soil moisture in the Cape Bounty Arctic Watershed Observatory, Melville Island, Nunavut, by applying a regression analysis of RADARSAT-1 radar backscattering coefficients and ratios to volumetric soil moisture measurements.

Only a few studies have taken advantage of polarimetric SAR for geological mapping in northern and Arctic Canada. Saint-Jean et al. (1999) showed that the VH polarization could more readily detect the distribution and orientation of lineament features of the Matamec Igneous Complex in eastern Quebec. LaRocque et al. (2012) produced a surficial material map of the Schulz Lake area, Nunavut, by combining HH and HV dual polarimetric RADARSAT-2, Landsat 7 ETM+, and Canadian Digital Elevation Model (CDEM) data into a maximum likelihood classifier. Shelat et al. (2012a) also applied the same classification method but with quad polarimetric RADARSAT-2, Landsat 7 ETM+, and CDEM, and produced a surficial material map of the Umiujalik Lake area, Nunavut. Both studies are in line with (Grunsky et al., 2006) and have only focused on improving classification accuracy by adding polarimetric SAR channels as additional inputs. Shelat et al. (2012b) further investigated different polarization signatures of surficial material units in the Umiujalik Lake area, Nunavut with quad polarimetric RADARSAT-2 data and produced polarimetric classification maps by applying Wishart, Freeman-Durden, and Cloude-Pottier (i.e., entropy (H), anisotropy (A), and alpha angle (α)) classifiers, but polarimetric SAR on its own resulted in much lower classification accuracies than that of the combined classification with multispectral sensors when compared to a geological map.

Likewise, quad polarimetric SAR capabilities have not been fully exploited for geological remote sensing in the Canadian Arctic. In particular, physical surface properties (e.g., centimeter-scale surface roughness, volumetric soil moisture) of geological units in the Canadian Arctic need to be further studied based on polarimetric SAR analysis techniques (e.g., polarimetric SAR decomposition, polarimetric SAR scattering model inversion, polarization signature parameters). This is especially important in the Arctic, where extreme weathering processes alter the physical properties of the rocks quite markedly.

Table 1.1. SAR application studies for geological mapping in northern and Arctic Canada

Study area	Reference	Data (Polarization)	Description
Red Indian Lake area, central Newfoundland	*Graham and Grant, 1991*	Convair-580 airborne SAR (HH)	- Identification of faults, fractures, glacial lineament features - Radar brightness and texture variation in moraines, boulders, and stony tills
Bathurst Island, Nunavut	*Budkewitsch and D'Iorio, 1997*	RADARSAT-1 (HH)	- Difference in radar backscattering brightness observed from rough limestone and smooth siltstone folds
Five complex impact structures in northern Canada (Mistastin, Charlevoix, Clearwater, Manicouagan, Haughton)	*Smith et al. 1999*	RADARSAT-1 (HH)	- Lineament feature extraction of impact structure patterns - Different appearance in radar backscattering depending on the degree of erosion and different lithologies - Very dark radar brightness from impact melt rocks and evaporite rocks
northeastern Alberta	*Grunsky, 2002*	RADARSAT-1 (HH)	- Principal component analysis of multi-beam RADARSAT-1 images - Related to surface roughness, moisture, topography, and surficial materials.

Mt. Watt and Meander River area, northwest Alberta	*Mei and Paulen, 2009*	RADARSAT-1 (HH) with DEM	- Arithmetic combination of multi-beam RADARSAT-1 images on a shaded relief DEM - Glacial landforms, meltwater channels, sand dune ridges, and fluvial deposits
Schultz Lake area, Nunavut	*Grunsky et al. 2006*	RADARSAT-1 (HH) with Landsat7 ETM+ and DEM	- Maximum likelihood supervised classification of surficial materials - Bedrock, boulders, sand and gravel, glacial tills, and organic deposits
Mackenzie Valley Pipeline Corridor, North West Territories	*Pavlic et al. 2008*	RADARSAT-1 (HH) with Landsat7 ETM+ and DEM	- Surficial materials mapping by SAR-DEM-ETM+ image fusion (glacial till, glaciofluvial, colluvial and organic deposits)
Melville Island, Nunavut	*Wall et al. 2010*	RADARSAT-1 (HH)	- Soil moisture change monitoring by the regression analysis between radar backscattering and soil moisture values
Matamec Igneous Complex, Lac Volant area, eastern Quebec	*Saint-Jean et al. 1999*	Convair-580 airborne SAR (quad)	- Enhancement in VH polarization in extracting the distribution and orientation of lineament features
Schultz Lake area, Nunavut	*LaRocque et al. 2012*	RADARSAT-2 (HH, HV) with Landsat7 ETM+ and DEM	- Maximum likelihood supervised classification of surficial materials

			- Bedrock, boulders, sand and gravel, glacial tills, and organic deposits
Umiujalik Lake area, Nunavut	*Shelat et al. 2012a, 2012b*	RADARSAT-2 (quad) with Landsat7 ETM+ and DEM	- Maximum likelihood supervised classification of surficial materials - Bedrock, boulders, sand and gravel, glacial tills, and organic deposits - Effect of incidence angles and polarization on classification accuracy - Supervised and unsupervised classification using Wishart, Freeman-Durden, and Cloude-Pottier polarimetric classifiers - Polarization signature analysis

1.4 Why study impact structures?

It is very challenging to find well-exposed outcrops for geological mapping in the Canadian Arctic. Meteorite impact structures can be a strategic point for mapping regional geology within a limited area. Meteorite impact structures are highly localized complex geological features that include a variety of impact-generated products (e.g., shatter cones, central uplifts, listric faults, impactites, hydrothermal alterations) (Osinski and Pierazzo, 2012). They are formed by hypervelocity impact events, which produce structural lineaments, such as fractures and faults. These features are particularly conducive to SAR investigation (e.g., McHone et al., 2002; Smith et al., 1999). In addition, subsurface lithologies from a depth directly proportional to the size of a crater are excavated and exposed through crater walls, terraces, ejecta, and central uplift features (Osinski and Pierazzo, 2012; Stewart and Valiant, 2006). Impact-exposed outcrops of subsurface lithologies can be used to reconstruct a significant portion of the regional stratigraphic column (e.g., Michalski and Niles, 2010; Quantin et al., 2012; Tornabene et al., 2005). Thus, impact structure-based mapping can be effectively extended to mapping over a broader regional lithologies. In addition, impact structures themselves are also important targets for resource exploration, as approximately 25% of impact structures on Earth possess economic resources (Grieve, 2012). For example, uranium ore deposits in the Carswell impact structure located in the Athabasca Basin, Saskatchewan, Canada, originated from the structural uplift of the Athabasca Group basement core by the impact (Grieve, 2012). The world-class nickel-copper-platinum group elements (Ni-Cu-PGE) ore deposits in the Sudbury impact structure, Ontario, Canada, are associated with impact-generated magmatic and hydrothermal processes (Ames and Farrow, 2007).

1.5 Geological setting of study areas

The Tunnunik and Haughton impact structures in the Canadian Arctic were the focus for this work. The Tunnunik impact structure (formerly known as the Prince Albert structure) is a deeply eroded complex impact structure (centred at 72° 28’N, 113° 58’W) on Victoria Island, Northwest Territories, Canada (Dewing et al., 2013, Fig. 1.4). The regional geology of this part of Victoria Island comprises the Arctic Platform and the Canadian Shield, with the latter exposed as part of the Minto Arch. The regional stratigraphy and target sequence exposed in the Tunnunik structure includes, from oldest to youngest: 1) the Neoproterozoic Shaler Supergroup (mainly comprised of grainstone, sandstone, and shale); 2) the Cambrian Quyuk Formation (or Clastic Unit; sandstone and mudstone); 3) the Cambrian Uvayualuk Formation (or Tan Dolostone Unit; dolomudstone and dolosandstone); 4) the Cambrian Mount Phayre Formation (or Stripy Unit; mudstone, shale, and interbedded dolomudstone); 5) the Cambrian-Ordovician Victoria Island Formation (dolostone, chert, and crystalline quartz); and 6) the Ordovician-Silurian Thumb Mountain/Allen Bay Formation (dolostone and dolomudstone) (Dewing et al., 2013, Fig. 1.5). A preliminary bedrock map of northern Victoria Island has been produced on a scale of 1:500,000 by the Geological Survey of Canada (Dewing et al., 2015), but a more detailed geological map is not available yet. The Tunnunik structure was confirmed to be of impact origin in 2010 based on the discovery of shatter cones and uplifted and inclined strata around the centre of the structure, which is the eroded remains of the central uplift (Dewing et al., 2013). The impact is assumed to have occurred <360 Myr ago (Ma) when pre-impact hydrothermal dolomitization occurred in the Ordovician limestones, but the exact age is currently unknown. Fieldwork carried out in 2012 resulted in a refined estimate of the apparent diameter of 28 km based on the mapping of inward-dipping listric faults out to a radius of ~14 km along the crater rim (Osinski et al., 2013, Fig. 1.5). Regional linear faults trending NW-SE and NE-SW crosscut the structure. Shatter cones, dipping strata of the eroded central uplift (Dewing et al., 2013), impact-generated hydrothermal alteration (Marion et al., 2013), and impact breccia dykes (Osinski et al., 2013) were confirmed within the structure. However, there is no preserved evidence of crater fill and ejecta materials. Most of surfaces are deeply weathered and altered by glacial activities and freeze-thaw processes, or locally covered by thick Quaternary glacial and periglacial sediments (Newman and Osinski, 2016).

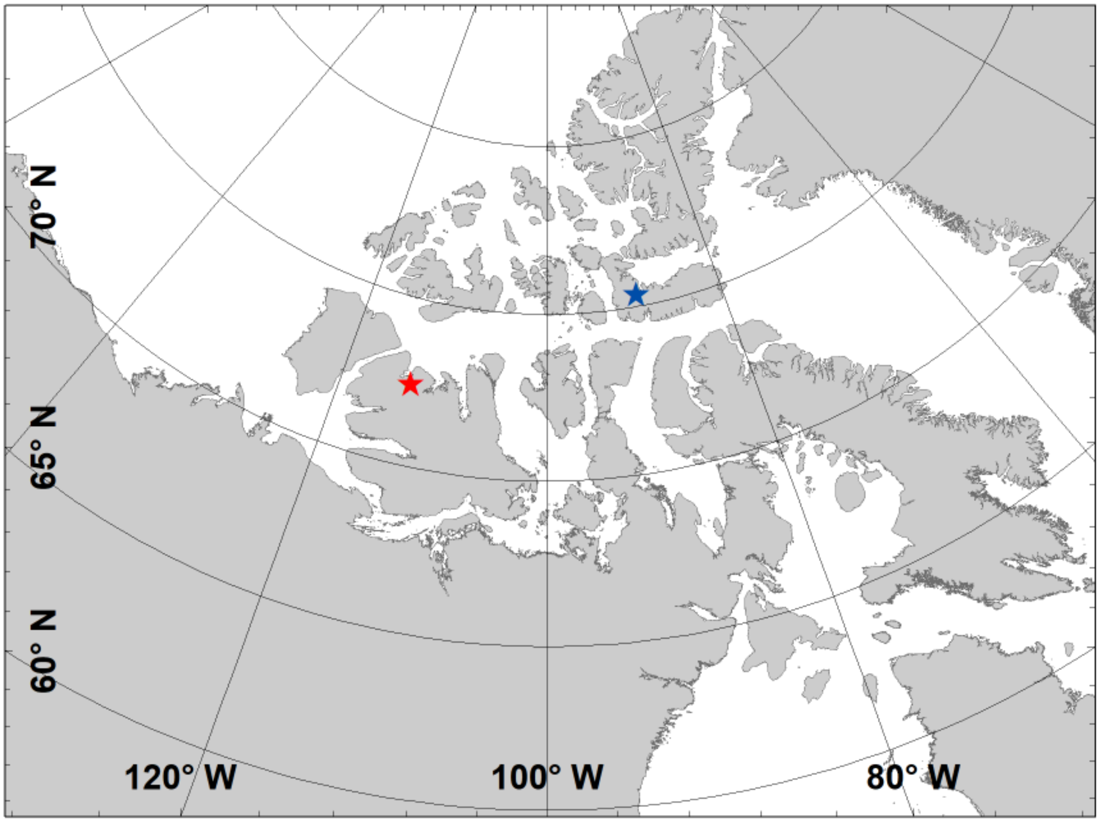

Figure 1.4. Locations of the Tunnunik (red star) and the Haughton (blue star) impact structures.

The Haughton impact structure is a relatively young and well-preserved complex impact structure with an apparent diameter of 23 km (centred at 75°22’N, 89°41’W) on Devon Island, Nunavut, Canada (Osinski and Spray, 2005, Fig. 1.4). The impact was estimated at ~39 Ma by ^{40}Ar-^{39}Ar laser probe dating of highly shocked crystalline basement clasts (Sherlock et al., 2005). The Haughton structure was formed in a ~1.9 km thick flat-lying Lower Paleozoic (i.e., Ordovician to Silurian) sedimentary sequence of the Arctic platform overlying the Canadian Shield. The crater rim and wall are mainly on the Middle Member of the Allen Bay Formation of thin-bedded dolomite and the Lower Member of the Allen

Bay Formation of thick-bedded and massive limestone and dolomite (Osinski et al., 2005, Fig. 1.6). The older Thumb Mountain Formation of medium- to thick-bedded limestone and dolomite and the Bay Fiord Formation of medium- to thick-bedded dolomite, crystalline gypsum and anhydrite, and coral fossils, are observed along the eastern crater wall, and the Eleanor River Formation of medium- to thick-bedded limestone and thin-bedded dolomite is exposed around the central uplift (Osinski et al., 2005, Fig. 1.6). Extensive crater-fill deposits (i.e., impact melt rocks) are well preserved within the structure, and are overlain by the Haughton Formation of post-impact lacustrine sediments and the Quaternary fluvioglacial and fluvial sediments along the Haughton River valley (Osinski et al., 2005, Fig. 1.6). Shatter cones are well developed within the central uplift (Osinski and Spray, 2006), and impact-generated hydrothermal alterations are present in the form of vugs and veins within impact melt rocks and the central uplift, and hydrothermal pipe structures along the faulted crater rim (Osinski et al., 2005b). Extensive field surveys and mapping have been conducted for the Haughton impact structure and produced a detailed geological map (Osinski et al., 2005a).

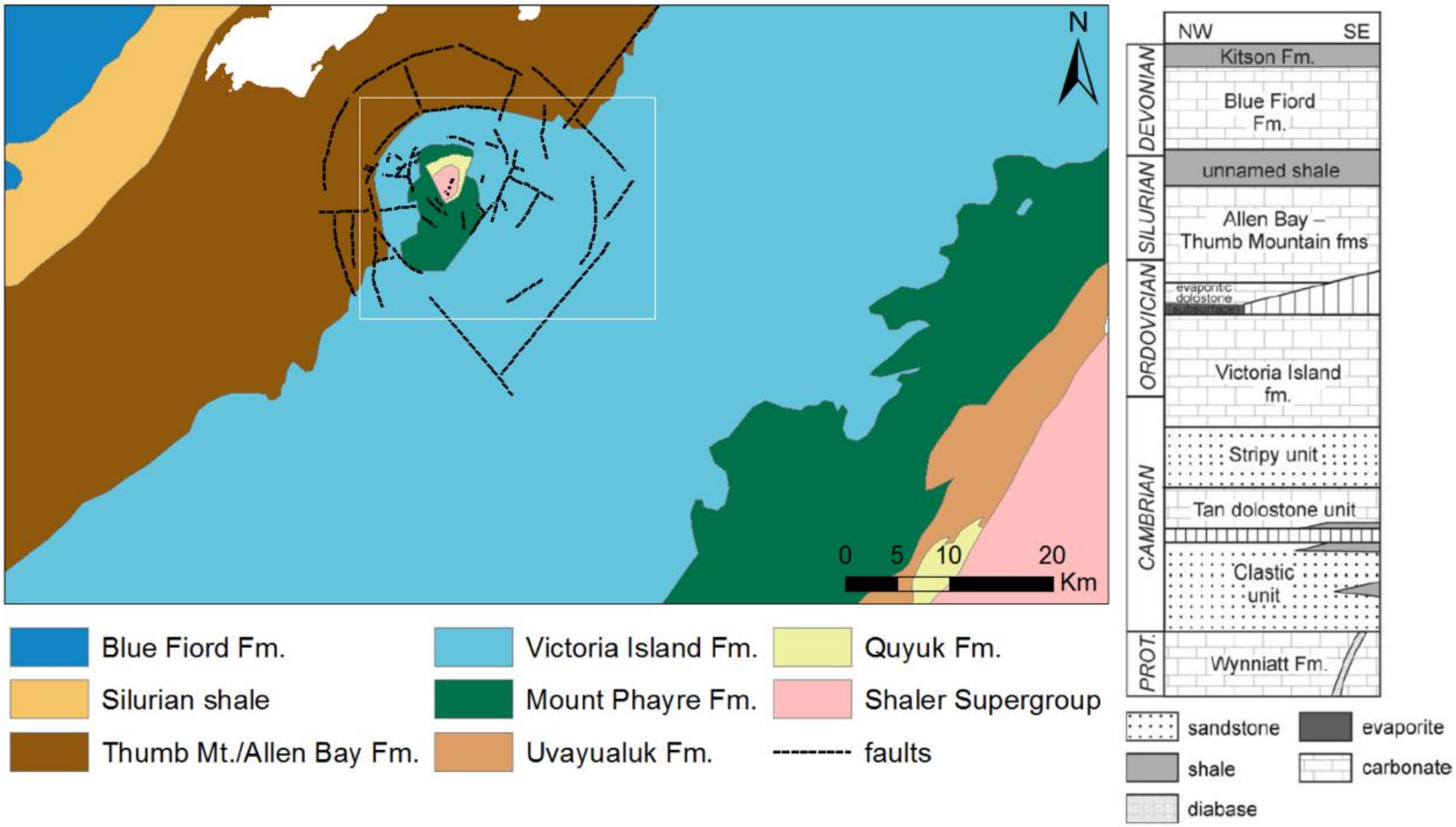

Figure 1.5. Simplified geological map of the Tunnunik impact structure and northwestern Victoria Island (left, modified from Dewing et al. (2015)) and stratigraphic column of northwestern Victoria Island (right, from Dewing et al. (2013)). The white square represents the coverage of the remote sensing datasets used in Chapter 2.

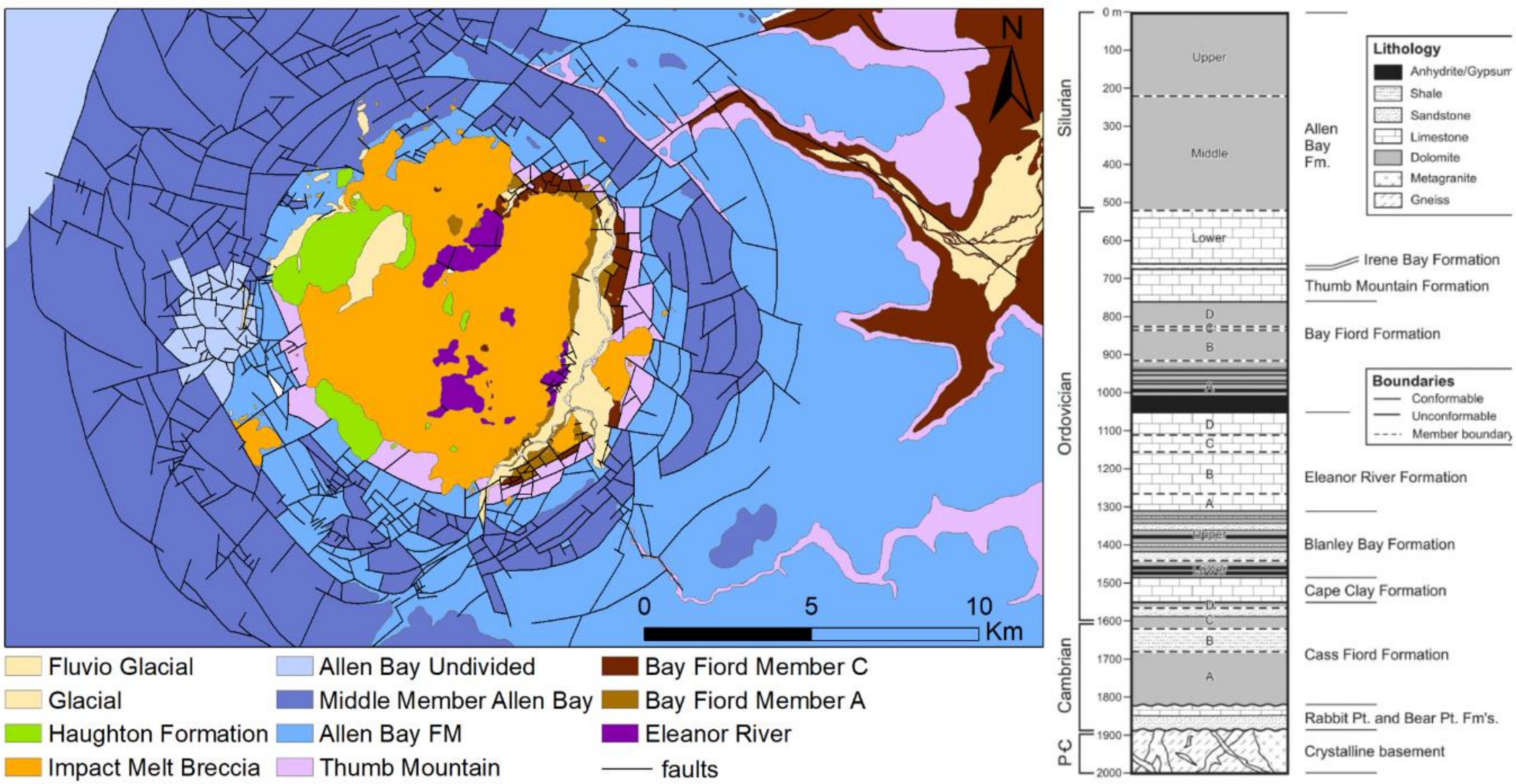

Figure 1.6. Simplified geological map of the Haughton impact structure (left, modified from Osinski et al. (2015)) and stratigraphic column of the target sequence at the Haughton impact structure (right, from Osinski et al. (2005)).

1.6 Thesis objectives and outline

This study aims to investigate how polarimetric SAR can refine the remote predictive mapping techniques and enhance our geological knowledge of the region, particularly in terms of physical surface properties, with the following research questions:

1) Can the physical surface properties of different geological units in the Canadian Arctic be determined using radar scattering mechanisms (i.e., single-bounce surface scattering, double-bounce dihedral scattering, and multiple-diffused scattering) investigated by polarimetric SAR decomposition techniques?

2) How can quantitative surface parameters, such as surface roughness and soil moisture, be estimated using a radar scattering model inversion method? And how can the semi-empirical radar scattering model developed based on bare soil surfaces be modified for weathered rock surfaces much rougher than soil sediments?

3) How do the radar backscattering responses from different geological units vary depending on polarizations? And can the polarization signatures be parameterized to characterize the surface roughness of geological units?

4) Finally, can the polarimetric SAR-derived physical surface properties be associated with mineralogical and lithological properties characterized from multispectral sensors? How can they be combined for remote predictive geological mapping of the Canadian Arctic?

The thesis is structured as follows:

In Chapter 2, the 28-km diameter Tunnunik impact structure is mapped using ASTER, Landsat 8, RADARSAT-2 polarimetric SAR, and Quickbird data. Multispectral analysis is accomplished through band ratios, minimum noise fraction (MNF) transform, and spectral matching algorithms, from which distinct spectral units are defined. Polarimetric SAR decompositions are also applied to characterize radar scattering mechanisms for the distinct spectral units and associate them with physical surface properties. The multispectral and polarimetric SAR mapping is combined with detailed surface textures and morphological features as observed in the high-resolution Quickbird imagery. All the remote sensing observations are integrated to interpret the geology of this region. Based on the preliminary interpretations, remote sensing parameters and their thresholds for each unit are implemented into a decision-tree algorithm and a remote predictive geological map is produced. Subsequent field and follow-up laboratory investigations are compared to the remote predictive map.

In Chapter 3, surface roughness and volumetric soil moisture of the Tunnunik and Haughton structures are estimated from RADARSAT-2 quad-polarimetric SAR through radar scattering model inversion. The limitations of radar scattering models developed based on bare soil surfaces for Arctic surfaces are discussed. A newly modified semi-empirical radar scattering model for weathered rock surfaces is presented. Based on the numerical formula of the cross-polarization ratio proposed by Oh (2004), which is modeled by only surface roughness parameters with no dependence on soil moisture, the best fitting model for weathered rock surfaces is determined with surface profiles collected from weathered rock surfaces in the Tunnunik and Haughton impact structures and corresponding RADARSAT-2 quad-polarimetric SAR data. The estimated results are compared to the in situ surface measurements.

In Chapter 4, polarimetric SAR signatures of geological units in the Tunnunik and Haughton impact structures are characterized using RADARSAT-2 quad polarimetric SAR. Three-dimensional polarimetric SAR signature plots are generated with radar backscattering responses according to the orientation and ellipticity angles of the polarization ellipse. The pedestal height and the standard deviation of linear co-polarization responses are calculated from the 3-dimensional polarization signature, and then compared to in situ surface roughness measurements. The correlation between the polarimetric SAR signatures of the geological units and their surface roughness are analyzed.

In Chapter 5, major findings are summarized, and general discussion and conclusions are presented with suggestions for future work.

1.7 References

Ames, D.E., Farrow, C.E.G., 2007. Metallogeny of the Sudbury mining camp, Ontario. Mineral deposits of Canada: A synthesis of major deposit-types, district metallogeny, the evolution of geological provinces, and exploration methods. Geol. Assoc. Canada, Miner. Depos. Div. Spec. Publ. 5, 329–350.

Blom, R., Daily, M., 1982. Radar image processing for rock-type discrimination. IEEE Trans. Geosci. Remote Sens. GE-20, 343–351. doi:10.1109/TGRS.1982.350453

Blom, R., Elachi, C., 1981. Spaceborne and airborne imaging radar observations of sand dunes. J. Geophys. Res. 86, 3061–3073. doi:10.1029/JB086iB04p03061

Borgerson, S.G., 2008. Implications of global warming. Foreign Aff. 87, 63–77.

Born, G.H., Sunne, J.A., Lame, D.B., 1979. Seasat mission overview. Science (80-.). 204, 1405–1406.

Brown, W.M., Porcello, L.J., 1969. An introduction to synthetic-aperture radar. IEEE Spectr. 6, 52–62. doi:10.1109/MSPEC.1969.5213674

Budkewitsch, P., D'Iorio, M.A., 1997. Contribution toward understanding C-band SAR data for lithological discrimination and structural mapping in the Canadian Arctic, in: Proceedings of 12th International Conference and Workshop on Applied Geologic Remote Sensing. Denver, Colorado, pp. 38–41.

Choe, B.-H., Kim, D., Hwang, J.-H., Oh, Y., Moon, W.M., 2012. Detection of oyster habitat in tidal flats using multi-frequency polarimetric SARdata. Estuar. Coast. Shelf Sci. 97, 28–37. doi:10.1016/j.ecss.2011.11.007

Christensen, P.R., Bandfield, J.L., Hamilton, V.E., Howard, D.A., Lane, M.D., Piatek, J.L., Ruff, S.W., Stefanov, W.L., 2000. A thermal emission spectral library of rock-forming minerals. J. Geophys. Res. 105, 9735–9739.

Cloutis, E.A., 1996. Review article hyperspectral geological remote sensing: evaluation of analytical techniques. Int. J. Remote Sens. 17, 2215–2242. doi:10.1080/01431169608948770

Cooper, B.L., Salisbury, J.W., Killen, R.M., Potter, A.E., 2002. Midinfrared spectral features of rocks and their powders. J. Geophys. Res. Planets 107, 1–17. doi:10.1029/2000JE001462

Denbina, M., Collins, M.J., 2012. Iceberg detection using compact polarimetric synthetic aperture radar. Atmosphere-Ocean 50, 437–446. doi:10.1080/07055900.2012.733307

Dewing, K., Hadlari, T., Rainbird, R.H., Bédard, J.H., 2015. Phanerozoic geology, northwestern Victoria Island, Northwest Territories; Geological Survey of Canada, Canadian Geoscience Map 171 (preliminary), scale 1:500 000. doi:10.4095/295530

Dewing, K., Pratt, B.R., Hadlari, T., Brent, T., Bédard, J., Rainbird, R.H., 2013. Newly identified “Tunnunik” impact structure, Prince Albert Peninsula, northwestern Victoria Island, Arctic Canada. Meteorit. Planet. Sci. 48, 211–223. doi:10.1111/maps.12052

Dredge, L.A., 1992. Breakup of limestone bedrock by frost shattering and chemical weathering , eastern Canadian Arctic. Arct. Alp. Res. 24, 314–323.

Drury, S.A., 1993. Image interpretation in geology, 2nd ed. Chapman and Hall, London.

Elachi, C., Bicknell, T., Jordan, R.L., Wu, C., 1982. Spaceborne synthetic-aperture imaging radars: Applicatoins, techniques, and technology. Proc. IEEE 70, 1174–1209.

Ford, J.P., 1984. Mapping of glacial landforms from seasat radar images. Quat. Res. 321, 314–321.

Ford, J.P., 1980. Seasat orbital radar imagery for geologic mapping: Tennessee-Kentucky-Virginia. Am. Assoc. Pet. Geol. Bull. 64, 2064–2094.

Fung, A.K., Li, Z., Chen, K.S., 1992. Backscattering from a randomly rough dielectric surface. IEEE Trans. Geosci. Remote Sens. 30, 356–369. doi:10.1109/36.134085

Goetz, A.F., Rowan, L.C., 1981. Geologic remote sensing. Science (80-.). 211, 781–791. doi:10.1126/science.211.4484.781

Graham, D.F., Grant, D.R., 1991. A test of airborne, side-looking synthetic-aperture radar in central Newfoundland for geological reconnaissance. Can. J. Earth Sci. 28, 257–265.

Grieve, R.A.F., 2012. Economic deposits at terrestrial impact structures, in: Osinski, G.R., Pierazzo, E. (Eds.), Impact Cratering: Processes and Products. Wiley-Blackwell, pp. 177–193.

Grunsky, E.C., 2002. The application of principal components analysis to multi-beam RADARSAT-1 satellite imagery: A tool for land cover and terrain mapping. Can. J. Remote Sens. 28, 758–769. doi:10.5589/m02-071

Grunsky, E.C., Harris, J.R., McMartin, I., 2006. Predictive mapping of surficial materials, Schultz lake area (NTS 66A), Nunavut, Canada. Geological Survery of Canada, Open File 5153.

Hajnsek, I., Cloude, S.R., Lek, J., Eric, P., 2003. inversion of surface parameters from polarimetric sar data 41, 1095–1097.

Hanssen, R.F., 2001. Radar Interferometry: Data interpreatation and error analysis.

Springer Netherlands, Dordrecht. doi:10.1007/0-306-47633-9

Harris, J.R., He, J.X., Rainbird, R., Behnia, P., 2014. A comparison of different remotely sensed data for classifying bedrock types in Canada's Arctic: Application of the Robust Classification Method and Random Forests. Geosci. Canada 41, 557. doi:10.12789/geocanj.2014.41.062

Harris, J.R., Wickert, L., Lynds, T., Behnia, P., Rainbird, R., Grunsky, E., McGredor, R., Schetselaar, E., 2011. Remote Predictive Mapping 3. Optical Remote Sensing –A Review for Remote Predictive Geological Mapping in Northern Canada 38, 49–83.

Huang, X., Wang, J., Shang, J., Liao, C., Liu, J., 2017. Application of polarization signature to land cover scattering mechanism analysis and classification using multi-temporal C-band polarimetric RADARSAT-2 imagery. Remote Sens. Environ. 193, 11–28. doi:10.1016/j.rse.2017.02.014

Hudec, P.P., 1998. Rock properties and physical processes of rapid weathering and deterioration, in: Proceedings of 8th International Congress of IAEG. pp. 335–341.

Hudec, P.P., 1973. Weathering of rocks in Arctic and sub-arctic environment, in: Proceedings of the Symposium on the Geology of the Canadian Arctic. pp. 313–335.

Hunt, G.R., 1977. Spectral signatures of particulate minerals in the visible and near infrared. Geophysics 42, 501–513.

Jones, R.C., 1941. I . Description and discussion of the calculus. J. Opt. Soc. Am. 31, 488–493. doi:http://dx.doi.org/10.1364/JOSA.31.000488

Kim, D., Moon, W.M., Kim, Y.S., 2010. Application of TerraSAR-X data for emergent oil-spill monitoring. IEEE Trans. Geosci. Remote Sens. 48, 852–863. doi:10.1109/TGRS.2009.2036253

Kim, J.-W., Kim, D., Hwang, B.-J., 2012. Characterization of Arctic sea ice thickness using high-resolution spaceborne polarimetric SAR data. IEEE Trans. Geosci. Remote Sens. 50, 13–22.

LaRocque, A., Leblon, B., Harris, J., Jefferson, C., Tschirhart, V., Shelat, Y., 2012. Surficial materials mapping in Nunavut, Canada with multibeam RADARSAT-2 dual-polarization C-HH and C-HV, LANDSAT-7 ETM+, and DEM data. Can. J. Remote Sens. 38, 281–305. doi:10.5589/m12-020

Lee, J.-S., Pottier, E., 2009. Polarimetric radar imaging: from basics to applications. CRC Press, New York.

Marion, C.L., Osinski, G.R., Linnen, R.L., 2013. Characterization of Hydrothermal Mineralization at the Prince Albert Impact Structure, Victoria Island, Canada, in: 44th Lunar and Planetary Science Conference. p. Abstract #1635.

McCarroll, D., Nesje, A., 1996. Rock surface roughness as an indicator of degree of rock surface weathering. Earth Surf. Process. Landforms 21, 963–977. doi:10.1002/(SICI)1096-9837(199610)21:10<963::AID-ESP643>3.0.CO;2-J

McHone, J.F., Greeley, R., Williams, K.K., Blumberg, D.G., Kuzmin, R.O., 2002. Space shuttle observations of terrestrial impact structures using SIR-C and X-SAR radars. Meteorit. Planet. Sci. 37, 407–420. doi:10.1111/j.1945-5100.2002.tb00824.x

McNairn, H., Duguay, C., Brisco, B., Pultz, T.., 2002. The effect of soil and crop residue characteristics on polarimetric radar response. Remote Sens. Environ. 80, 308–320. doi:10.1016/S0034-4257(01)00312-1

Mei, S., Paulen, R., 2009. Using multi-beam radarsat-1 imagery to augment mapping surficial geology in northwest alberta, canada. Can. J. Remote Sens. 35, 1–22. doi:10.5589/m08-077

Michalski, J.R., Niles, P.B., 2010. Deep crustal carbonate rocks exposed by meteor impact on Mars. Nat. Geosci. 3, 751–755. doi:10.1038/ngeo971

Neish, C.D., Carter, L.M., 2014. Planetary Radar, in: Spohn, T., Johnson, T. (Eds.), Encyclopedia of the Solar System. Academic Press, London, UK, pp. 1133–1159.

Newman, J.D., Osinski, G.R., 2016. Geological mapping of the Tunnunik impact structure, Victoria Island, Canadian High Arctic, in: 47th Lunar and Planetary Science Conference. p. Abstract #1591. doi:10.1038/ngeo2474.

Oh, Y., 2004. Quantitative retrieval of soil moisture content and surface roughness from multipolarized radar observations of bare soil surfaces. IEEE Trans. Geosci. Remote Sens. 42, 596–601. doi:10.1109/TGRS.2003.821065

Osinski, G.R., Abou-Aly, S., Francis, R., Hansen, J., Marion, C.L., Pickersgill, a E., Tornabene, L.L., 2013. The Prince Albert Impact Structure, Northwest Territories, Canada: A New 28-km Diameter Complex Impact Structure, in: 44th Lunar and Planetary Science Conference. p. Abstract #2099.

Osinski, G.R., Lee, P., Spray, J.G., Parnell, J., Lim, D.S.S., Bunch, T.E., Cockell, C.S., Glass, B., 2005a. Geological overview and cratering model for the Haughton impact structure, Devon Island, Canadian High Arctic. Meteorit. Planet. Sci. 40, 1759–1776. doi:10.1111/j.1945-5100.2005.tb00145.x

Osinski, G.R., Pierazzo, E., 2012. Impact Cratering: Processes and Products. John Wiley & Sons.

Osinski, G.R., Spray, J.G., 2005. Tectonics of complex crater formation as revealed by the Haughton impact structure, Devon Island, Canadian High Arctic. Meteorit. Planet. Sci. 40, 1813–1834. doi:10.1111/j.1945-5100.2005.tb00148.x

Osinski, G.R., Spray, J.G., Lee, P., 2005b. A case study of impact-induced hydrothermal activity: The Haughton impact structure, Devon Island, Canadian High Arctic. Meteorit. Planet. Sci. 40, 1789–1812. doi:10.1111/j.1945-5100.2005.tb00147.x

Osinski, G.R., Spray, J.R., 2006. Shatter cones of the Haughton impact structure, Canada, in: Proceedings of the 1st International Conference on Impact Cratering in the Solar System. European Sapce Agency, pp. 95–99.

Overpeck, J., Hughen, K., Hardy, D., Bradley, R., Case, R., Douglas, M., Finney, B., Gajewski, K., 1997. Arctic Environmental Change of the Last Four Centuries. Science (80-.). 278, 1251–1256. doi:10.1126/science.278.5341.1251

Pavlic, G., Singhroy, V., Duk-Rodkin, A., Alasset, P.-J., 2008. Satellite data fusion techniques for terrain and surficial geological mapping, in: IEEE Geoscience and Remote Sensing Symposium. pp. 314–317. doi:10.1109/IGARSS.2008.4779346

Pour, A.B., Hashim, M., 2014. Structural geology mapping using PALSAR data in the Bau gold mining district, Sarawak, Malaysia. Adv. Sp. Res. 54, 644–654. doi:10.1016/j.asr.2014.02.012

Quantin, C., Flahaut, J., Clenet, H., Allemand, P., Thomas, P., 2012. Composition and structures of the subsurface in the vicinity of Valles Marineris as revealed by central uplifts of impact craters. Icarus 221, 436–452. doi:10.1016/j.icarus.2012.07.031

Raney, R.K., Spudis, P.D., Bussey, B., Crusan, J., Jensen, J.R., Marinelli, W., McKerracher, P., Neish, C., Palsetia, M., Schulze, R., Sequeira, H.B., Winters, H., 2011. The lunar mini-RF radars: Hybrid polarimetric architecture and initial results. Proc. IEEE 99, 808–823. doi:10.1109/JPROC.2010.2084970

Rowan, L.C., Goetz, A.F.H., Ashley, R.P., 1977. Discrimination of hydrothermal altered and unaltered rocks in visible and near infrared multispectral images. Geophysics 42, 522–535. doi:10.1190/1.1440723

Rowan, L.C., Hook, S.J., Abrams, M.J., Mars, J.C., 2003. Mapping hydrothemally altered rocks at Cuprite, Nevada, using the Advanced Spaceborne Thermal Emission And Reflection Radiometer (ASTER), a new satellite-imaging system. Econ. Geol. 98, 1019–1027. doi:10.1016/S0361-1124(78)80358-X

Rowan, L.C., Mars, J.C., 2003. Lithologic mapping in the Mountain Pass, California area using Advanced Spaceborne Thermal Emission and Reflection Radiometer (ASTER) data. Remote Sens. Environ. 84, 350–366. doi:10.1016/S0034-4257(02)00127-X

Running, S.W., Way, J.B., McDonald, K.C., Kimball, J.S., Frolking, S., Keyser, A.R., Zimmerman, R., 1999. Radar remote sensing proposed for monitoring freeze-thaw transitions in boreal regions. Eos (Washington. DC). 80, 213–221. doi:10.1029/99EO00158

Sabins, F.F., 1999. Remote sensing for mineral exploration. Ore Geol. Rev. 14, 157–183. doi:10.1016/S0169-1368(99)00007-4

Saint-Jean, R., Singhroy, V., Rheault, M., 1999. Multi-polarized airborne C-SAR images for geological mapping at lac volant, Québec, in: 13th Applied Geological Remote Sensing Workshop.

Salisbury, J.W., D'Aria, D.M., 1992. Emissivity of terrestrial materials in the 8-14 μm atmospheric window. Remote Sens. Environ. 42, 83–106. doi:10.1016/0034-4257(94)90102-3

Schaber, G.G., Elachi, C., Farr, T.G., 1980. Remote sensing data of SP Mountain and SP Lava flow in North-Central Arizona. Remote Sens. Environ. 9, 149–170. doi:10.1016/0034-4257(80)90005-X

Scheuchl, B., Flett, D., Caves, R., Cumming, I., 2004. Potential of RADARSAT-2 data for operational sea ice monitoring. Can. J. Remote Sens. 30, 448–461. doi:10.5589/m04-011

Shelat, Y., Leblon, B., LaRocque, A., Harris, J., Jefferson, C.W., Lentz, D., Tschirhart, V., 2012a. Effects of incidence angles and image combinations on mapping accuracy of surficial materials in the Umiujalik Lake area, Nunavut using RADARSAT-2 polarimetric SAR, LANDSAT-7 ETM+ and DEM data. Part 1. Non-Polarimetric Analysis. Can. J. Remote Sens. 38, 383–403.

Shelat, Y., Lentz, D., Leblon, B., LaRocque, A., Harris, J., Jefferson, C., Tschirhart, V., 2012b. Effects of incidence angles on mapping accuracy of surficial materials in the Umiujalik Lake area, Nunavut, using RADARSAT-2 polarimetric SAR images. Part 2. Polarimetric analysis. Can. J. Remote Sens. 38, 404–423. doi:10.5589/m12-031

Sherlock, S.C., Kelley, S.P., Parnell, J., Green, P., Lee, P., Osinski, G.R., Cockell, C.S., 2005. Re-evaluating the age of the Haughton impact event. Meteorit. Planet. Sci. 40, 1777–1787.

Singhroy, V., Molch, K., 2004. Geological case studies related to RADARSAT-2. Can. J. Remote Sens. 30, 893–902. doi:10.5589/m04-050

Smith, S.K., Grieve, R.A.F., Harris, J.R., Singhroy, V., 1999. The utilization of RADARSAT-1 imagery for the characterization of terrestrial impact landforms. Can. J. Remote Sens. 25, 218–228. doi:10.1080/07038992.1999.10874721

Stewart, S.T., Valiant, G.J., 2006. Martian subsurface properties and crater formation processes inferred from fresh impact crater geometries. Meteorit. Planet. Sci. 41, 1509–1537. doi:10.1111/j.1945-5100.2006.tb00433.x

Tornabene, L.L., Moersch, J.E., Osinski, G.R., Lee, P., Wright, S.P., 2005. Spaceborne visible and thermal infrared lithologic mapping of impact-exposed subsurface lithologies at the Haughton impact structure, Devon Island, Canadian High Arctic: Applications to Mars. Meteorit. Planet. Sci. 40, 1835–1858. doi:10.1111/j.1945-5100.2005.tb00149.x

Touzi, R., Hurley, J., Vachon, P.W., 2015. Optimization of the degree of polarization for enhanced ship detection using polarimetric RADARSAT-2. IEEE Trans. Geosci. Remote Sens. 53, 5403–5424.

Ulaby, F.T., Moore, R.K., Fung, A.K., 1982. Microwave remote sensing : active and passive. Artech House, Norwood, MA.

van Der Meer, F.D., van Der Werff, H.M.A., van Ruitenbeek, F.J.A., Hecker, C.A., Bakker, W.H., Noomen, M.F., van Der Meijde, M., John, E., Carranza, M., Boudewijn De Smeth, J., Woldai, T., 2012. Multi- and hyperspectral geologic remote sensing: A review. Int. J. Appl. Earth Obs. Geoinf. 14, 112–128. doi:10.1016/j.jag.2011.08.002

Wall, J., Collingwood, A., Treitz, P., 2010. Monitoring surface moisture state in the Canadian High Arctic using synthetic aperture radar (SAR). Can. J. Remote Sens. 36, 124–134.

Chapter 2

2 Remote predictive mapping of the Tunnunik impact structure in the Canadian Arctic using multispectral and polarimetric SAR data fusion*

Byung-Hun Choe, Livio L. Tornabene, Gordon R. Osinski, and Jennifer D. Newman

2.1 Introduction

Minerals and rocks are characterized by diagnostic spectral features. These result from a rock reflecting, absorbing, and/or emitting the radiant solar energy at certain visible-near infrared (VNIR), short-wavelength infrared (SWIR), and thermal infrared (TIR) wavelengths depending on their material properties (see Clark et al., 1990a; Cooper et al., 2002; Hunt, 1977; Hunt and Salisbury, 1971, 1970; Salisbury and D'Aria, 1992, and references therein). Since these distinctive spectral properties can be used to constrain mineral and lithological composition of target surfaces, spectral analysis techniques, such as principal component analysis (PCA), band ratioing, and decorrelation stretching, have been successfully used for mineral and lithological mapping in various geological settings (e.g., hydrothermally altered rocks, volcanic deposits, iron ores, and Arctic bedrock) (e.g., Cloutis, 1996; Drury, 1993; Rowan et al., 2003; Rowan and Mars, 2003; Sabins, 1999, 1987; Tornabene et al., 2005; Van Der Meer et al., 2011, and references therein).

---

* This chapter article is currently in revision in *Canadian Journal of Remote Sensing* for publication with the same title.

In addition to spectroscopy, synthetic aperture radar (SAR) is well known for its ability to characterize the physical surface properties of target rocks such as surface roughness and dielectric properties (e.g., Ulaby et al., 1982). Minimal or non-vegetation cover in the Arctic is ideal for SAR imaging on structures and physical surface properties as well as spectral mapping of rock surfaces. In particular, extensive glacial erosion and deposition can form different surface roughness depending on rock types (McCarroll and Nesje, 1996), which can be readily imaged using polarimetric SAR and utilized for geological mapping (Singhroy et al., 1992). SAR also has a great advantage for Arctic mapping because it is independent of sunlight and capable of penetrating clouds by transmitting its own source at relatively long radio wavelengths (Running et al., 1999). Spectral sensors, on the other hand, are disturbed by cloud coverage and very limited in their ability to acquire clear images for geological mapping. However, despite extensive developments of high-resolution polarimetric SAR systems in recent years, few workers have utilized polarimetric SAR capabilities for geological mapping. Several studies have conducted lineament feature extraction and reported on the variation in radar backscattering from different geological units (e.g., Graham and Grant, 1991; Saint-Jean et al., 1999; Smith et al., 1999). Even though some studies have tried to develop mapping algorithms by integrating SAR sensors with multispectral data, polarimetric SAR was used only as supplementary input parameters to improve statistical classification accuracy using variations in spectral and/or polarimetric SAR parameters (Grunsky, 2002; LaRocque et al., 2012; Pavlic et al., 2008; Y. Shelat et al., 2012a; Shelat et al., 2012b).

The goal of this chapter is to further develop data fusion techniques to integrate spectral, physical, and morphological properties discerned from optical to microwave domains for remote predictive mapping (RPM). This study demonstrates how mineralogical and lithological information from multispectral analysis can be combined with physical surface properties derived from polarimetric SAR and high-resolution surface morphology to synergize RPM in the Canadian Arctic. As a case study, the Tunnunik impact structure in the Canadian Arctic was investigated using Advanced Spaceborne Thermal Emission and Reflectance Radiometer (ASTER), Landsat 8 Operational Land Imager (OLI), RADARSAT-2 quad polarimetric SAR, and Quickbird high-resolution optical data. The resultant remote predictive mapping was then ground truthed during a field campaign in July 2015. The Tunnunik structure was chosen as meteorite impacts are highly localized and complex structural geological features exposing multiple subsurface lithologies, which can be used to reconstruct a significant portion of the regional stratigraphic column (e.g., Tornabene et al., 2005). The extensive development of structural lineaments, such as fractures and faults, in impact structures is particularly conducive to SAR investigation (e.g., McHone et al., 2002; Smith et al., 1999). In addition, impact structures themselves are also important targets for resource exploration, as approximately 25% of impact structures on Earth possess economic resources (Grieve, 2012).

2.2 Methods and datasets used

2.2.1 Spectral datasets, calibration, and methods

Table 2.1 lists the technical specification of each remote sensing dataset used in this study. ASTER has three sensors sensitive to visible-near infrared (VNIR), short-wavelength infrared (SWIR), and thermal infrared (TIR) wavelengths (Abrams et al., 1995). ASTER Level 1A (AST_L1A) products are calibrated into Level 1B (AST_L1B) registered radiance by radiometric and geometric corrections, and then further processed into higher Level 2 products such as surface reflectance (AST_07 for VNIR/SWIR) and surface radiance (AST_09 for VNIR/SWIR and AST_09T for TIR) after atmosphere correction (Abrams et al., 1995). Surface emissivity (AST_05 for TIR) is produced after the Temperature-Emissivity Separation (TES) processing based on AST_09T surface radiance (Abrams et al., 1995). The digital number (DN) values of the Level 2 reflectance (8-bit) and emissivity (16-bit) are converted into floating point by multiplying each wavelength by the band scale factor (i.e., 0.001) (Abrams, 2000). This enables comparisons between image-derived spectra with laboratory-measured mineral and lithologic spectral libraries. Note that the ASTER SWIR sensor reported a crosstalk problem from stray light from band 4. Crosstalk-corrected SWIR data has been provided (Iwasaki and Tonooka, 2005), but unfortunately it is not feasible to collect SWIR data since April 2008 due to a thermal anomaly on the detector (see https://asterweb.jpl.nasa.gov/swir-alert.asp). Thus, ASTER SWIR bands were not used in this study as coverage of the Tunnunik impact structure was not acquired by ASTER until after 2008.

Landsat 8 Level 1 standard data products provide radiometrically calibrated and terrain-corrected (L1T) 16-bit DN data, which can be converted to Top of Atmosphere (TOA) reflectance using scaling factors with additional solar elevation angle corrections for TOA reflectance (U. S. Geological Survey, 2016). Here we use Landsat 8 VNIR/SWIR band reflectance data to fill in the gap from the lack of ASTER SWIR data and provide supplemental spectral information for our ASTER TIR emissivity spectral analysis. This analysis can constrain surface materials rich in iron oxides, clay minerals, and hydrothermally altered minerals (Goetz and Rowan, 1981; Harris et al., 2014; van Der Meer et al., 2012).

Here we employ several techniques to highlight the spectral characteristics of geologic materials in the scene, such as band ratios, principal component analysis (PCA), and spectral matching, which have been extensively used in previous studies for mineral and lithological mapping (e.g., Rowan and Mars, 2003; Tornabene et al., 2005; van Der Meer et al., 2012). All the pre-processing and spectral analysis were performed using the spectral processing modules of the Environment for Visualizing Image (ENVI) software. Firstly, to exclude spectral contributions from vegetation, water bodies, ice, and snow, and maximize the spectral variability of the well-exposed geologic surface materials (i.e., deposits or outcrops), image masking was conducted prior to employing various techniques for generating spectral maps. Vegetation was masked out by applying threshold values based off high reflectance at the NIR band relative to at the Red band (Tucker, 1979), and water bodies, ice, and snow were masked out by thresholding low reflectance at the NIR and/or SWIR bands (Harris et al., 2011).

Band ratioing is a technique employed to generate a greyscale image that emphasizes absorption features attributed to specific mineral or rock groups. The general idea for generating a multispectral band ratio image is dividing a band on the continuum (i.e., a flat and continuous portion of the spectrum) by a band that falls with an absorption feature or near the base of a steep-slope (e.g., Rowan et al., 1977; Tornabene et al., 2005; van Der Meer et al., 2012). This result is a greyscale image where the DN values generally reflect the absorption strength for a spectral feature being highlighted to emphasize the presence of a specific mineral or rock type. For example, the mineral calcite has an absorption feature at 11.2 μm in the TIR, which corresponds to ASTER band 14 (Rockwell and Hofstra, 2008; Rowan and Mars, 2003). As such, a ratio of band 13 to 14 (i.e., b13/b14) provides a band strength greyscale image, where the highest DN values highlight the pixels with the strongest absorptions, indicating the areas in the scene with the best exposure and/or the highest concentrations of calcite. Various band ratios for ASTER and Landsat platforms have been proposed for mapping specific minerals and lithologies (van Der Meer et al., 2012). We applied these band ratios to our ASTER and Landsat 8 scenes to produce spectral maps and provide guidance for a more rigorous spectral analysis of image-derived spectra. RGB colour composites were produced by combining different band ratios. These are particularly useful in classifying distinct spectral units.

The minimum noise fraction (MNF) transform is a type of PCA, but it rotates input bands to minimize noise fraction (i.e., maximize signal to noise ratio) using an estimated noise covariance matrix, while PCA is based on maximizing the spectral variance (Green et al., 1988). As a result, the most spatially coherent signals decorrelated from noise are reassigned into the first band, and noise fraction increases with increasing component number (i.e., image quality decreases) (Harris et al., 2005; Tornabene et al., 2005). By combining higher-ranked MNF bands (i.e., MNF band 1 is the top rank) into a RGB colour composite, a relatively noise-free spectral map can be derived. An MNF transformed ASTER TIR emissivity colour composite was produced and compared with ASTER and Landsat 8 band ratio colour composites. Based on spectrally and morphologically distinct units showing similarities and consistencies between spectral maps generated from ASTER and Landsat 8, we defined regions of interest (ROIs).

We investigated ASTER TIR emissivity spectra of each ROI using spectra averaging, window averaging, and ROI tools, and derived a statistically consistent and representative spectrum for each ROI by averaging 30 sample spectra with a standard deviation less than 0.01. The ASTER TIR averaged emissivity spectra were then matched to a whole-rock (Ward's) spectral library (Christensen et al., 2000) provided by Arizona State University by applying spectral angle mapper (SAM) and spectral feature fitting (SFF) algorithms. The SAM represents the fit of a target spectrum to a reference spectrum (e.g., a "known" spectrum for a material measured in the lab) by calculating the angle between the two spectra in n-dimensional vector space (i.e. number of bands, for example the ASTER TIR 5 bands have a 5-dimensional vector); if an image-derived spectrum were to perfectly match the reference spectrum, the vector angle is 0 giving the reference spectrum a score of 1.0 based on the cosine function (Kruse et al., 1993). Imperfect matches essentially have scores less than 1.0, with most good matches for a known/unknown falling in the 0.9 to 1.0 range. The SFF calculates the correlation coefficient of the least-squares fit on absorption features of the two spectra after removing the spectral continuum, which scores 1.0 for the perfect match and less than 1.0, similarly as described for the SAM matching above, for imperfect matches (Clark et al., 1990b).

2.2.2 RADARSAT-2 dataset, calibration, and methods

The RADARSAT-2 quad polarimetric SAR data was acquired at the Single Look Complex (SLC) level (Thompson and McLeod, 2004). The SLC product was pre-processed through radiometric calibration, multi-looking (by 2-look processing in the azimuth direction to make the ground pixel close to a square), speckle filtering (by the enhanced Lee filter with a 5 by 5 window), and geometric correction (at 10 m by 10 m pixel spacing) in that order, using the Polarimetric SAR Data Processing and Education Tool (PolSARpro) (Lee and Pottier, 2009). Then, the second-order covariance [C] and coherency [T] matrices were generated for microwave scattering mechanism analysis using polarimetric SAR decomposition theorems (Cloude and Pottier, 1996, see Appendix A).

With the recent development of high-resolution polarimetric SAR sensors, many studies have developed polarimetric decomposition techniques (Lee and Pottier, 2009). These techniques enable us to investigate microwave scattering mechanisms on target surfaces based on the polarimetric state changes of transmitted signals caused by physical properties of target surfaces (Cloude and Pottier, 1996). Thus, scattering mechanism analysis can indicate distinct geological units in physical surface properties such as surface roughness and morphology. Importantly, it is well known that different lithologies weather in different ways (i.e., grain-size and angularity) (Bandis et al., 1983). For example, relatively thick and massive carbonates in the Arctic are more resistant to weathering and form prominent cliffs and/or blocky boulder fields; conversely, thinly laminated shales and siltstones are typically recessive on steep slopes and weathered to relatively smooth, fine-grained scree deposits (Dredge, 1992; Hudec, 1973). As such, the erosional expressions of these rocks and associated deposits can be translated into very different radar scattering signatures (Smith et al., 1999). Here we applied Pauli, Freeman-Durden (FD), and Entropy-Alpha ($H\alpha$) polarimetric decomposition techniques to RADARSAT-2 quad polarimetric data to determine the dominant scattering mechanism from each geological unit in/around the Tunnunik impact structure (see Appendix B). The Pauli decomposition reconstructs target surfaces into three scattering components, such as single-bounce scattering from a plane surface, double-bounce scattering from a dihedral corner, and double-bounce scattering from a 45° oriented dihedral corner, based on simple algebraic combinations of polarimetric channels using the Pauli spin matrix basis (Cloude and Pottier, 1996). The FD decomposition describes the three scattering components by physically modeling a very smooth Bragg surface (single-bounce scattering), a dihedral corner (double-bounce scattering), and a forest canopy of randomly oriented thin cylinder-like scatters (multiple/volume scattering) (Freeman et al., 1998). The $H\alpha$ decomposition is based on the entropy and alpha angle parameters derived from eigenvalue and eigenvector analysis of the scattering matrix. Entropy represents the randomness of the scattering mechanisms ranging 0 to 1 (approaching to 0 for only a single dominant scattering), and alpha angles determine the type of scattering mechanisms among the single-bounce, double-bounce, and multiple/volume scattering depending on their degrees (Cloude and Pottier, 1997).

2.2.3 Remote Predictive Mapping (RPM) and additional supporting datasets: Quickbird and Canadian Digital Elevation Model (CDEM)

Quickbird is an ultrafine-resolution commercial satellite providing four VNIR bands (blue, green, red, and NIR) at a pixel spacing of 2.44 m and a panchromatic band at 0.61 m (Toutin and Cheng, 2002). Basic Imagery products are radiometrically corrected 11-bit DNs, which are processed into Standard Imagery products after geometric correction and map projection which are available with pan-sharpening at 0.61 m, and further processed into

Orthorectified Imagery products with absolute positioning accuracy using a DEM and ground control points (GCPs) (Toutin and Cheng, 2002).

Table 2.1. Specifications of remote sensing datasets used in Chapter 2

	Band (wavelength, µm)	**Pixel spacing (m)**	**Acquisition date/mode**
Landsat 8 OLI	1: Aerosol (0.435-0.451) 2: Blue (0.452-0.512) 3: Green (0.533-0.590) 4: Red (0.636-0.673) 5: NIR (0.851-0.879) 6: SWIR-1 (1.566-1.651) 7: SWIR-2 (2.107-2.294)	30	- 2013. 07. 02 - Level 1 standard data product (LC80550092013183LGN00)
ASTER	10 TIR (8.125-8.475) 11 TIR (8.475-8.825) 12 TIR (8.925-9.275) 13 TIR (10.25-10.95) 14 TIR (10.95-11.65)	90	- 2014. 08. 14 - On-Demand Level 2 product (AST_05_00308142014200146)
RADARSAT-2	C-band (5.6 cm)	4.7 * 5.1 (slant range * azimuth)	- 2012. 06. 08 - Wide Fine Quad polarization (HH/HV/VH/VV) - Incidence angle: 24.9-28.3° (FQ7W)
Quickbird	Pan (0.45-0.90)	0.61	- 2012. 07. 03/ 2012. 07. 12 (Orthomosaic) - Pan-sharpened
	Blue (0.45-0.52) Green (0.52-0.60) Red (0.63-0.69) NIR (0.76-0.90)	2.44	

The CDEM provides DEM tiles with complete coverage of Canada at the scale of 1:50,000 (available at http://geogratis.gc.ca/site/eng/extraction). A CDEM mosaic covering the Tunnunik impact structure was acquired at the grid resolution of 1.5 by 0.75 arc seconds (~23 by 11 metres). Based on the orthorectified and pan-sharpened Quickbird image rendered on the DEM, we investigated more detailed surface textures (e.g., colour/tone, homogeneity, layering) and morphological features (e.g., glacial striations, periglacial polygons, gullies), and structural lineaments (e.g., faults, joints). All the processed data were integrated in ArcGIS using the same coordinate system (Universal Transverse Mercator (UTM), Zone 11 North).

Based on our preliminary image interpretations, a decision-tree based algorithm was developed to automatically produce a remote predictive map. The decision-tree approach has been applied to a variety of pattern recognition and classification tasks because of its computational simplicity and intuitive interpretability for classes defined (Swain and Hauska, 1977). In particular, its non-parametric nature does not require statistical distribution between input parameters (Friedl and Brodley, 1997), while statistical classification and mapping based on spectral variance by combining a variety of spectral bands and band ratios (e.g., Maximum Likelihood classification (Strahler, 1980), Robust Classification Method (Harris et al., 2012)) can result in uncertain or unclassified areas in case input parameters are not statistically consistent (Harris et al., 2014). Here we employed a specified range of thresholds of Landsat 8 VNIR/SWIR, ASTER TIR, and RADARSAT-2 polarimetric SAR parameters into a decision-tree to characterize lithological and surface roughness properties of each geological unit.

2.2.4 Ground-truth and subsequent sample analysis

Field work was carried out at the Tunnunik impact structure over the course of a month in July and August 2015. We investigated the defined units based on our remote predictive mapping and collected representative rock samples. Collected rock samples were analyzed by powder X-ray diffraction (XRD) to semi-quantitatively identify the mineral compositions present. Using a mortar and pestle, samples were ground into a very fine powder and then mounted onto powder mounts. Mounted samples were analyzed in the X-ray Diffraction and Microdiffraction Laboratory in the Department of Earth Sciences at the University of Western Ontario using a Rigaku DMAX Geigerflex diffractometer. XRD measurements were collected from 10° to 90° 2θ at a 0.02° step size with operating conditions of Co Kα radiation (λ = 1.79021 Å), 66 minutes run time, accelerating voltage of 40 kV and beam current of 35 mA. XRD patterns were analyzed with Bruker-AXS EVA software.

2.3 Results

To characterize the geology of the Tunnunik impact structure, we integrated all the compositional, surface roughness, texture and morphological properties derived from the multispectral and polarimetric SAR observations. A total of four distinct spectral units were defined as summarized in Table 2.2. Below, we first outline the observations from the individual remote sensing datasets before integrating the observations from all the datasets employed in our study to more completely define the geological units.

2.3.1 ASTER TIR emissivity

A total of four distinct spectral units were recognized in the MNF colour composite (Fig. 2.1). The representative spectra of the orange-yellow (Unit 1) and magenta (Unit 4) units similarly show strong absorptions in TIR bands 10 and 12 (Figs. 2.1a and 2.1d). The cyan unit (Unit 2) shows absorptions at band 12 and band 14 (Fig. 2.1b). The green unit (Unit 3) shows a dominant absorption only at band 14 (Fig. 2.1c). The absorptions at band 10 (centred at 8.3 μm) and band 12 (9.1 μm) are the main absorption feature of silica, and the absorption at band 14 (11.3 μm) is associated with carbonates (Rockwell and Hofstra, 2008). The spectral matching results indicate that the best matching rock candidates were siltstone (for orange-yellow and magenta units), cherty limestone (cyan unit), and dolomitic limestone (green unit), respectively.

Based on the absorption features, band ratio images were produced to emphasize the carbonate and silica signatures by applying (b10+b13)/b14 and b13/b12, respectively. In general, the band ratio of b13/b14 is used to extract the carbonate absorption at band 14 (van Der Meer et al., 2012), but (b10+b13)/b14 was applied instead. As orange-yellow and magenta units show a weak absorption at band 14, not only at band 10 and 12, band 10 at which the carbonate units (cyan and green units) have little absorption was additionally incorporated into the band ratio for better differentiation. The carbonate signatures are concentrated in the eastern structure around the green unit (Unit 3) in the MNF composite (Fig. 2.2a). The dominant silica signatures are consistently observed in the orange-yellow (Unit 1) and magenta colour units (Unit 4) in the MNF composite (Fig. 2.2b).

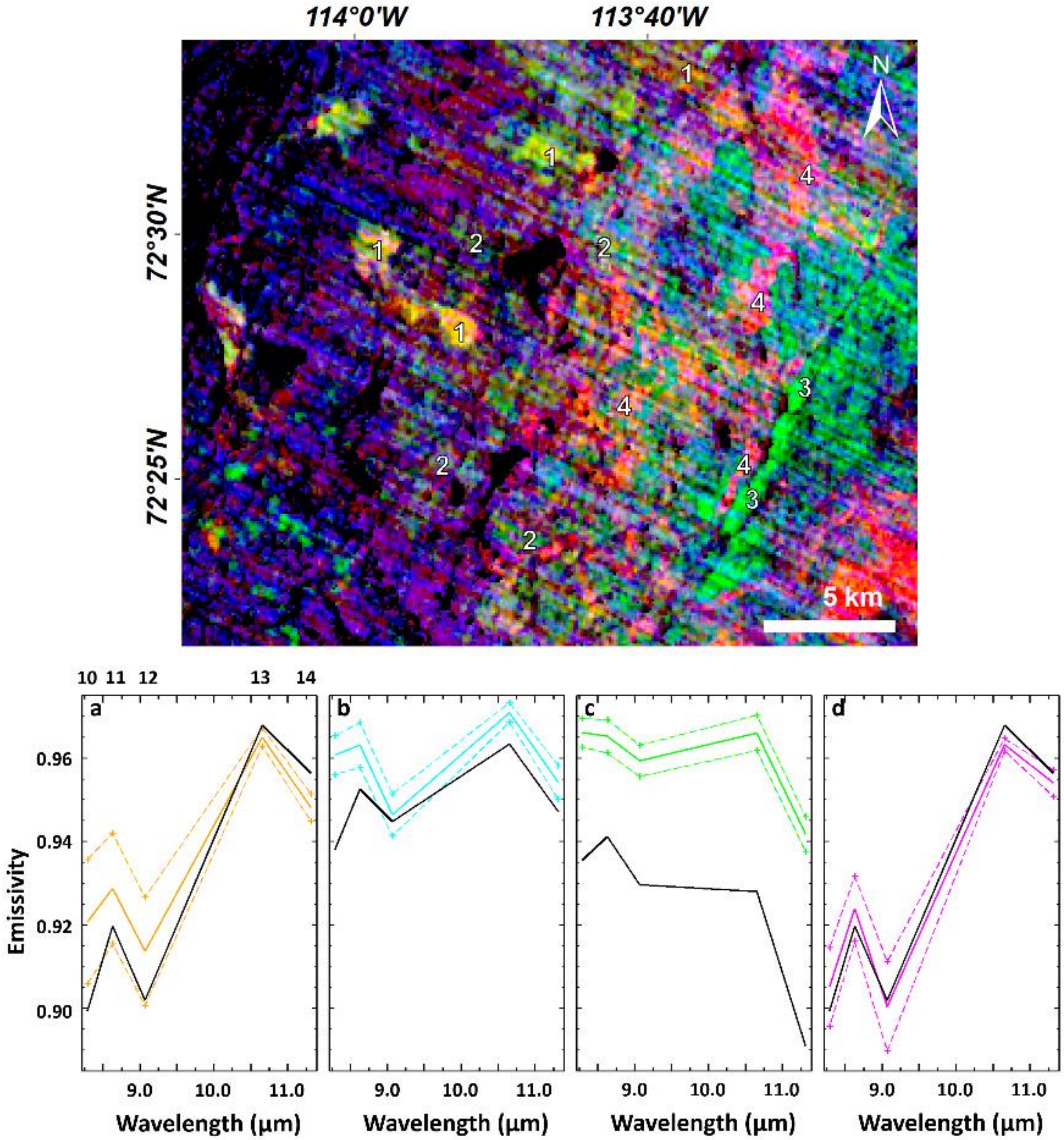

Figure 2.1. MNF transformed ASTER TIR emissivity RGB color composite (upper, R; MNF band 1, G; band 2, B; band 3 by applying a linear 2% stretch) and TIR emissivity spectra matching results (bottom). Vegetation and water bodies in the MNF composite were masked out in black. The white numbers on the MNF composite represent the 4 spectral units discussed in the text. The coloured lines are the averaged TIR emissivity spectra (solid) of representative 30 samples from each unit and its standard deviation (dashed with markers); (a) orange-yellow, (b) cyan, (c) green, and (d) magenta units. The solid black lines are the best matching rock spectra from the ASU Ward's whole-rock spectral library (Christensen et al. 2000); (a) siltstone, (b) cherty limestone, (c) dolomitic limestone, and (d) siltstone. The black numbers (10-14) on the top X axis represent ASTER TIR bands corresponding to wavelengths listed in Table 2.1.

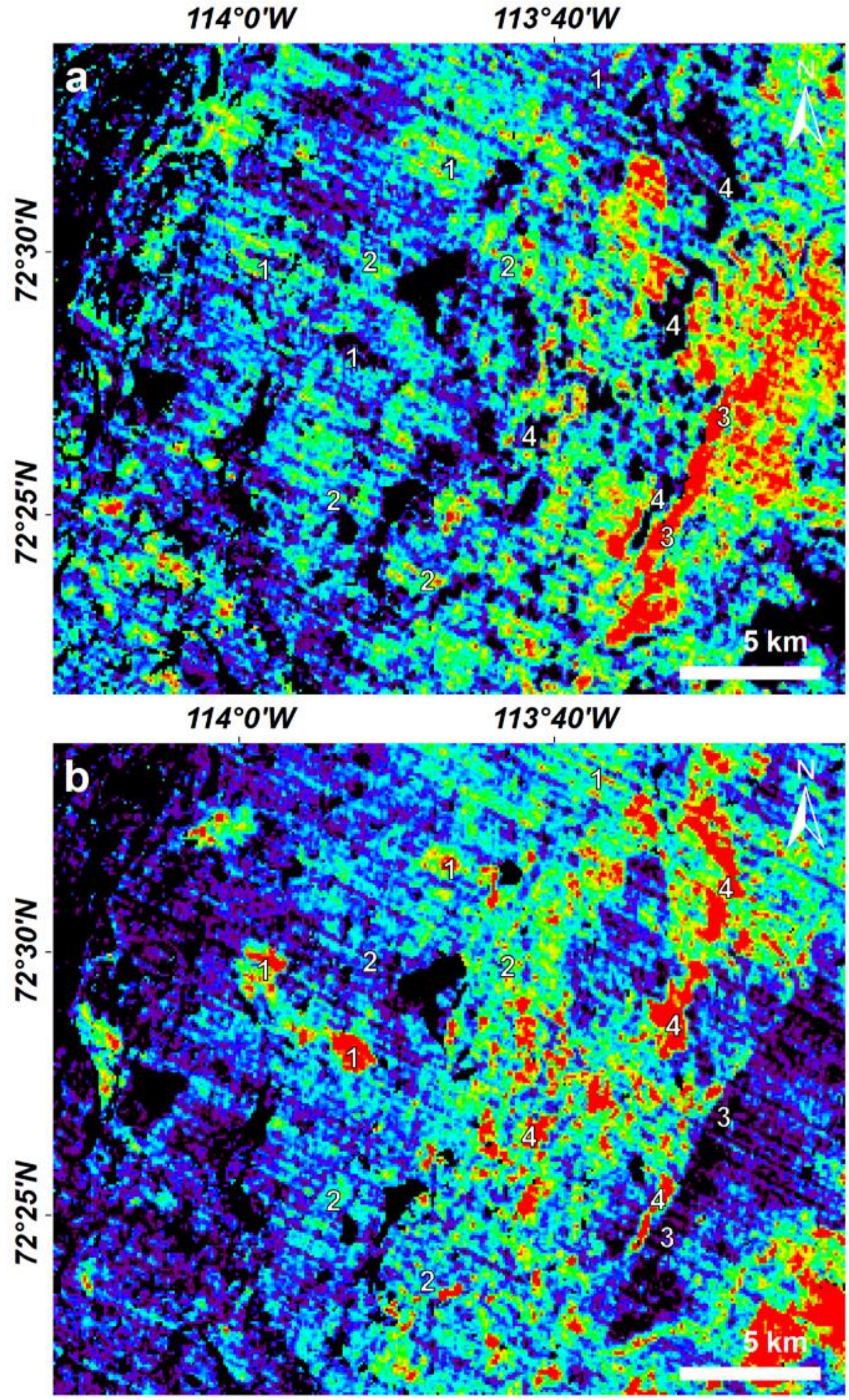

Figure 2.2. ASTER TIR band ratio images. (a) (b10+b13)/b14 for carbonates. (b) b13/b12 for silica. They were coloured in purple (low) to red (high) at the range of (a) 1.99-2.04 and (b) 1.00-1.05, respectively by applying a linear 2% stretch. Vegetation and water bodies were masked out in black.

2.3.2 Landsat 8 VNIR/SWIR reflectance

A Landsat 8 band ratio colour composite was constructed by combining the following band ratios; b6/b5, b6/b7, and b4/b2. These are known to be sensitive to ferrous iron (Fe^{2+}), clay/carbonates/sulfates, and ferric iron (Fe^{3+}), respectively (Drury, 1993; Harris et al., 2014; van Der Meer et al., 2012). This composite also defined 4 different spectral units (i.e. red, yellow-green, magenta, and purple as numbered in Fig. 2.3) similarly to the ASTER MNF composite. Overall, b6/b7 (clay/carbonates/sulfates) signatures are significant over the whole structure, which are represented in yellow-green depending on the portion of ferric iron signatures in the red channel (Unit 2, Fig. 2.3). A dumbbell-shaped feature coloured in red near the centre of the structure shows relatively strong ferric iron signatures suggesting the presence of iron-oxidized minerals (Unit 1, Fig. 2.3). In the eastern parts of the structure, a very narrow and long tadpole-shaped structure along the NE-SW trending regional fault line is distinctively represented in magenta (Unit 3, Fig. 2.3), and subsequently purple coloured units (Unit 4, Fig 2.3) appear depending on the portions of ferric and ferrous iron signatures.

2.3.3 Polarimetric SAR decomposition

Three different main units are apparent in the polarimetric decompositions (i.e., blue (Unit 1), purple (Unit 2), yellow (Unit 3 and 4) for the Pauli decomposition (Fig. 2.4a), and blue (Unit 1), cyan (Unit 2), green (Unit 3 and 4) for the FD decomposition (Fig. 2.4b)), which can be translated to smooth, moderately rough, and rough surfaces, respectively. Overall,

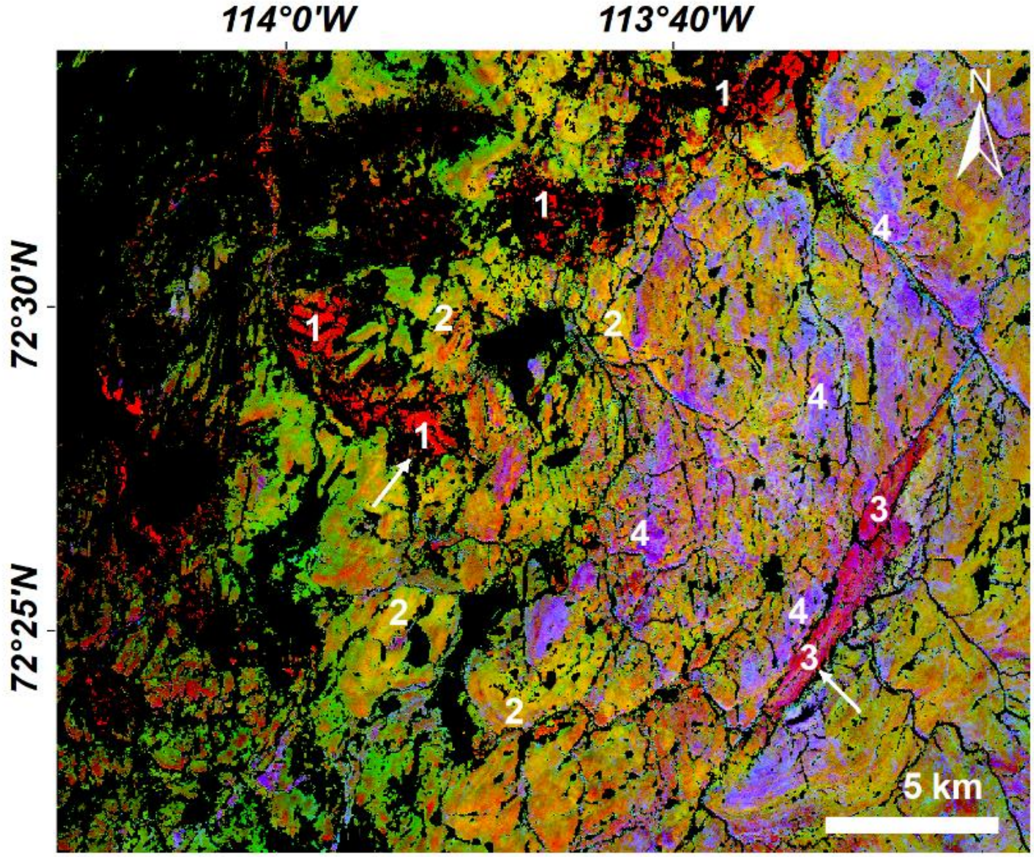

Figure 2.3. Landsat 8 OLI band ratio color composite (R; b4/b2 (1.00-1.20), G; b6/b7 (1.19-1.35), B; b6/b5 (1.31-1.49) by applying a Gaussian stretch with a standard deviation of 3). The majority of densely vegetated areas and water bodies were masked out in black. Remaining pixels dominated by green around channels and lakes are vegetated areas that were difficult to remove without adversely effecting mineral- and rock- dominated spectral units. The numbers represent the 4 spectral units discussed in the text. The white arrows indicate the dumbbell-shaped (left) and tadpole-shaped (right) features, respectively.

the central and western areas of the structure show relatively dominant single-bounce scattering features including very low entropy and mean alpha angle values ($H < 0.4$ and $\alpha < 15°$, Figs. 2.4c and 2.4d), which is consistent with very smooth surfaces (Cloude and Pottier, 1997). In the eastern structure, on the other hand, very strong multiple-diffused scattering is observed in the Pauli (Fig. 2.4a) and FD (Fig. 2.4b) decomposition results, suggesting that it comprises very rough and blocky surfaces. However, both composites showed a slightly different colour stretching in those surfaces assumed to be very rough and blocky. Specifically, they are represented by yellows in the Pauli composite resulting from the mixture of double-bounce and multiple-diffused scattering components, while greener in the FD composite indicating more dominant multiple-diffused scattering. The surrounding areas of channels and lakes showing residual vegetation signatures from the Landsat 8 band ratio composite (Fig. 2.3) do not show any multiple-diffused scattering and alpha angle values between 40° and 50°, which indicates they are not dense vegetation and forest, but only very sparse vegetation (Cloude and Pottier, 1997).

2.3.4 High-resolution Quickbird and CDEM

In the southeast corner of the Quickbird image adjusted by histogram equalization (Fig. 2.5a), a reddish brown unit is observed. This is consistent with the very narrow ASTER-based green unit and the Landsat 8-based magenta unit (i.e., Unit 3 in Figs. 2.1 and 2.3). The unit appears to correlate with what appears to be well-exposed bedrock unit with extensive fractures, striations or lineations as well as possessing what appears to be thinly layered features of different colours at the eastern edge (Fig. 2.5e). Above it, bluish grey units (Unit 4) are mapped in places, which we also interpret to be consistent with well-exposed bedrock. It features more frequent layering and/or deeply striated surfaces (Fig. 2.5f). Then, grainy surfaces (Unit 2) are followed with different colour tones of dark grey, grey, and light brown. Polygons interpreted to be periglacial and dissected terrain features

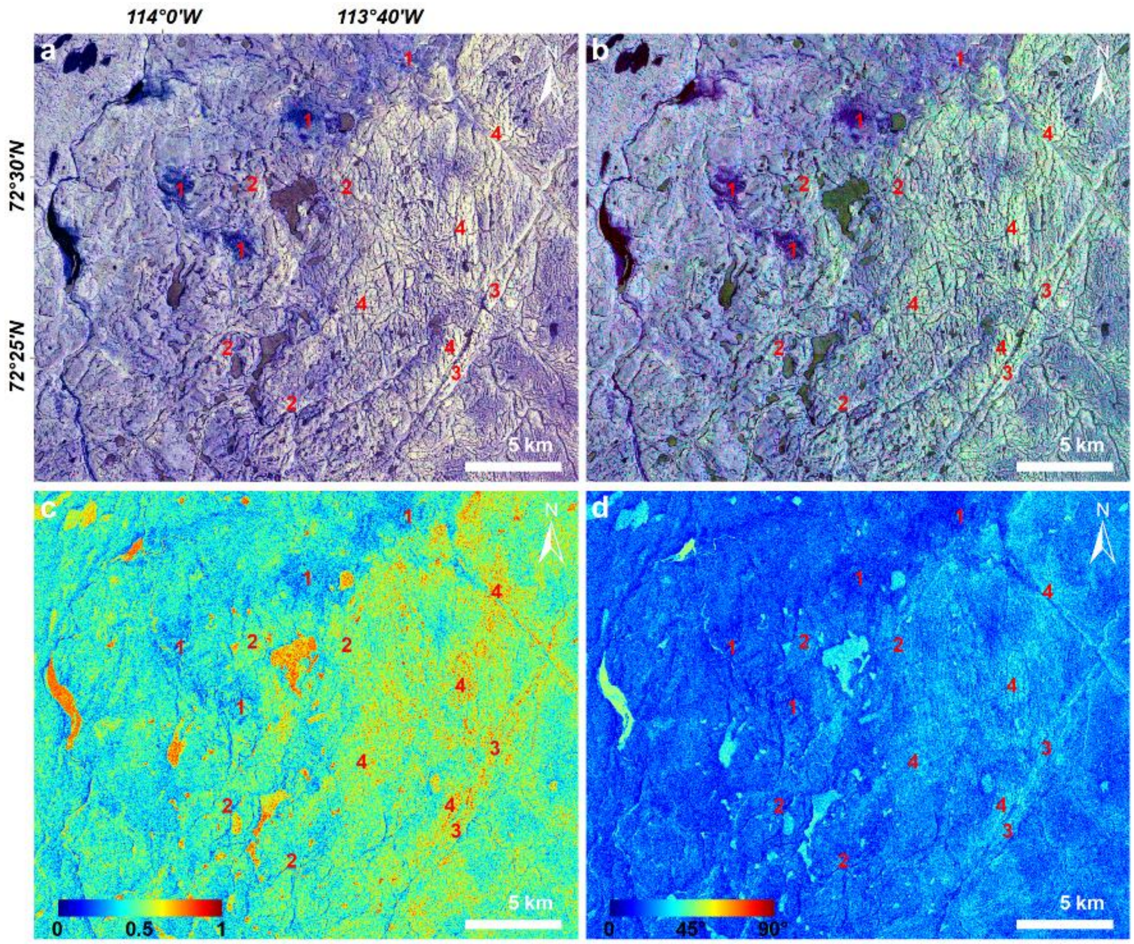

Figure 2.4. RADARSAT-2 polarimetric decomposition results. (a) Pauli RGB composite, (b) Freeman-Durden RGB composite, (c) entropy (*H*), and (d) alpha angles (α). The RGB composites of the Pauli and Freeman-Durden decomposition represent double-bounce scattering (red), multiple scattering (green), and single-bounce scattering (blue), respectively. The Pauli and Freeman-Durden histograms were linearly stretched at the same range from -25 to 0 dB.

are noticed (Fig. 2.5d). More massive and homogenous appearing lighter-toned surfaces (Unit 1) are placed in patches, which are interpreted to be homogeneous fine-grained deposits (Fig. 2.5c). In addition, gullies are observed to have been extensively developed along the edges of the deposits. The CDEM (Fig. 2.5b) shows a significant correlation between topography and surface roughness. Higher topography corresponds to rough and blocky surfaces (Unit 3 and 4) in the eastern structure observed from polarimetric SAR decompositions. Lower topography corresponds to very smooth fine-grained deposits (Unit 1) and moderately rough grainy surfaces (Unit 2).

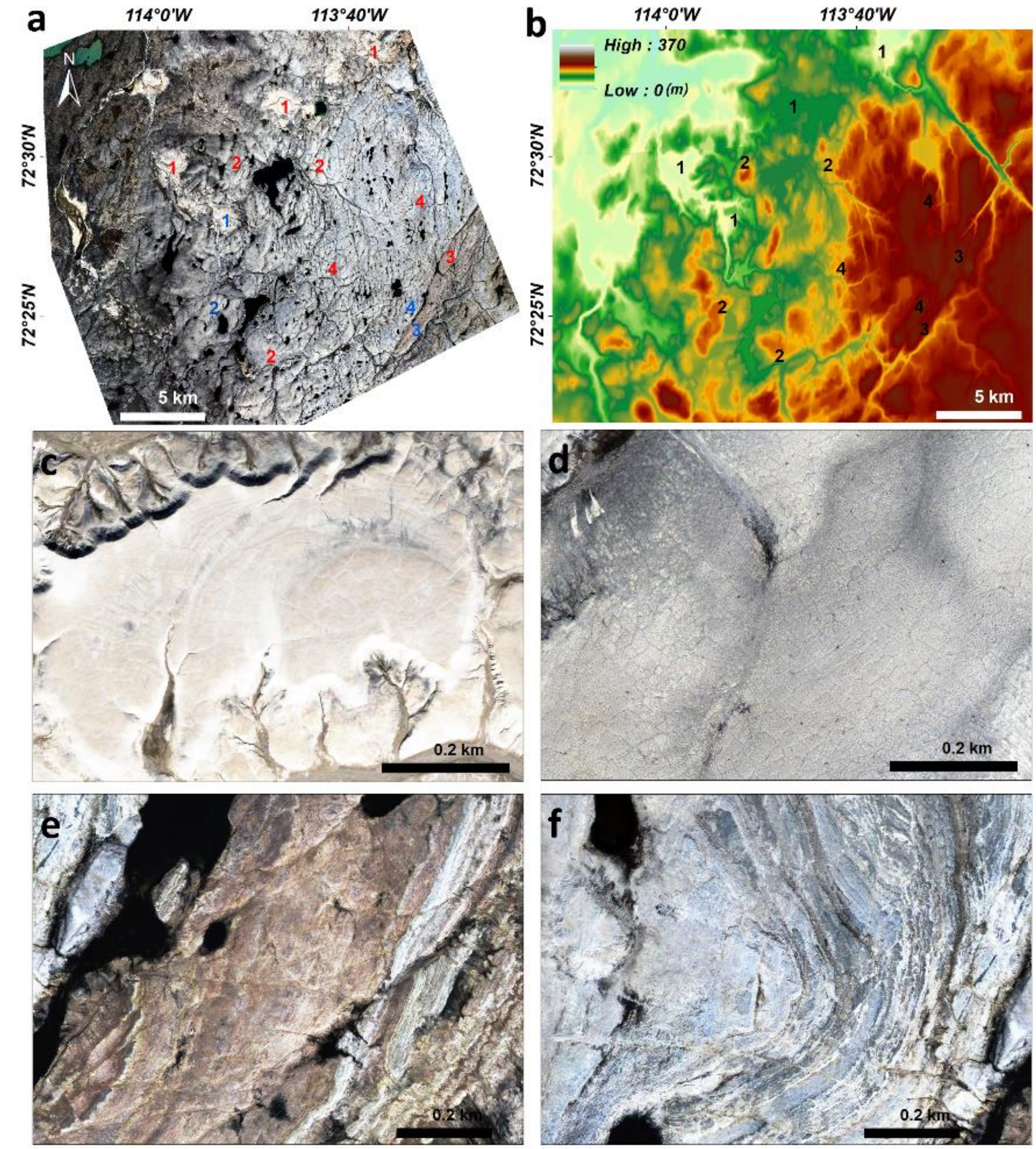

Figure 2.5. High-resolution Quickbird image (a, the RGB colour image was stretched by applying the histogram equalization for enhancing image contrast and classification), CDEM (b), and Quickbird image close-ups for each unit ((c) Unit 1, (d) Unit 2, (e) Unit 3, and (f) Unit 4). The blue numbers in (a) represent the locations of the close-ups.

2.4 Remote predictive mapping

2.4.1 Synthesis of remote sensing observations

A total of four distinct units were defined as summarized below and in Table 2.2. Unit 1 is the orange-yellow unit in the ASTER MNF composite (Fig. 2.1). The averaged TIR emissivity spectra for this unit indicated the presence of silica absorptions at band 10 and 12 that matches with the siltstone spectrum from the ASU spectral library (Fig. 2.1a). It also shows a very strong ferric iron signature (red) from the Landsat 8 band ratio composite (Fig. 2.3). RADARSAT-2 polarimetric decompositions confirm dominant single-bounce scattering in Unit 1 indicating very smooth surfaces (Fig. 2.4). Combined with our interpretations based on Quickbird and elevation data (Figs. 2.5a and 2.5b), this suggests that this unit is unconsolidated deposits having a very homogenous fine-grained surface texture (Fig. 2.5c), which consistently occurs as a restively flat-lying (low slope) deposit within local topographic lows (Fig. 2.5b). In addition, this unit is strongly associated with morphologic characteristics that give essential clues into its nature and origins. The unit occurs in where there are channels, lakes, and contains well-developed gullies and polygons. Based on the integrated information, including the context of the geologic setting, we interpreted Unit 1 to be a series of silica-dominated fluvio-lacustrine glacial deposits.

Unit 2 is the cyan (or mixed by blue and green) unit in the MNF composite (Fig. 2.1) and appears in yellow-green in the Landsat 8 band ratio composite (Fig. 2.3). The averaged TIR emissivity spectrum shows absorption features at band 12 as well as at band 14, and is matched to a cherty limestone spectrum from the ASU spectral library (Fig. 2.1b). Given that the main lithologies of Victoria Island and Thumb Mountain formations where the Tunnunik structure are and the widespread yellow-green units throughout the structure, the b6/b7 signatures of Landsat 8 are interpreted to represent materials dominated by carbonates rather than clay or sulfates. Unit 2 has a similar morphological appearance to Unit 1, but appears coarser and less homogenous and greyish in colour in the Quickbird image (Fig. 2.5b) and occurs on slopes near higher standing terrain (Fig. 2.5b) and has a dissected morphologic appearance. Polarimetric decompositions observed single-bounce scattering (blue) as well as double-bounce and multiple scattering (yellow, in Fig. 2.4a) in Unit 2, which indicates moderately rough surfaces of fine-grained deposits and coarser boulders interspersed. It was interpreted to be cherty limestone.

Unit 3 is the narrow and spectrally distinct unit along the NE-SW trending regional fault line on the ASTER MNF (green, Fig. 2.1), Landsat 8 band ratio (magenta, Fig. 2.3), and Quickbird (reddish brown, Fig. 2.5c) images. The averaged TIR emissivity spectrum exhibits a strong absorption at band 14 and is best matched with a dolomitic limestone spectrum from the ASU spectral library (Fig. 2.1b). Polarimetric decompositions observed very strong multiple scattering with double-bounce scattering to some extent, which was represented by yellow in the Pauli composite (Fig. 2.4a). We interpret Unit 3 as dolomitic limestone bedrock weathered to very rough and blocky surfaces.

Unit 4 is represented in purple in the ASTER MNF composite (Fig. 2.1) and magenta in the Landsat 8 band ratio composite (Fig. 2.3). It appeared bluish grey bedrock with very thin and frequent linear and quasi-linear features at intervals of approximately 3 to 10 m in the Quickbird image (Fig. 2.5d). The averaged TIR emissivity spectrum shows absorptions at band 10 and 12, a slight deflection at band 14 suggests some carbonate may be present, but the overall spectral character is consistent with silica-rich and similar to Unit 1 matched to the siltstone spectrum (Fig. 2.1d). The dominant scattering mechanism, however, is multiple and double-bounce scatterings in contrast to Unit 1 (Fig. 2.4a). Unit 4 was interpreted to be weathered rough and blocky silica-bearing bedrock. In particular, weathered rough surfaces in Unit 3 and Unit 4 are closely correlated with higher topography in the eastern structure, which can be related to glacial processes of this region (Briner et al. 2008). It is presumed that there has been extensive glacial action from higher elevations in the SE to lower elevations in the NW, resulting in glacial weathering, erosion, and deposition. Massive carbonate rocks relatively resistant to weathering could have been altered to blocky boulders and rock fragments at higher elevations (Units 3 and 4), while fluvio-lacustrine depositional environment could have been formed at middle (Unit 2) and lower (Unit 1) elevations.

Table 2.2. Colour scheme and characteristics of each unit derived from different remote sensors

	ASTER	**Landsat8**	**RADARSAT-2***	**Quickbird**
Unit 1	orange-yellow (silica)	red (Fe^{3+})	blue (smooth)	white (homogeneous, fine-grained)
Unit 2	cyan (cherty limestone)	yellow-green (carbonate)	purple (moderate rough)	grey (relatively homogeneous, grainy)
Unit 3	green (dolomitic limestone)	magenta ($Fe^{3+} > Fe^{2+}$)	yellow (rough)	reddish brown (layered bedrock)
Unit 4	magenta (silica)	purple ($Fe^{2+} \approx Fe^{3+}$)	yellow (rough)	bluish grey (layered bedrock)

* Pauli RGB composite (Fig. 2.4a) was applied here.

2.4.2 Decision-tree based algorithm

Rather than manually delineating the 4 units described above, a decision-tree based algorithm was employed to produce a remote predictive map (Fig. 2.6). First, surfaces covered by sparse vegetation in the western structure were masked out to remove additive spectra effects from vegetation spectra for effective geological mapping by applying high thresholds of the Landsat 8 b5/b4 (>1.45) and b7/b5 (>1.3). Unit 1 (dumbbell-shaped) and Unit 3 (tadpole-shaped) with very distinct shapes in limited areas were extracted. For Unit 1 showing strong ferric iron-bearing and silica-bearing signatures and smooth surfaces, a high threshold of the Landsat 8 b4/b2 (>1.1) and ASTER b13/b12 (>1.03), and a low threshold of the RADARSAT-2 multiple scattering component (<-22dB) were applied. Unit 3 was characterized by relatively high concentration of carbonate signatures (Fig. 2.3a) among rough and blocky surfaces in the eastern structure (Fig. 2.4a), so high thresholds of the ASTER (b10+b13)/b14 (>2.03) and RADARSAT-2 multiple scattering (>-20dB) were applied. A low threshold of the Landsat 8 b6/b7 (<1.27) was additionally considered because it showed much lower values in the b6/b7 compared to the surrounding areas. Unit 4 showed much higher silica signatures from the ASTER TIR band ratio (Fig. 2.3b) and spectral matching (Fig. 2.2d), and rougher surfaces from the RADARSAT-2 decomposition (Fig. 2.4a) compared to Unit 2, so higher thresholds of the ASTER b13/b12 (>1.03) and RADARSAT-2 (>-20dB) were applied. The remaining areas were classified to Unit 2 representing moderate rough surfaces containing a certain amount of both silica- and carbonate-bearing spectral signatures. A remote predictive map to define the four geological units was produced by the proposed decision-tree algorithm (Fig. 2.7).

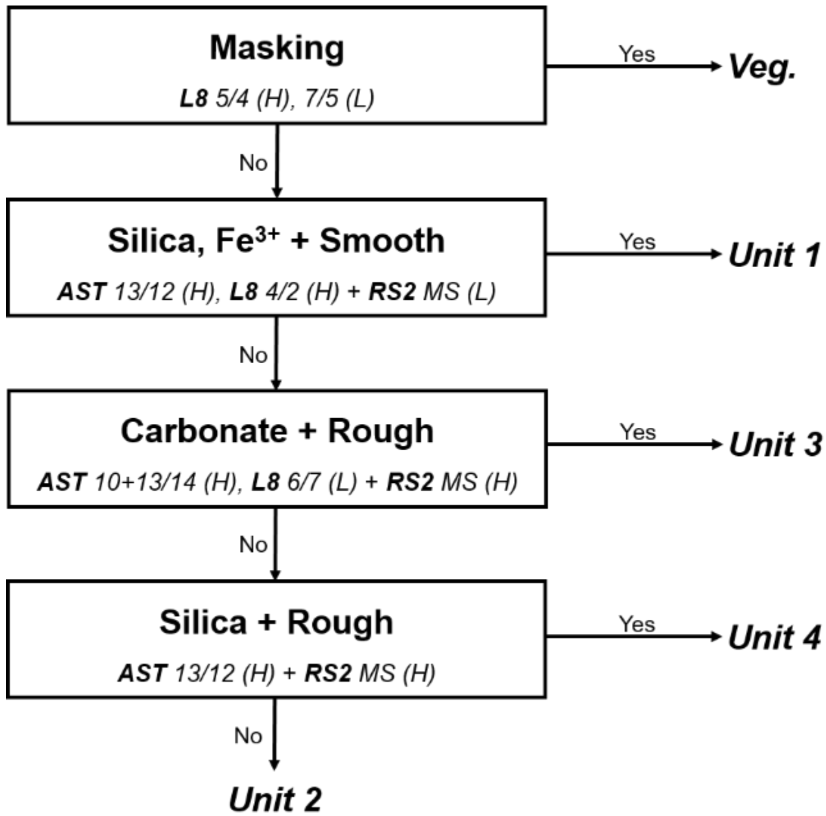

Figure 2.6. A decision-tree based algorithm for remote predictive mapping (‘Veg.’=vegetated surfaces, ‘L8’=Landsat8 VNIR/SWIR band ratio, ‘AST’=ASTER TIR band ratio, ‘RS2 MS’=RADARSAT-2 multiple-scattering, ‘H’=high threshold, and ‘L’=low threshold).

2.5 Ground truth: field and laboratory observations

2.5.1 Unit 1

In the region we defined as Unit 1, unconsolidated to partially indurated fluvio-lacustrine glacial deposits were observed in the field (Fig. 2.8a). As predicted, the surfaces are very smooth relative to the scale of the RADARSAT-2 data. XRD analysis confirmed dolomite,

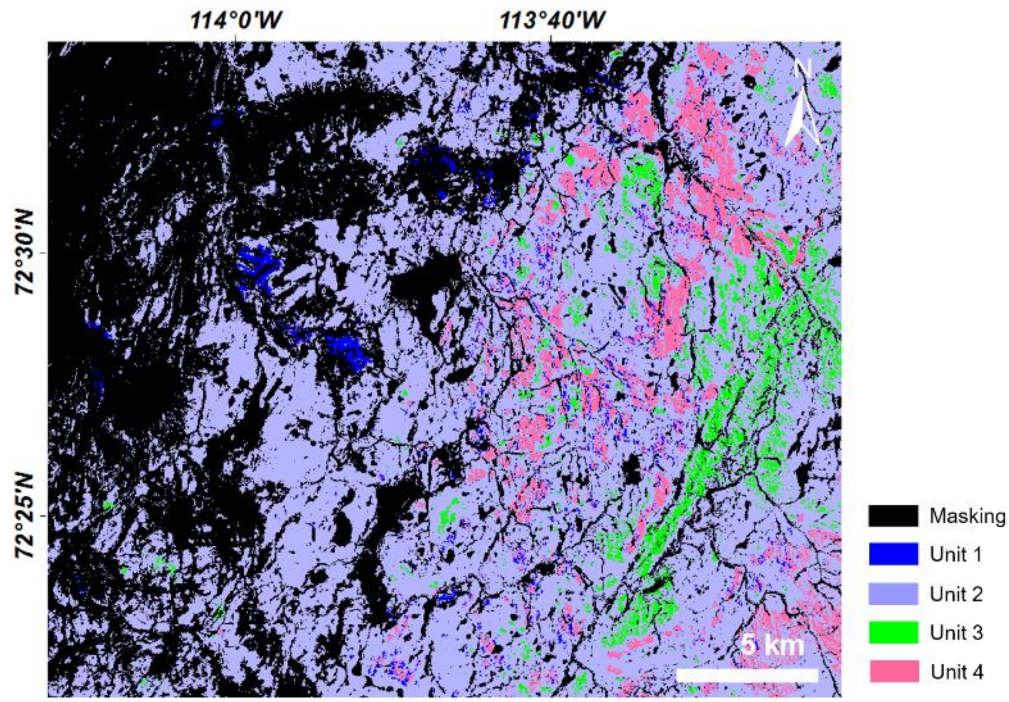

Figure 2.7. Remote predictive geological map of the Tunnunik impact structure. Vegetation and water bodies are masked out in black.

quartz, and a ferric iron phase (possibly nontronite) (see Fig. A.5 in Appendix E). It is suggested that the silica absorption features in ASTER TIR bands 10 and 12 (Fig. 2.1a) result from quartz, which is a dominant mineral in these deposits. The ferric iron signatures from the Landsat 8 band ratio composite (Fig. 2.1) indicate the presence of oxidized iron. Gullies and polygons, formed by recurrent seasonal melting of ice and snow, are widespread in Unit 1. Their presence and morphology are consistent with Unit 1 being partially indurated deposits.

2.5.2 Unit 2

In Unit 2, dolostone with abundant chert nodules were observed in the field (Fig. 2.8b). XRD analysis showed that it is mainly composed of dolomite, calcite, and quartz, with minor pyrite (see Fig. A.6 in Appendix E). The ASTER TIR emissivity spectra absorption at band 12 is attributed to microcrystalline quartz in the chert nodules and the TIR band 14 absorption is from the carbonate components (Fig. 2.8b). The pervasively fractured carbonate bedrock has formed rough surfaces, but unconsolidated sediments are also observed as discontinuous patches (Fig. 2.8c). It is represented by a certain amount of single-bounce scattering (Fig. 2.4) indicating moderate roughness relative to Unit 3 and Unit 4 (see below), and also appears as grainy and dissected surface texture on the Quickbird image (Fig. 2.5d). The relatively higher ferric iron signatures represented in yellow in the Landsat 8 band ratio composite (Fig. 2.3) may result from the surficial oxidation of the minor pyrite included in these rocks.

2.5.3 Unit 3

Field observations show that Unit 3 comprises dolostone (Fig. 2.8d). XRD mineralogical characterization of samples from Unit 3 confirm the high abundance of dolomite with minor amounts of quartz (see Fig. A.7 in Appendix E). The apparent absorption at ASTER TIR band 14 (Fig. 2.1c) is highly indicative of dolomite, and the ferric iron signatures from the Landsat 8 (Fig. 2.3) is likely the result of surficial Fe-staining. Very rough and blocky surfaces were observed, which is consistent with the polarimetric decomposition analysis (Fig. 2.4).

2.5.4 Unit 4

In Unit 4, we observed very rough and blocky outcrops of carbonates covered by silica-coatings (Figs. 2.8e and 2.8f). The main mineralogy based on the XRD analysis is dolomite and quartz (see Fig. A.8 in Appendix E). The higher abundance of quartz in these samples compared to Unit 3 is attributed to increased weathering, evident by the silica-coated weathered surfaces. Minor calcite was also detected. The TIR emissivity absorptions at band 10 and 12 (Fig. 2.1d) are from quartz concentrated within the silica-coated surfaces. Based on the dominant silica signature and the weak carbonate absorption for the image-derived averaged spectrum for unit 4 (Fig. 2.1d), it is clear that the extensive alteration and silica-coatings on the surfaces of these outcrops largely mask the underlying carbonate signatures at the spatial scale of the ASTER TIR emissivity data. Though both of Unit 1 and Unit 4 are matched to the same siltstone spectrum based on the similar silica absorptions from the TIR emissivity spectra (Figs. 2.1a and 2.1d), they show significant differences in ferric and ferrous iron signatures (Fig. 2.3) and texture (Figs. 2.5c and 2.5f), particularly in scattering mechanism (Fig. 2.4). Here, the physical surface properties observed from polarimetric SAR should be synthetically considered on top of the multispectral analysis. The double-bounce and multiple scatterings observed in Unit 4 (Fig. 2.4a) are attributed to the fragmented carbonate rocks. Unit 3 and Unit 4 has what appears to be a layered appearance in the Quickbird image (Figs. 2.5e and 2.5f). However, field observations revealed that the layering is actually alternating bands of differentially weathered outcrop and unconsolidated deposits (Fig. 2.8g). If Unit 3 and Unit 4 were well-exposed layered bedrock as appeared on the Quickbird image, they could have shown much more single-bounce scattering, not such strong multiple-diffused scattering observed in very blocky rock fragments.

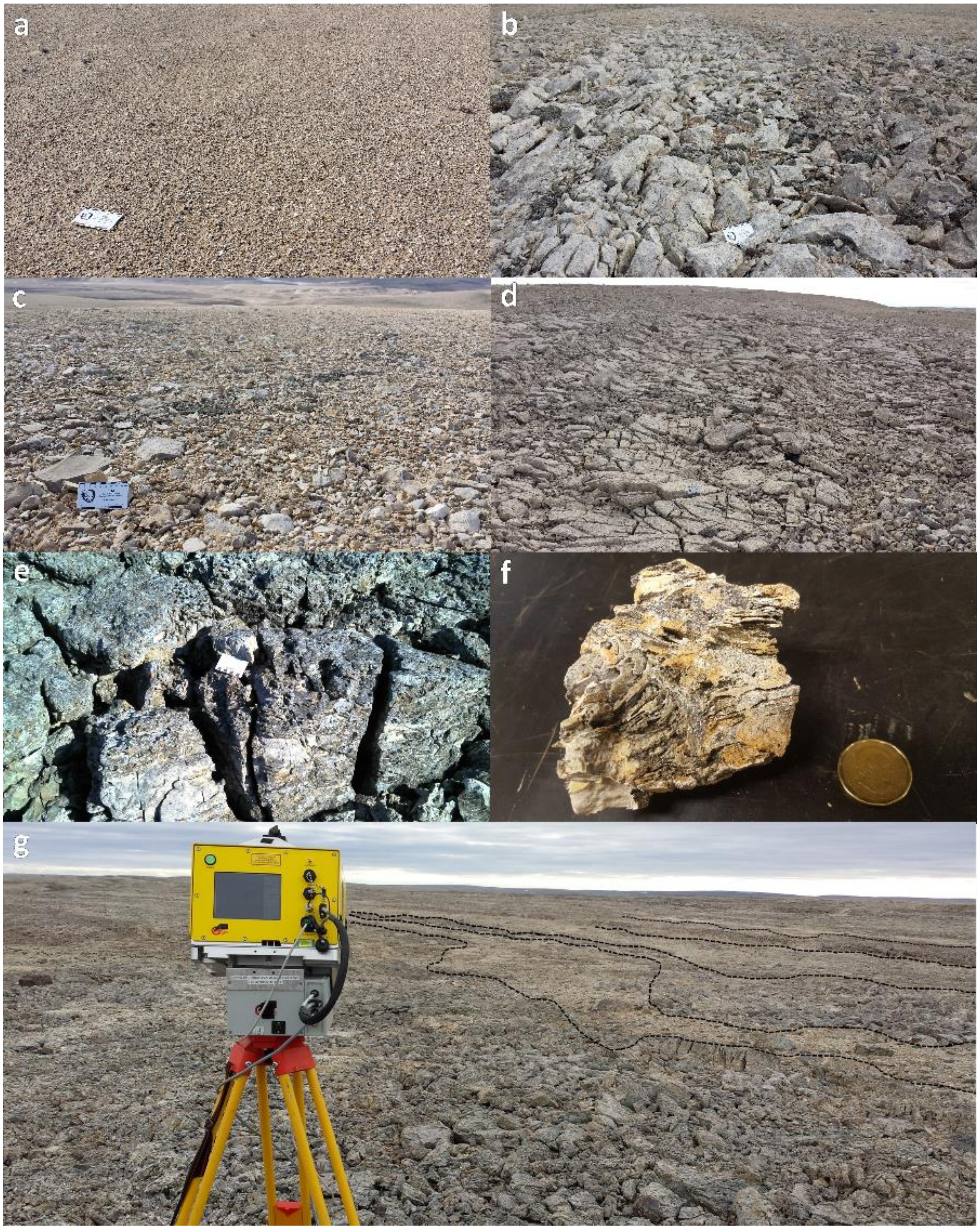

Figure 2.8. Field photos from each unit. (a) sandy glacial deposits of Unit 1, (b) weathered chert-bearing dolostones of Unit 2, (c) smoother surfaces covered by glacial deposits of Unit 2, (d) weathered dolostones of Unit 3, (e) silica-coated surfaces in Unit 4, (f) a sample of Unit 4, and (f) alternate layering of weathered carbonates and alluvial deposits in Unit 4 (dashed lines). A scale card of 9 by 5 cm (a-e), a ~2.5 cm diameter coin (f), and a tripod-mounted LiDAR of 1.6 m height (g) for scale.

2.6 Discussion and conclusions

We used several different remote sensing sensors to investigate the Tunnunik impact structure in terms of lithology, physical surface properties, and morphology for remote predictive mapping. Based on our remote predictive interpretations and field observations, we conclude:

1) ASTER TIR bands are the most effective to determine the main lithologies. The ASTER TIR MNF composite suggests that blue-green units are mainly comprised of carbonates, with the greener the colour of the unit, the more dolomite being present. The orange-magenta to red units indicate silica-bearing surfaces. The ASTER TIR band ratios are also effectively able to detect the high concentrations of carbonates and silica. Glacial deposits (Unit 1) and silica-coated carbonates (Unit 4), however, are not differentiated showing the similar spectra at the 5 TIR bands. For glacial deposits (Unit 1), the XRD analysis confirmed a substantial portion (even as the most major component) of dolomite from collected samples, but silica signatures are much more dominant from the ASTER TIR analysis, although it shows an absorption feature at the TIR band 14 relating to carbonates. This indicates that the actual mineral and lithological compositions can be different from the spectral signatures detected from the view of spectral remote sensors at a broad spatial resolution (e.g., 90 m for ASTER TIR). This is because spectral sensors are only able to detect the topmost layer (micrometers) of the rock surface, so surficial coatings can confound identification.

2) Landsat 8 provides supplemental spectral signatures to define different spectral units. Landsat 8 VNIR/SWIR band ratio analysis suggests that ferric (b4/b2) and ferrous (b6/b5)

iron signatures are related to surficial oxidization and staining of iron components by surface weathering. Carbonate signatures are represented by b6/b7 and are widespread over the Tunnunik structure.

However, even though Unit 3 shows the highest concentration of carbonate signatures from the ASTER TIR (Fig. 2.2a) and prominent presence of dolostone from the field observation and XRD analysis, carbonate signatures are poorly detected in Unit 3 and ferric and ferrous iron signatures are rather much more dominant. One possible explanation is the effect of particle size on spectral reflectance (Cooper and Mustard, 1999). Rough and blocky boulder surfaces of Unit 3 could significantly weaken the spectral reflectance of Landsat 8 SWIR bands 6 and 7 compared to the surrounding moderately rough surfaces of dolostone, chert, and fine-grained deposits (i.e., Unit 2).

3) RADARSAT-2 polarimetric decomposition analysis suggests that the Pauli decomposition best describes single-bounce scattering (blue) in very smooth glacial fluvial deposits, and double-bounce and multiple scattering (yellow) in carbonate rocks such as dolostone and limestones weathered to rough and blocky rock fragments. The multiple-diffused scattering component in the FD decomposition was modeled to describe forest canopy scatters by overemphasizing the cross-polarized HV scattering components (i.e., by 8 times the power of HV components (Freeman et al., 1998) versus by 2 times the power of HV components in the Pauli composite (Cloude and Pottier, 1996)). Thus, even a relatively small amount of cross-polarized scattering signatures from very rough and blocky surfaces can be translated similarly to forest canopies or dense vegetation in the FD decomposition. It is recommended that the Pauli decomposition is best to describe and visualize both double-bounce and multiple scattering components that can be generated

from highly weathered rough surfaces and blocky boulders in the Arctic, which are different to multiple-diffused scattering signatures in forest canopies. The *Hα* decomposition also confirms that they have entropy values greater than 0.5 and alpha angle values ranging 20° to 40°, particularly beyond the typical range of dense vegetation and forest between 40° and 50° (Cloude and Pottier, 1997).

4) High-resolution Quickbird imagery provides more detailed surface textural information. It is particularly useful to identify morphological features, such as gullies and thermal contraction polygons, that supports the presence of glacial alluvial deposits. Extensive glacial striations are observed in the deeply weathered rough surfaces revealed by RADARSAT-2. Topographic data is also useful in understanding the deposition processes by glacial activity in the Arctic and relate them to different landforms depending on elevation.

In summary, remote sensing-derived parameters such as band ratios and scattering mechanism components can be used to characterize different geological units. These can be incorporated into a decision-tree algorithm to automatically produce a remote predictive map. The decision-tree based remote predictive mapping algorithm used in this study delineated four different geological units (i.e. fluvio-lacustrine glacial deposits, chert-bearing dolostone, dolostone, and silica-coated dolostone) in the Tunnunik impact structure. Major lithologies were best defined by the ASTER TIR emissivity, however, a greater number of TIR bands or hyperspectral bands at higher resolution are recommended for more detailed and accurate lithological mapping in the future. Landsat 8 VNIR/SWIR reflectance effectively removed vegetated surfaces at the masking process and supported additional mineral signatures such as iron oxides. This study showed that SAR on its own is not sufficient for accurate geological mapping, but provided complementary surface roughness properties that was not possible with spectral classification alone.

Furthermore, the decision-tree algorithm can be further modified depending on user needs (i.e., what aspects need to be mapped by simplifying or subdividing the parameters applied). As more remote sensing data sets become available, a number of quantitative remote sensing parameters can be updated, contributing to more diverse and accurate mapping. Previous remote sensing mapping works have focused on improving classification accuracy by adding more remote sensing parameters and relying on statistical techniques (e.g., Harris et al., 2014; LaRocque et al., 2012), but more selective decision-tree mapping algorithms based on various geological perspectives and interpretation can provide a variety of thematic geological maps (e.g., highly-weathered carbonate rock concentration map).

2.7 References

Abrams, M., 2000. The Advanced Spaceborne Thermal Emission and Reflection Radiometer (ASTER): Data products for the high spatial resolution imager on NASA's Terra platform. Int. J. Remote Sens. 21, 847–859. doi:10.1080/014311600210326

Abrams, M., Hook, S., Ramachandran, B., 1995. ASTER user handbook. Jet Propulsion Laboratory, Pasadena, CA.

Bandis, S.C., Lumsden, A.C., Barton, N.R., 1983. Fundamentals of rock joint deformation. Int. J. Rock Mech. Min. Sci. Geomech. Abstr. 20, 249–268.

Christensen, P.R., Bandfield, J.L., Hamilton, V.E., Howard, D.A., Lane, M.D., Piatek, J.L., Ruff, S.W., Stefanov, W.L., 2000. A thermal emission spectral library of rock-forming minerals. J. Geophys. Res. 105, 9735–9739.

Clark, R.N., Gallagher, A.J., Swayze, G.A., 1990. Material absorption band depth mapping of imaging spectrometer data using the complete band shape least-squares algorithm simultaneously fit to multiple spectral features from multiple materials, in: The Third Airborne Visible/Infrared Imaging Spectrometer (AVIRIS) Workshop. pp. 176–186.

Clark, R.N., King, T.V. V, Klejwa, M., Swayze, G.A., 1990. High spectral resolution reflectance spectroscopy of minerals. J. Geophys. Res. Solid Earth 95, 12653–12680.

Cloude, S.R., Pottier, E., 1997. An entropy based classification scheme for land applications of polarimetric SAR. IEEE Trans. Geosci. Remote Sens. 35, 68–78.

Cloude, S.R., Pottier, E., 1996. A review of target decomposition theorems in radar polarimetry. IEEE Trans. Geosci. Remote Sens. 34, 498–518.

Cloutis, E.A., 1996. Hyperspectral geological remote sensing: evaluation of analytical techniques. Int. J. Remote Sens. 17, 2215–2242. doi:10.1080/01431169608948770

Cooper, B.L., Salisbury, J.W., Killen, R.M., Potter, A.E., 2002. Midinfrared spectral features of rocks and their powders. J. Geophys. Res. Planets 107, 1–17. doi:10.1029/2000JE001462

Cooper, C.D., Mustard, J.F., 1999. Effects of very fine particle size on reflectance spectra of smectite and palagonitic soil. Icarus 142, 557–570.

Dredge, L.A., 1992. Breakup of limestone bedrock by frost shattering and chemical weathering , eastern Canadian Arctic. Arct. Alp. Res. 24, 314–323.

Drury, S.A., 1993. Image interpretation in geology, 2nd ed. Chapman and Hall, London.

Freeman, A., Member, S., Durden, S.L., 1998. A three-component scattering model for polarimetric SAR data. IEEE Trans. Geosci. Remote Sens. 36, 963–973.

Friedl, M.A., Brodley, C.E., 1997. Decision tree classification of land cover from remotely sensed data. Remote Sens. Environ. 61, 399–409. doi:10.1016/S0034-4257(97)00049-7

Goetz, A.F., Rowan, L.C., 1981. Geologic remote sensing. Science (80-.). 211, 781–791. doi:10.1126/science.211.4484.781

Graham, D.F., Grant, D.R., 1991. A test of airborne, side-looking synthetic-aperture radar in central Newfoundland for geological reconnaissance. Can. J. Earth Sci. 28, 257–265.

Green, A.A., Berman, M., Switzer, P., Craig, M.D., 1988. Transformation for ordering multispectral data in terms of image quality with implicaitons for noise removal. IEEE Trans. Geosci. Remote Sens. 26, 65–74. doi:10.1109/36.3001

Grieve, R.A.F., 2012. Economic deposits at terrestrial impact structures, in: Osinski, G.R., Pierazzo, E. (Eds.), Impact Cratering: Processes and Products. Wiley-Blackwell, pp. 177–193.

Grunsky, E.C., 2002. The application of principal components analysis to multi-beam RADARSAT-1 satellite imagery: A tool for land cover and terrain mapping. Can. J. Remote Sens. 28, 758–769. doi:10.5589/m02-071

Harris, J.R., Grunsky, E.C., He, J., Gorodetzky, D., Brown, N., 2012. A robust, cross-validation classification method (RCM) for improved mapping accuracy and confidence metrics. Can. J. Remote Sens. 38, 69–90. doi:10.5589/m12-013

Harris, J.R., He, J.X., Rainbird, R., Behnia, P., 2014. A comparison of different remotely sensed data for classifying bedrock types in Canada’s Arctic: Application of the robust classification method and random forests. Geosci. Canada 41, 557. doi:10.12789/geocanj.2014.41.062

Harris, J.R., Rogge, D., Hitchcock, R., Ijewliw, O., Wright, D., 2005. Mapping lithology in Canada’s Arctic: application of hyperspectral data using the minimum noise fraction transformation and matched filtering. Can. J. Earth Sci. 42, 2173–2193. doi:10.1139/e05-064

Harris, J.R., Wickert, L., Lynds, T., Behnia, P., Rainbird, R., Grunsky, E., McGredor, R., Schetselaar, E., 2011. Remote Predictive Mapping 3. Optical remote sensing –A review for remote predictive geological mapping in northern Canada 38, 49–83.

Hudec, P.P., 1973. Weathering of rocks in Arctic and Sub-arctic environment, in: Proceedings of the Symposium on the Geology of the Canadian Arctic. pp. 313–335.

Hunt, G.R., 1977. Spectral signatures of particulate minerals in the visible and near infrared. Geophysics 42, 501–513.

Hunt, G.R., Salisbury, J.W., 1971. Visible and near infrared spectra of minerals and rocks. II. Carbonates. Mod. Geol. 2, 23–30.

Hunt, G.R., Salisbury, J.W., 1970. Visible and near-infrared spectra of minerals and rocks: I silicate minerals. Mod. Geol. 1, 283–300.

Iwasaki, A., Tonooka, H., 2005. Validation of a crosstalk correction algorithm for ASTER/SWIR. IEEE Trans. Geosci. Remote Sens. 43, 2747–2751. doi:10.1109/TGRS.2005.855066

Kruse, F.A., Lefkoff, A.B., Boardman, J.W., Heidebrecht, K.B., Shapiro, A.T., Barloon, P.J., Goetz, A.F.H., 1993. The spectral image processing system (SIPS)—interactive visualization and analysis of imaging spectrometer data. Remote Sens. Environ. 44, 145–163. doi:10.1016/0034-4257(93)90013-N

LaRocque, A., Leblon, B., Harris, J., Jefferson, C., Tschirhart, V., Shelat, Y., 2012. Surficial materials mapping in Nunavut, Canada with multibeam RADARSAT-2 dual-polarization C-HH and C-HV, LANDSAT-7 ETM+, and DEM data. Can. J. Remote Sens. 38, 281–305. doi:10.5589/m12-020

Lee, J.-S., Pottier, E., 2009. Polarimetric radar imaging: from basics to applications. CRC Press, New York.

McCarroll, D., Nesje, A., 1996. Rock surface roughness as an indicator of degree of rock surface weathering. Earth Surf. Process. Landforms 21, 963–977. doi:10.1002/(SICI)1096-9837(199610)21:10<963::AID-ESP643>3.0.CO;2-J

McHone, J.F., Greeley, R., Williams, K.K., Blumberg, D.G., Kuzmin, R.O., 2002. Space shuttle observations of terrestrial impact structures using SIR-C and X-SAR radars. Meteorit. Planet. Sci. 37, 407–420. doi:10.1111/j.1945-5100.2002.tb00824.x

Pavlic, G., Singhroy, V., Duk-Rodkin, A., Alasset, P.-J., 2008. Satellite data fusion techniques for terrain and surficial geological mapping, in: IEEE Geoscience and Remote Sensing Symposium. pp. 314–317. doi:10.1109/IGARSS.2008.4779346

Rockwell, B.W., Hofstra, A.H., 2008. Identification of quartz and carbonate minerals across northern Nevada using aster thermal infrared emissivity data-implications for geologic mapping and mineral resource investigations in well-studied and frontier areas. Geosphere 4, 218–246. doi:10.1130/GES00126.1

Rowan, L.C., Goetz, A.F.H., Ashley, R.P., 1977. Discrimination of hydrothermal altered and unaltered rocks in visible and near infrared multispectral images. Geophysics 42, 522–535. doi:10.1190/1.1440723

Rowan, L.C., Hook, S.J., Abrams, M.J., Mars, J.C., 2003. Mapping hydrothemally altered rocks at Cuprite, Nevada, using the Advanced Spaceborne Thermal Emission And Reflection Radiometer (ASTER), a new satellite-imaging system. Econ. Geol. 98, 1019–1027. doi:10.1016/S0361-1124(78)80358-X

Rowan, L.C., Mars, J.C., 2003. Lithologic mapping in the Mountain Pass, California area using Advanced Spaceborne Thermal Emission and Reflection Radiometer (ASTER) data. Remote Sens. Environ. 84, 350–366. doi:10.1016/S0034-4257(02)00127-X

Running, S.W., Way, J.B., McDonald, K.C., Kimball, J.S., Frolking, S., Keyser, A.R., Zimmerman, R., 1999. Radar remote sensing proposed for monitoring freeze-thaw transitions in boreal regions. Eos (Washington. DC). 80, 213–221. doi:10.1029/99EO00158

Sabins, F.F., 1999. Remote sensing for mineral exploration. Ore Geol. Rev. 14, 157–183. doi:10.1016/S0169-1368(99)00007-4

Sabins, F.F., 1987. Remote sensing: Principals and interpretation, 2nd ed. Freeman, New York.

Saint-Jean, R., Singhroy, V., Rheault, M., 1999. Multi-polarized airborne C-SAR images for geological mapping at lac volant, Québec, in: 13th Applied Geological Remote Sensing Workshop.

Salisbury, J.W., D'Aria, D.M., 1992. Emissivity of terrestrial materials in the 8-14 μm atmospheric window. Remote Sens. Environ. 42, 83–106. doi:10.1016/0034-4257(94)90102-3

Shelat, Y., Leblon, B., LaRocque, A., Harris, J., Jefferson, C.W., Lentz, D., Tschirhart, V., 2012a. Effects of incidence angles and image combinations on mapping accuracy of surficial materials in the Umiujalik Lake area, Nunavut using RADARSAT-2 polarimetric SAR, LANDSAT-7 ETM+ and DEM data. Part 1. Non-Polarimetric Analysis. Can. J. Remote Sens. 38, 383–403.

Shelat, Y., Lentz, D., Leblon, B., LaRocque, A., Harris, J., Jefferson, C., Tschirhart, V., 2012b. Effects of incidence angles on mapping accuracy of surficial materials in the Umiujalik Lake area, Nunavut, using RADARSAT-2 polarimetric SAR images. Part 2. Polarimetric analysis. Can. J. Remote Sens. 38, 404–423. doi:10.5589/m12-031

Singhroy, V., Kenny, F.M., Barnett, P.J., 1992. Radar imagery for quaternary geological mapping in glaciated terrains. Can. J. Remote Sens. 18, 117–123.

Smith, S.K., Grieve, R.A.F., Harris, J.R., Singhroy, V., 1999. The utilization of RADARSAT-1 imagery for the characterization of terrestrial impact landforms. Can. J. Remote Sens. 25, 218–228. doi:10.1080/07038992.1999.10874721

Strahler, A.H., 1980. The use of prior probabilities in maximum likelihood classification of remotely sensed data. Remote Sens. Environ. 10, 135–163. doi:10.1016/0034-4257(80)90011-5

Swain, P.H., Hauska, H., 1977. The decision tree classifier: Design and potential. IEEE Trans. Geosci. Electron. 15, 142–147. doi:10.1109/TGE.1977.6498972

Thompson, A.A., McLeod, I.H., 2004. The RADARSAT-2 SAR processor. Can. J. Remote Sens. 30, 336–344. doi:10.5589/m04-016

Tornabene, L.L., Moersch, J.E., Osinski, G.R., Lee, P., Wright, S.P., 2005. Spaceborne visible and thermal infrared lithologic mapping of impact-exposed subsurface lithologies at the Haughton impact structure, Devon Island, Canadian High Arctic: Applications to Mars. Meteorit. Planet. Sci. 40, 1835–1858. doi:10.1111/j.1945-5100.2005.tb00149.x

Toutin, T., Cheng, P., 2002. QuickBird – A milestone for high resolution mapping. Earth Obs. Mag. 11, 14–18.

Tucker, C.J., 1979. Red and photographic infrared linear combinations for monitoring vegetation. Remote Sens. Environ. 8, 127–150. doi:10.1016/0034-4257(79)90013-0

U. S. Geological Survey, 2016. Landsat 8 (L8) Data Users Handbook. doi:http://www.webcitation.org/6mu9r7riR

Ulaby, F.T., Moore, R.K., Fung, A.K., 1982. Microwave remote sensing : active and passive. Artech House, Norwood, MA.

van Der Meer, F.D., van Der Werff, H.M.A., van Ruitenbeek, F.J.A., Hecker, C.A., Bakker, W.H., Noomen, M.F., van Der Meijde, M., John, E., Carranza, M., Boudewijn De Smeth, J., Woldai, T., 2012. Multi- and hyperspectral geologic remote sensing: A review. Int. J. Appl. Earth Obs. Geoinf. 14, 112–128. doi:10.1016/j.jag.2011.08.002

Chapter 3

3 A modified semi-empirical radar scattering model for weathered rock surfaces*

Byung-Hun Choe, Gordon R. Osinski, Catherine D. Neish, and Livio L. Tornabene

3.1 Introduction

Extensive glacial activity and recurrent freeze-thaw processes alter surfaces and landforms in the Canadian Arctic (Lidmar-Bergström, 1997). Glacial erosion and deposition (e.g., glacial polish and striations, tills, drumlins, erratics) (Price and Clayton, 1973) and different lithology-dependent weathering processes (e.g., thinly laminated shales and siltstones weathering to fine-grained deposits versus massive dolomites and limestones weathering to lithic fragments and blocky boulder fields) form different physical surface properties (Hudec, 1973; Dredge, 1992). Arctic surfaces are relatively undisturbed by vegetation, and so their different polarimetric synthetic aperture radar (SAR) scattering signatures can be effectively correlated with their surface roughness. This can contribute to more accurate remote predictive mapping for Arctic geology (Chapter 2). It was noted that spectrally distinct units in the Canadian Arctic show different scattering mechanisms in polarimetric SAR decomposition analyses, indicating different surface roughness

---

* This chapter article is currently in preparation to be submitted to *IEEE Transactions on Geoscience and Remote Sensing* for publication with the same title.

properties depending on their lithologies (Chapter 2). In this study, we extend this work to quantitatively estimate the surface roughness and soil moisture content of geological units in the Canadian Arctic using polarimetric SAR data and radar scattering model inversion.

There has been extensive work on the use of radar scattering models to estimate the surface parameters of bare soil surfaces (Baghdadi et al., 2016; Dubois and Engman, 1995; Fung et al., 1992; Hajnsek et al., 2003; Moghaddam et al., 2000; Oh et al., 1992; Shi et al., 1997; Ulaby et al., 1982). The early conventional Kirchhoff approximation (KA) and small perturbation model (SPM) are only applicable to a very limited range of surfaces (i.e., surfaces with a radius of curvature larger than the radar wavelength (KA) or smooth surfaces relative to the radar wavelength (SPM)) (Ulaby et al., 1982). The integral equation method (IEM) (Fung et al., 1992), Oh (Oh et al., 1992), and extended-Bragg (Hajnsek et al., 2003) models have been developed to extend the valid range of estimating surface parameters and are now widely used for a variety of applications (e.g., agricultural fields, watersheds, wetlands, snow, sea ice) (Baghdadi and Zribi, 2006; Barrett et al., 2009; Bindlish and Barros, 2000; Hajnsek et al., 2009; Kim et al., 2011, 2012; Park et al., 2009; Schuler et al., 2002; Shi and Dozier, 2000; Tjuatja et al., 1992). The IEM is a physically-based model used to estimate radar backscattering coefficients from randomly rough dielectric surfaces according to surface parameters (i.e., RMS height, correlation length, dielectric constant) and radar sensor parameters (i.e., radar frequency, polarization, incidence angle) with a wider range of validity by applying approximate integral equations (Fung et al., 1992, see Appendix C for details), and bridges the gap between the KA and SPM by adopting a transition function for the Fresnel reflection coefficients used in the model (Fung and Chen, 2004; Wu et al., 2001). The extended-Bragg is also a theoretical model to extend the range of the SPM by describing roughness-induced disturbance through rotational transformation of the Bragg scattering matrix with a width of distribution of azimuthally oriented angles (β_1, β_1=0 for Bragg surfaces) (Hajnsek et al., 2003, see Appendix D for details). The extended-Bragg model estimates surface roughness (i.e., RMS height) and dielectric constants using polarimetric parameters (i.e., entropy (H), alpha angle (α), anisotropy (A)) derived from eigenvalues and eigenvectors of the rotated coherency matrix (Hajnsek et al., 2003). However, the IEM is still limited to bare soil surfaces of ks <3 (where k is the radar wavenumber ($=2\pi/\lambda$) and s is the RMS height) and requires at least three multiple acquisitions at different frequencies to invert the three unknown parameters (i.e., RMS height, correlation length, and dielectric constant) from the radar backscattering coefficients using the IEM formula (Fung et al., 1992). The extended-Bragg is validated in ks <1 and not applicable to rough surfaces with H >0.5 or α >25° (Hajnsek et al., 2003).

The Oh model is a semi-empirical model developed to determine the best fit between polarimetric parameters (i.e., cross-polarization backscattering coefficient, co-polarization ratio, cross-polarization ratio) and surface parameters (i.e., RMS height, volumetric soil moisture). It is based on extensive experimental measurements of multifrequency and multiangular polarimetric radar backscattering responses over bare soils with a variety of surface roughness and moisture conditions (Oh, 2004; Oh et al., 2002, 1992). It covers a much wider range (i.e., 0.13< ks <6.98 and 0.04< M_v <0.29, where k=wavenumber, s=RMS height, and M_v=volumetric soil moisture (cm^3/cm^3)) compared to the IEM and the extended-Bragg models (Oh, 2004). In particular, it has the great advantage that it can be readily modified for new surfaces by determining the best fit based on new experimental measurements, producing different model coefficients representative of that surface (Oh et al., 2002).

In this chapter, we estimate the surface roughness and volumetric soil moisture of different geological units in the Canadian Arctic by applying the Oh model to radar observations of different field sites. We then discuss the limitations of the Oh model for rough surfaces of weathered rocks (which are distinct from bare soil surfaces) by comparing the inversion results to our in-situ measurements of surface roughness and soil moisture. Finally, a modified semi-empirical model for weathered rough rock surfaces (ks > 3) is proposed, and validated with the in-situ measurements.

3.2 Polarimetric SAR data and ground truth collection

RADARSAT-2 (C-band, 5.405 GHz) quad polarimetric (i.e., HH, HV, VH, and VV) data were acquired over the Tunnunik and Haughton impact structures (detailed in Table 1). They were acquired at the Wide Fine Quad-pol beam mode (i.e., at 4.7 m by 5.1 m pixel spacing in slant range and azimuth with a wide swath of 50 km by 25 km in ground range and azimuth), and processed to single look complex (SLC) products with the Constant-Sigma lookup table (Thompson and McLeod, 2004). The SLC products were radiometrically calibrated into the sigma naught (σ_0) backscattering coefficients, then terrain corrected (at 20 m by 20 m pixel spacing) and filtered for speckle noise (Lee filter, 5 by 5 window) in that order. The data were processed using the Sentinel-1 Toolbox software (see https://sentinel.esa.int/web/sentinel/toolboxes/sentinel-1/tutorials).

Table 3.1. Specifications of RADARSAT-2 data used in Chapter 3

	Acquisition date	Pass	Beam mode	Incidence angle
Tunnunik	2015. 07. 11	descending	FQ7W	24.9~28.3°
Haughton	2016. 08. 08	ascending	FQ19W	37.7~40.4°

Fieldwork was conducted at the Tunnunik structure in July 13-August 20, 2015, and at the Haughton structure in July 29-August 4, 2016. We acquired high-resolution surface topography in 3-dimensional point clouds using a tripod-mounted LiDAR scanner (ILRIS-3D from Optech) (Figs. 3.1a and 3.1b). The scans were acquired at 2 mm horizontal spacing (X, Y) and 1 mm vertical spacing (Z) for regions roughly 5 m by 10 m in area. Volumetric soil moisture was measured using a portable soil moisture sensor with a handheld data logger (GS1 sensor from Decagon Devices; needle length: 5.2 cm, volume of influence: 1430 ml) (Figs. 3.1c and 3.1d). A total of 27 LiDAR scans were collected from the Tunnunik (11) and Haughton Haughton (16) impact structures. One-dimensional surface profiles with a length of 3 to 4 m were generated from the LiDAR scans. 10 selective profiles from each LiDAR scan, which are not affected by shadow and surface slope, were used to calculate surface roughness parameters (i.e., root mean square (RMS) height and correlation length) (Fig. 3.2), which were then averaged. The averaged surface roughness parameters are assumed to be able to represent the surface roughness for each site as each scan was acquired from a surface that looks alike at a broader coverage and represents a geological unit, though the area of each scan is less than a single ground pixel (i.e., 20 m by 20 m) of the processed RADARSAT-2 data.

The RMS height (s) is the standard deviation of surface height values (i.e., vertical variation of a surface profile) given by

$$S = \sqrt{\frac{1}{N-1}\left(\sum_{i=1}^{n}(z(x_i) - \overline{z})^2\right)}$$

(3.1)

where N is the number of samples, $z(x_i)$ is the surface height at each point x_i, and is the average surface height (Ulaby et al., 1982). The correlation length is determined by the lag distance where the autocorrelation function (ACF) value of the 1-dimensional surface profile equals to 1/e (i.e., horizontal variation of a surface profile). The ACF ($\rho(\tau)$) is given by

$$\rho(\tau) = \frac{\int z(x)z(x+\tau)dx}{\int z(x)^2 dx}$$

(3.2)

where $z(x)$ is the surface height at each point x and τ is the lag distance (Ulaby et al., 1982).

Soil moisture measurements were collected from fine-grained deposits, unsorted soil deposits with coarser boulders interspersed, or soil patches in and around weathered rock surfaces, at a total of 20 sites in the Tunnunik structure by averaging 15-20 measurements at each site. The soil moisture measurements collected from the Haughton structure were not used in this study because most of surfaces were highly saturated with over 20% moisture content due to rainy and cloudy weather during the fieldwork.

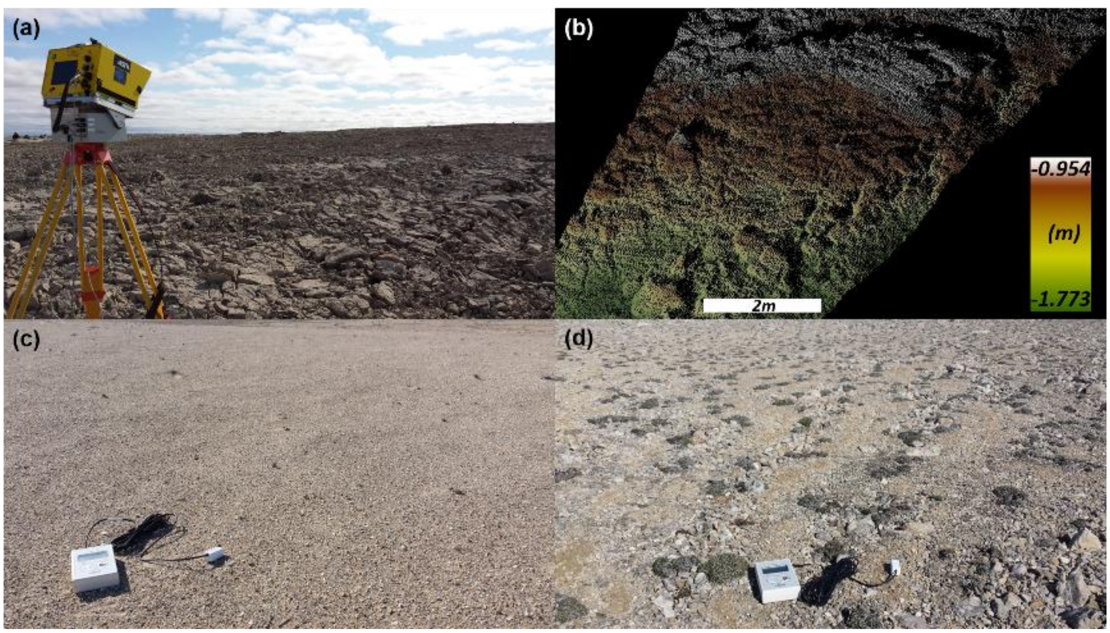

Figure 3.1. Example of in situ measurements of surface roughness and soil moisture. (a) LiDAR scanning weathered rock surfaces at the Tunnunik (~1.7 m tripod-mounted LiDAR for scale). (b) Surface topography in a 3-D point clouds generated from the LiDAR scan. (c) Soil moisture measurement from fine-grained deposits (~9 cm by 15 cm handheld data logger for scale). (d) Soil moisture measurement from unsorted soil deposits with coarser boulders interspersed.

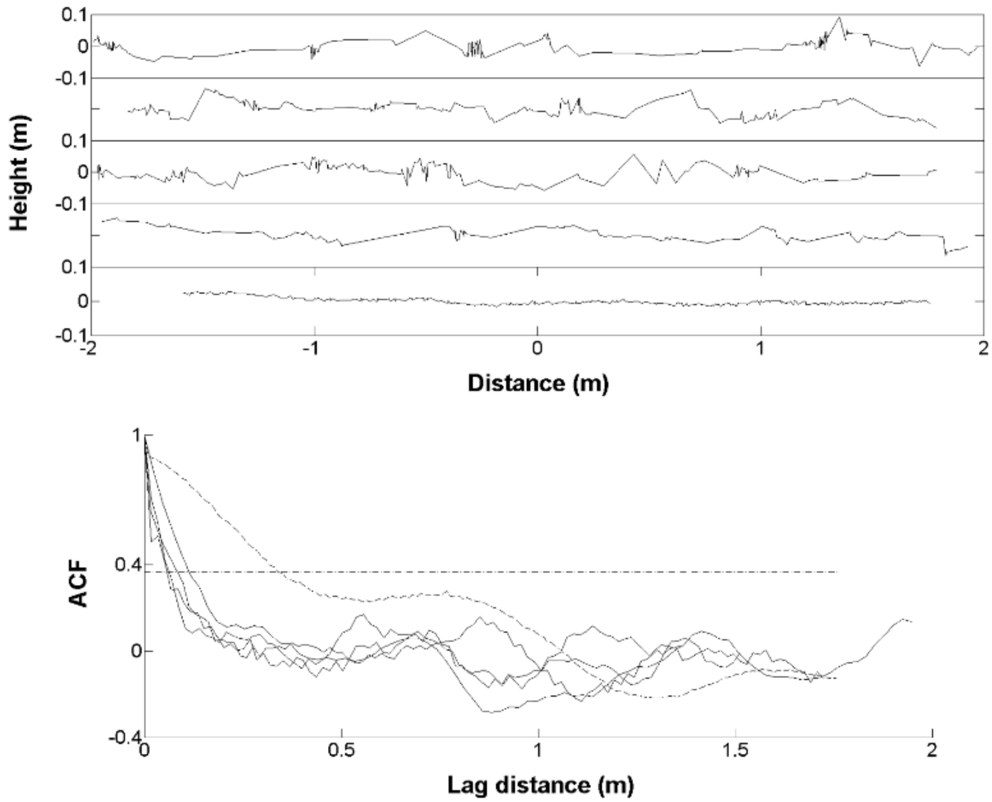

Figure 3.2. Weathered rock surface profiles (upper; top 4=weathered rocks, bottom= fine-grained deposits for comparison) and their autocorrelation function (ACF) plots (bottom; solid lines=weathered rocks surfaces, dashed line=fine-grained deposits). The parallel dash-dot line represents where ACF equals to 1/e.

3.3 Oh model (2004)

3.3.1 Inversion method

The semi-empirical Oh model is given by three numerical formulas for the cross-polarization backscattering coefficient (σ_{vh}^{0}), the co-polarization ratio ($\sigma_{hh}^{0}/\sigma_{vv}^{0}$), and the cross-polarization ratio ($\sigma_{vh}^{0}/\sigma_{vv}^{0}$) (Oh, 2004). These formulas relate to incidence angle (θ), wave number (k), surface roughness (i.e., RMS height, s) and volumetric soil moisture (M_v) as follows:

$$\sigma_{vh}^{0} = 0.11Mv^{0.7}(cos\theta)^{2.2}\{1 - exp[-0.32(ks)^{1.8}]\}$$

(3.3)

$$\frac{\sigma_{hh}^{0}}{\sigma_{vv}^{0}} = 1 - (\frac{\theta}{90°})^{0.35Mv^{-0.65}} \cdot exp[-0.4(ks)^{1.4}]$$

(3.4)

$$\frac{\sigma_{vh}^{0}}{\sigma_{vv}^{0}} = 0.095(0.13 + sin1.5\theta)^{1.4}\{1 - exp[-1.3(ks)^{0.9}]\}$$

(3.5)

The inversion process to obtain the RMS height (*s*) and volumetric soil moisture (M_v) using (3)-(5) is as follows (see Oh (2004) for details): Firstly, solve (3.3) for *ks* and substitute the equation into (3.4). The co-polarization ratio ($\sigma_{hh}^{0}/\sigma_{vv}^{0}$) is a function of θ, M_v, and σ_{vh}^{0}, $F(\theta, M_v, \sigma_{vh}^{0})$, so M_v is now the only unknown parameter in (3.4) and can be solved by finding the root numerically or using a lookup table. Subsequently, *ks* is obtained by inserting M_v into the equation solved for *ks* from (3.3). Alternatively, *ks* can be directly obtained from (3.5) where *ks* is the only unknown parameter, and M_v can then be obtained by inserting the derived *ks* into (3.3) and (3.4), respectively. A total of two *ks* and three M_v values are obtained through this process and averaged for more reliable and accurate inversion.

3.3.2 Inversion results

Both surface roughness (ks) and volumetric soil moisture (M_v) measurements were successfully collected at the Tunnunik impact structure. We applied equations (3.3)-(3.5) of the Oh model to the SAR data, and compared the inversion results to the in-situ measurements. The estimated ks values agree well with the in-situ measurements for relatively smooth surfaces ($ks \leq 3$), but they are highly saturated for $ks > 3$ and underestimate the values for rough surfaces consisting of weathered rocks (Fig. 3.3a). On the other hand, the volumetric soil moisture inversion shows a better agreement with the in-situ measurements collected from fine-grained deposits and unsorted soil deposits with coarser boulders interspersed (Fig. 3.3b).

However, the moisture contents of weathered rock surfaces with small patches of soil deposits in/around them are generally estimated at > 20%, even though most or all of their surfaces are composed of dry, rough rocks (see, for example, Figure 3.1a). We propose that the anomalously high moisture values result from an as yet uncharacterized surface roughness effect, not the actual moisture content of these very small soil patches. The Oh model simulation shows that the cross-polarization backscattering coefficient (σ_{vh}^{0}) is rapidly saturated after $ks > 3$. For the cross-polarization backscattering coefficients observed for weathered rock surfaces (> -17 dB), values of M_v are in excess of 20%, and remain constant even as ks increases (Fig. 3.4a). The co-polarization ratio ($\sigma_{hh}^{0}/\sigma_{vv}^{0}$) also rapidly increases with increasing ks and approaches 0 dB (i.e., σ_{hh}^{0}=σ_{vv}^{0}) at $ks > 3$ with no dependence on M_v (Fig. 3.4b). Accordingly, the inversion process is largely affected by ks for rough surfaces. The inversion results show that the Oh model is well applied for smooth surfaces of fine-grained and unsorted glacial deposits, but not applicable for dry and rough weathered rock surfaces.

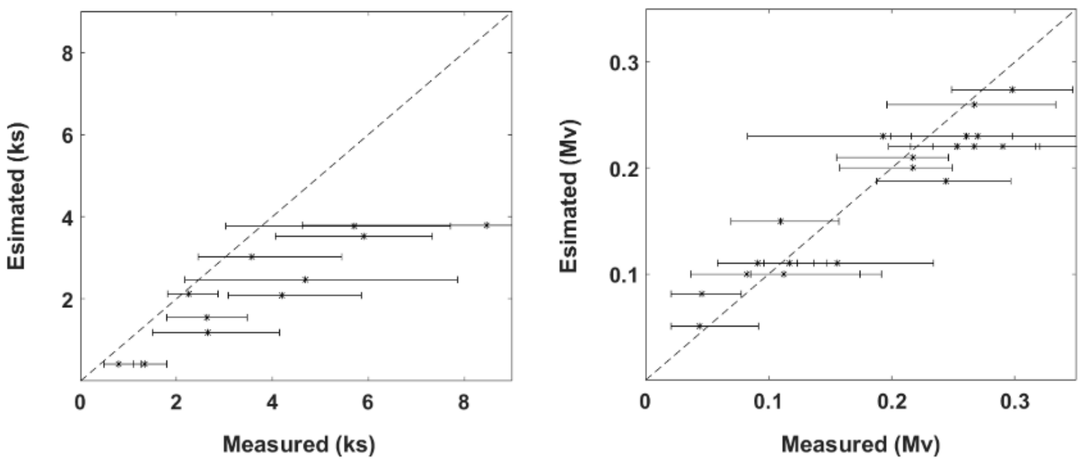

Figure 3.3. Comparison between Oh model inversion results and in situ measurements from the Tunnunik impact structure. (a) Surface roughness (*ks*). (b) Volumetric soil moisture (M_v). The asterisks and horizontal error bars represent the average and the range of each measurement, respectively.

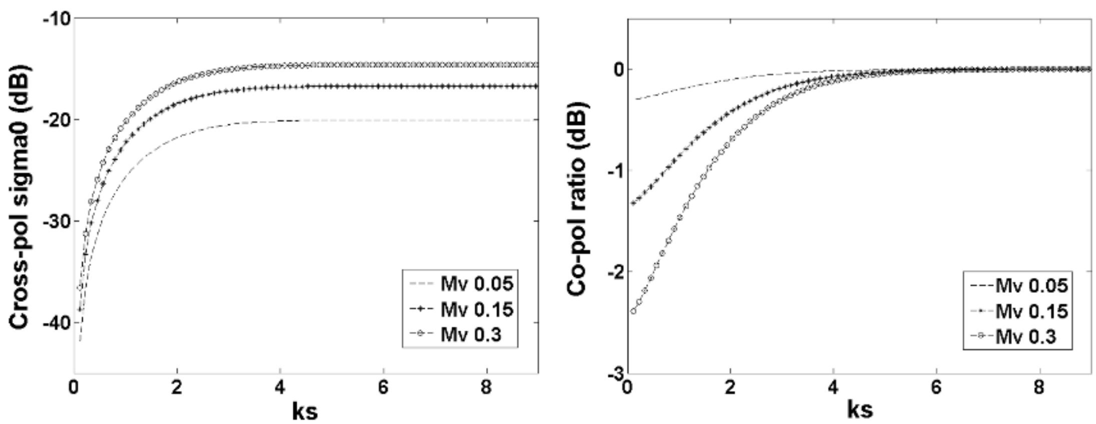

Figure 3.4. Oh model simulation according to surface roughness (*ks*: 0~9) and volumetric soil moisture (M_v: 0.05 (dash), 0.15 (asterisk), 0.3 (circle)) at θ=30°. (a) The cross-polarization backscattering coefficient ($\boldsymbol{\sigma^0_{vh}}$). (b) The co-polarization ratio ($\boldsymbol{\sigma^0_{hh}/\sigma^0_{vv}}$).

3.4 Modified model for weathered rock surfaces

3.4.1 Model modification

Unlike soil deposits, which are capable of retaining moisture, weathered rock surfaces drain water rapidly and generally have dry conditions except for a few hours after a rain storm. Radar backscattering is more affected by surface roughness than soil moisture content (or dielectric properties) (Fung, 1994; Ulaby et al., 1982). Thus, we assume that radar backscattering from weathered rock surfaces in these regions is mainly controlled by surface roughness. Also, radar backscattering from very rough surfaces of *ks* > 3 is less affected by different incidence angles (Oh et al., 1992). We developed a modified model for weathered rock surfaces based on a numerical formula for the cross-polarization ratio

(3.5) with dependence on only surface roughness, not soil moisture content, unlike (3.3) and (3.4). The original functional form of (3.5) is given by

$$\frac{\sigma_{vh}^{0}}{\sigma_{vv}^{0}} = \boldsymbol{a}(s/l + sin\boldsymbol{b}\theta)^{\boldsymbol{c}}\{1 - exp[-\boldsymbol{d}(ks)^{\boldsymbol{e}}]\} \tag{3.6}$$

where *s/l* is the surface slope determined by the RMS height (*s*) and the correlation length (*l*), and *a*, *b*, *c*, *d*, and *e* are coefficients determined by fits to the data (Oh et al., 2002). The surface slope (*s/l*) was derived from the RMS heights and correlation lengths measured from surface profiles collected in the field. The average surface slope for weathered rock surfaces of the Tunnunik and Haughton structures was 0.35, which is about three times larger than the surface slope for bare soil surfaces (0.13) used in (Oh, 2004). This function was then fit to the RADARSAT-2 polarimetric SAR data using the measured *ks* values, utilizing a least squares curve fitting approach (Figure 3.5). The derived coefficients are as follows; *a*=0.2, *b*=1.5, *c*=1.5, *d*=0.06, and *e*=2.2. A newly modified model for weathered rock surfaces in the Canadian Arctic is thus given by

$$\frac{\sigma_{vh}^{0}}{\sigma_{vv}^{0}} = 0.2(0.35 + sin1.5\theta)^{1.5}\{1 - exp[-0.06(ks)^{2.2}]\} \tag{3.7}$$

The modified model mitigates the rapid saturation of the Oh model at *ks* > 3 and can be successfully applied to very rough rock surfaces, up to approximately *ks ~9.*

3.4.2 Combined inversion algorithm

The Tunnunik and Haughton structures have a variety of geological units from fine-grained deposits to rough, weathered rock surfaces. Thus, to estimate surface roughness and volumetric soil moisture content, we must select the appropriate model (the Oh model or the modified model) depending on the surface roughness of the unit in question (Appendix F). Here, the cross-polarization ratio is first calculated by the Oh model (3.3) to determine whether it is composed of relatively smooth soil deposits ($ks \leq 3$). For example, for ks=3 at an incidence angle of 30°, the cross-polarization ratio is about –11.4 dB for the Oh model. Thus, the surface roughness of areas with cross-polarization ratios less than -11.4 dB will be estimated by the Oh model; the surface roughness of areas with higher cross-polarization ratios will be estimated by the modified model. For smooth surfaces with $ks \leq 3$, ks and M_v are estimated by the inversion of (3.3) to (3.5). For rough surfaces with $ks > 3$, only ks is estimated using (3.7); they are assumed to be weathered rock surfaces with very dry conditions (M_v=0).

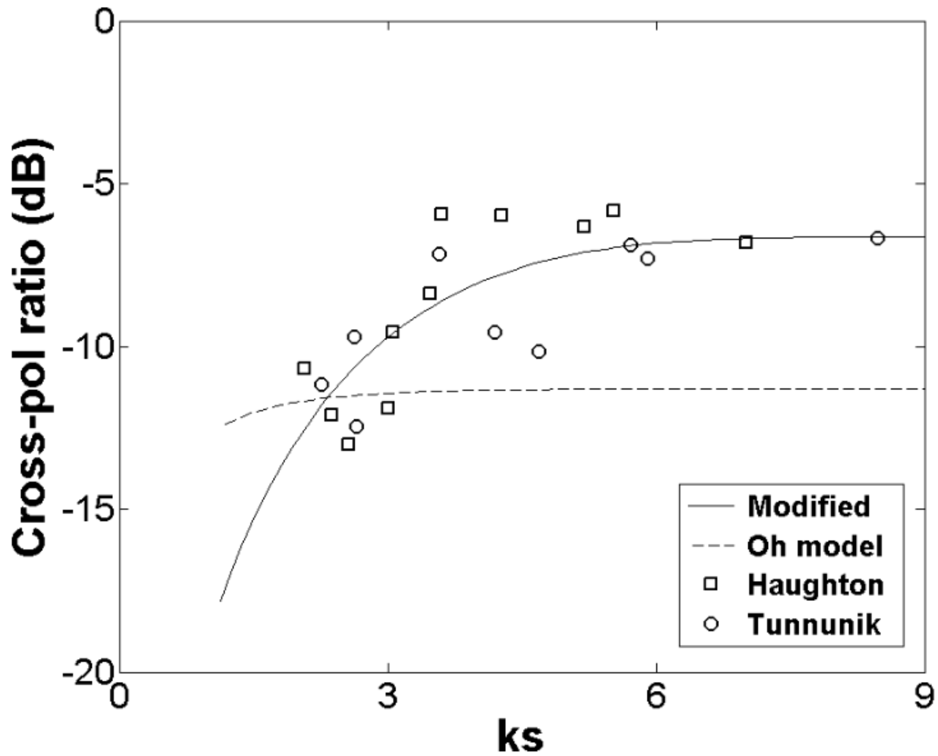

Figure 3.5. Modified model curve fit (solid line) to in situ measurements from weathered rock surfaces in the Tunnunik (circles) and Haughton (squares) structures. The original Oh model (dashed line) is shown for comparison.

3.4.3 Inversion results

Surface roughness (*ks*) and volumetric soil moisture (M_v) maps of the Tunnunik and Haughton structures were produced by applying the combined inversion algorithm (Fig. 3.6). In the Tunnunik surface roughness map (Fig. 3.6a), the upper areas north of the NE-SW trending fault crosscut the centre of the structure show smooth surfaces of $ks \leq 2$, where fine-grained deposits (T1; numbered 1 in the Tunnunik surface roughness map) are present (Chapter 2). Very rough surfaces of $ks > 5$ are observed in the eastern part of the structure, which are matched with dolomite (T3) and silica-coated dolomite (T4) units of the Victoria Island formation. The medium rough surfaces (*ks*: 2~5) between them are matched with chert-bearing dolomite units (T2) of the Victoria Island formation (see Chapter 2). The volumetric soil moisture map (Fig. 3.6b) derived for $ks \leq 3$ shows a variation in moisture contents between smooth and fine-grained deposits ranging from 0 to 35%. Most fine-grained deposits are unconsolidated and dry fast, and so have very low moisture contents; although high moisture over 20% are observed from deposits around channels and extensive developments of gullies are also present around them.

In the Haughton surface roughness map (Fig. 3.6c), the fine-grained deposits (H1), impact melt deposits (H2) that are widespread within the structure, and the Bay Fiord Formation (mainly comprised of dolomite and gypsum) along the eastern wall (H3) show smooth surfaces with $ks \leq 2$ (see Osinski et al. (2005) for details in geology of the Haughton structure). Medium rough surfaces (*ks*: 2~5) are observed in the Middle member of the Allen Bay Formation (dolomite) along the crater rim and to the west of the crater (H4). Very rough surfaces with $ks > 5$ are observed in the Eleanor River Formation (limestone and dolomite) exposed around the central uplift (H5), the Thumb Mountain Formation (limestone and dolomite) along the eastern wall (H6), the Lower member of the Allen Bay Formation (limestone) along the crater rim and to the east of the crater (H7), and fluvial deposits of boulders and cobbles within the structure (H8). These areas of high surface roughness are all observed to have been extensively weathered through a process known as cryoturbation, which breaks the more resistant limestone and dolomite rocks into highly angular clasts (see Figs. 2.8 and 4.7). High moisture contents are likewise observed around the channels, but the volumetric soil moisture map shows little variation compared to the

Tunnunik structure (Fig. 3.6d). It appears to have been affected by the rainy and cloudy weather near the acquisition date of the RADARSAT-2 data. The newly estimated roughness values for the weathered rock surfaces were compared to the surface roughness measured in situ at the Tunnunik and Haughton structures (Fig. 3.7). The modified model shows a better agreement between the values for weathered rock surfaces at $ks > 3$, where the Oh model significantly underestimates the roughness (Fig. 3.3a). Consequently, the modified model has broadened the range of validity up to ~9 in *ks*.

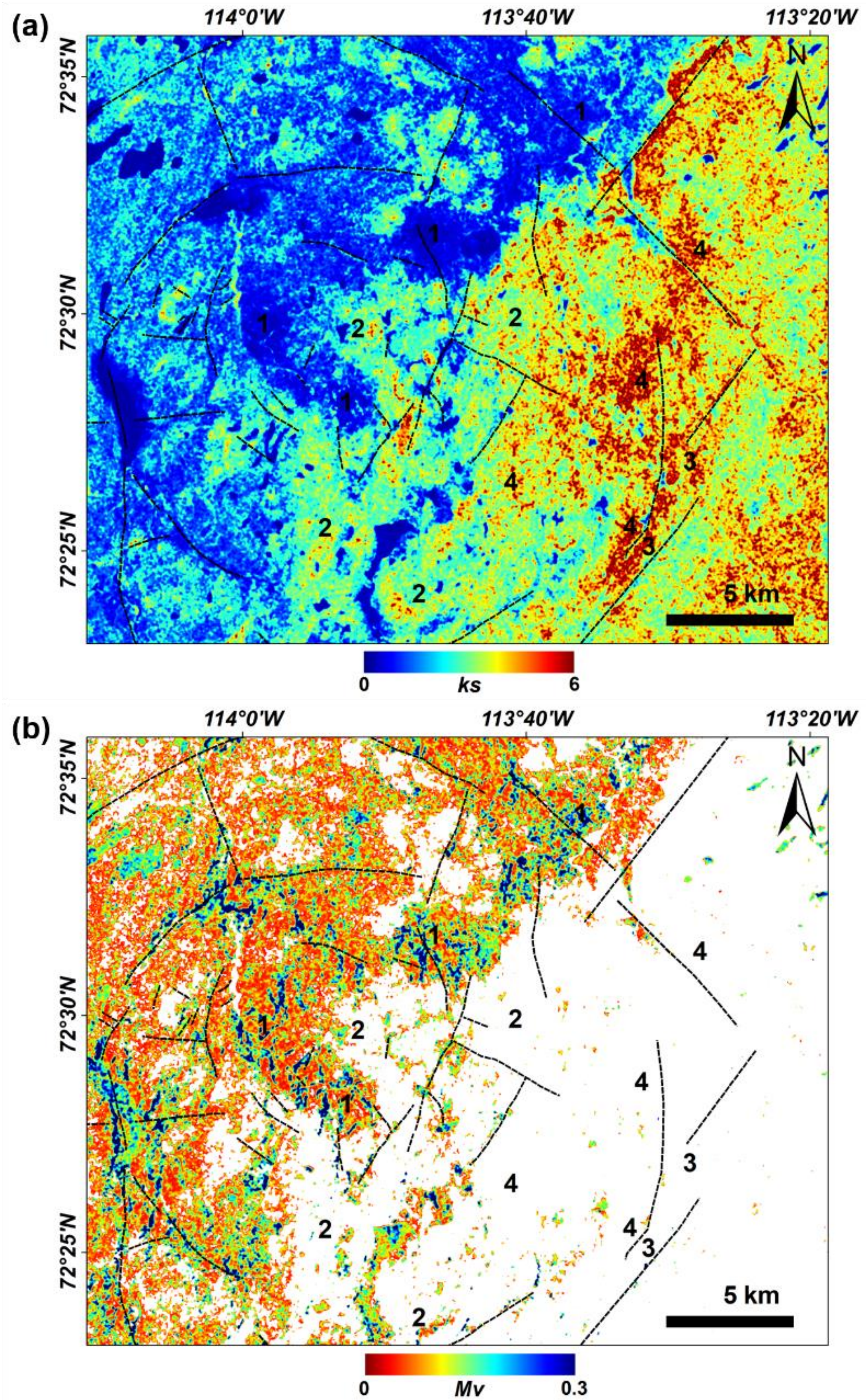
(a)
114°0'W
113°40'W
113°20'W
72°35'N
72°30'N
72°25'N
5 km
0
ks
6
(b)
114°0'W
113°40'W
113°20'W
72°35'N
72°30'N
72°25'N
5 km
0
Mv
0.3

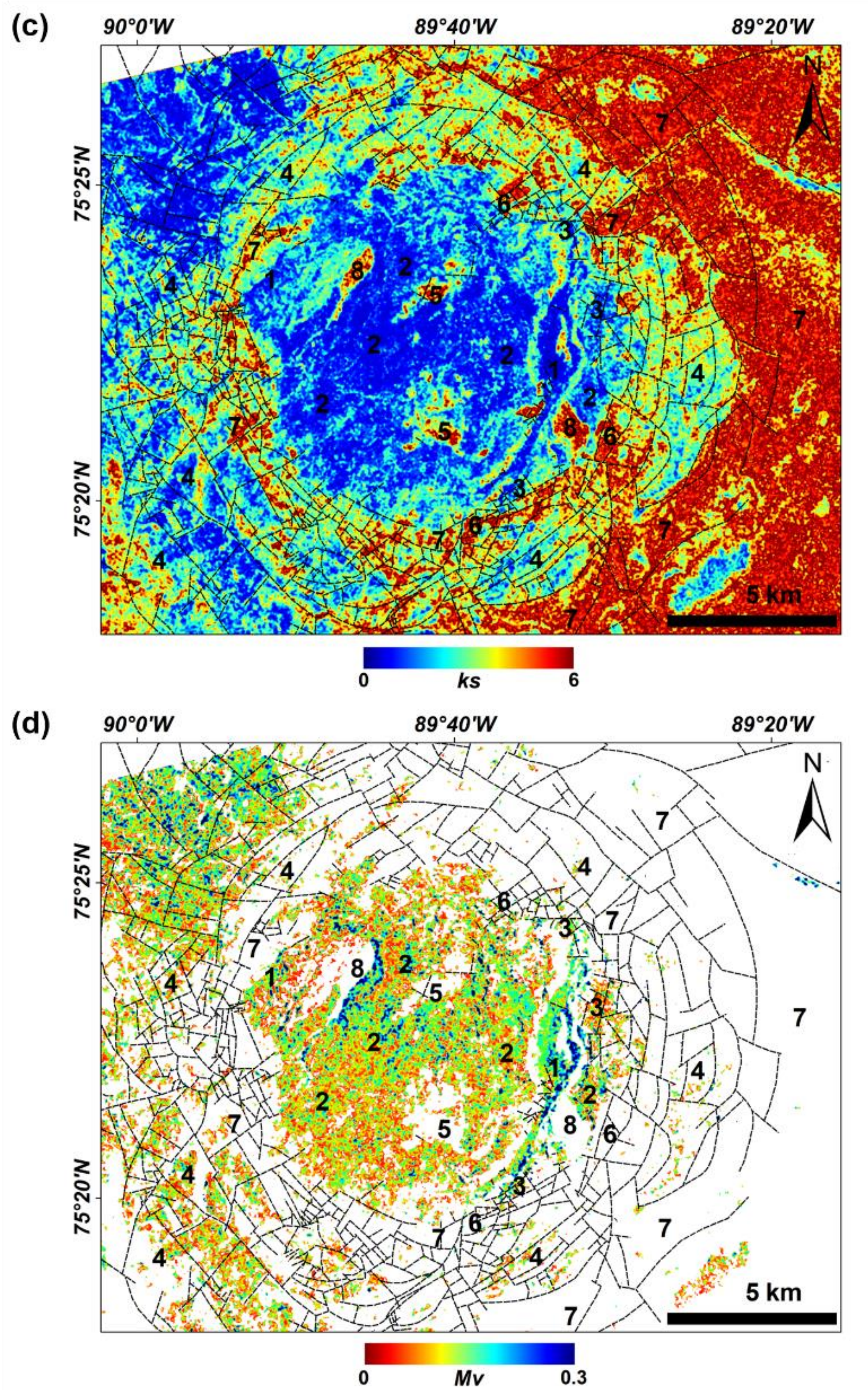
(c)
90°0'W
89°40'W
89°20'W
75°25'N
75°20'N
N
5 km
0
ks
6
(d)
90°0'W
89°40'W
89°20'W
75°25'N
75°20'N
N
5 km
0
Mv
0.3

(continued)

Figure 3.6. Inversion results obtained by applying the combined inversion algorithm. (a) Tunnunik surface roughness map (*ks*). See Figure 2.7 for comparison. (b) Tunnunik soil moisture map (M_v). (c) Haughton surface roughness map (*ks*). See Figure 1.6 for comparison. (d) Haughton soil moisture map (M_v). Weathered rock surfaces are masked out in white in the soil moisture maps. Black dashed lines are fault lines associated with the impact structures.

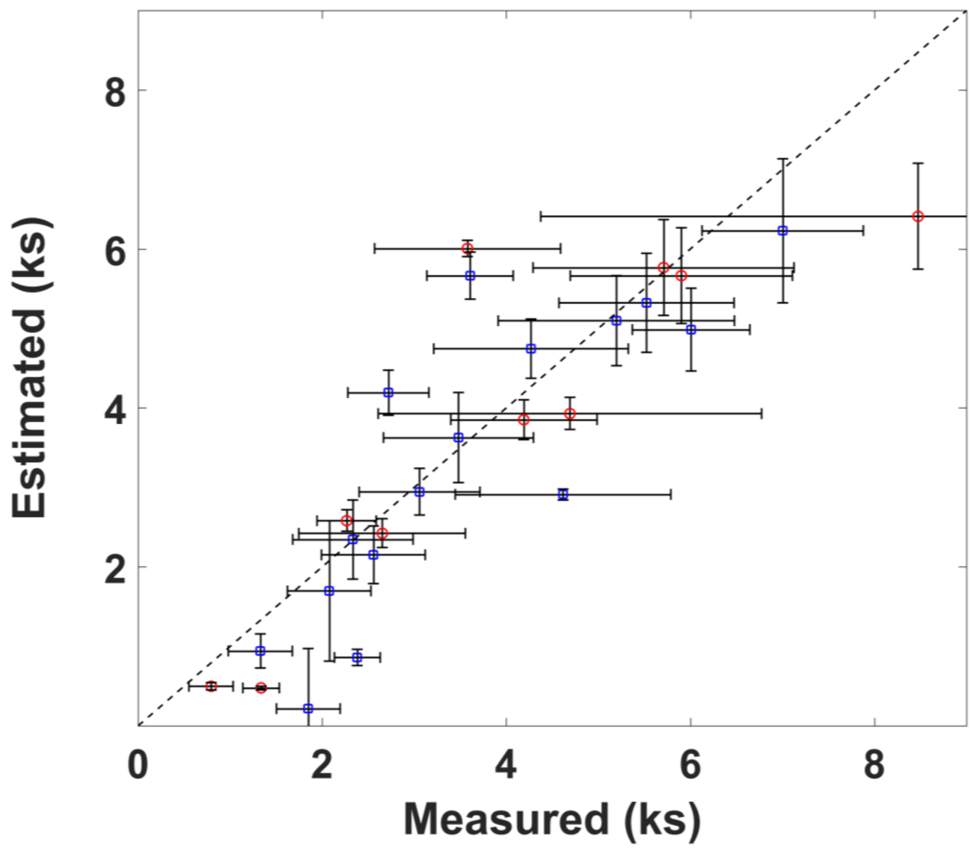

Figure 3.7. Comparison between the modified model inversion results and the surface roughness measurements from the Tunnunik (red circles) and Haughton (blue squares) impact structures. The markers represent the average and the horizontal and vertical error bars represent the standard deviations of each measurement and estimation, respectively.

3.5 Discussion and conclusions

Semi-empirical radar scattering models provide numerical functions that tie the radar cross-polarization coefficients, the co-polarization ratio, and the cross-polarization ratio to the surface roughness and soil moisture of target surfaces at a variety of incidence angles (Oh et al., 2002). In this work, we developed a new modified model that is valid over a wide range of surface roughnesses. If enough experimental measurements can be collected, this new model has the great potential to expand our understanding of the physical properties of surfaces that cover a wide range of roughness and soil moisture contents.

We validated this new scattering model using different geological units around the Tunnunik and Haughton impact structures in the Canadian Arctic. The modified model is based only on the relationship between the cross-polarization ratio ($\sigma_{vh}^0/\sigma_{vv}^0$) and surface roughness (i.e., RMS height) for very rough surfaces, and is insensitive to the moisture content. It was able to estimate the surface roughness of weathered rock surfaces up to *ks* ~9, an improvement over the original Oh model for bare soil surfaces.

In our work, we found that fine-grained glacial deposits ((e.g., T1, H1, H3) and crater-fill deposits (i.e., impact melt breccias, H2) have very smooth surfaces (*ks* ≤ 2), while resistant, thick-bedded and massive limestone and dolomite units (e.g. T3, T4, H5, H6, H7) are weathered to very rough surfaces (*ks* > 5). Weathered rock surfaces interspersed with glacial deposits (e.g., T2) and recessive thin bedded dolomite units (e.g., H4) are weathered to medium rough surfaces (*ks*: 2~5). These results suggest that the different surface roughness observed in different geological units is related to the form of weathering that is unique to that substrate. It appears to be particularly sensitive to the lithology and sedimentary structure (i.e., bedding) of the rock unit.

The soil moisture inversion for smooth and fine-grained deposits may not reflect the best estimates, due to the time difference between SAR data acquisitions and the in situ measurements. For the Tunnunik structure, the results showed a strong agreement between the estimated and measured soil moisture values (Fig. 3.3b), as there was little variation in weather conditions during the SAR acquisition and in situ measurements (specifically, clear and sunny days). However, the data for the Haughton structure was largely affected by rainy and cloudy weather during the in situ measurements, and so could not be validated. The results showed spatial variations in soil moisture contents with the highest values found along river valleys in the Tunnunik and Haughton structures, but in situ measurements within few hours on the same date of SAR acquisition need to be collected for further refinement and validation because moisture contents of top soils affecting to radar backscattering can be quickly changed within one day. Surface roughness, on the other hand, is not temporally affected by weather conditions and SAR acquisitions are little affected by incidence angles and dielectric properties for such dry and rough weathered rock surfaces, which facilitates developing a modified model. The model could be robustly validated at both sites. There was a range of surface roughness measured across the two sites, as described above.

In summary, the results of this study suggest that the polarimetric SAR-based inversion algorithm developed in this work for weathered rock surfaces can be used to quantify and monitor the surface properties and temporal changes of Arctic geological surfaces. Erosional and depositional processes can be monitored over time with broad spatial coverage and rapid accessibility. This is of particular importance as the North continues to warm as a result of global climate change.

3.6 References

Baghdadi, N., Choker, M., Zribi, M., Hajj, M., Paloscia, S., Verhoest, N., Lievens, H., Baup, F., Mattia, F., 2016. A new empirical model for radar scattering from bare soil surfaces. Remote Sens. 8, 920. doi:10.3390/rs8110920

Baghdadi, N., Zribi, M., 2006. Evaluation of radar backscatter models IEM, OH and Dubois using experimental observations. Int. J. Remote Sens. 27, 3831–3852. doi:10.1080/01431160600658123

Barrett, B.W., Dwyer, E., Whelan, P., 2009. Soil moisture retrieval from active spaceborne microwave observations: An evaluation of current techniques. Remote Sens. 1, 210–242. doi:10.3390/rs1030210

Bindlish, R., Barros, A.P., 2000. Multifrequency soil moisture inversion from SAR measurements with the use of IEM. Remote Sens. Environ. 71, 67–88. doi:10.1016/S0034-4257(99)00065-6

Dredge, L.A., 1992. Breakup of limestone bedrock by frost shattering and chemical weathering , eastern Canadian Arctic. Arct. Alp. Res. 24, 314–323.

Dubois, P.C., Engman, T., 1995. Measuring soil moisture with imaging radars. IEEE Trans. Geosci. Remote Sens. 33, 915–926. doi:10.1109/36.406677

Fung, A.K., 1994. Microwave scattering and emision. models and their applications. Artech House, Boston, MA.

Fung, A.K., Chen, K.S., 2004. An update on the IEM surface backscattering model. IEEE Geosci. Remote Sens. Lett. 1, 75–77. doi:10.1109/LGRS.2004.826564

Fung, A.K., Li, Z., Chen, K.S., 1992. Backscattering from a randomly rough dielectric surface. IEEE Trans. Geosci. Remote Sens. 30, 356–369. doi:10.1109/36.134085

Hajnsek, I., Cloude, S.R., Lek, J., Eric, P., 2003. Inversion of surface parameters from polarimetric SAR data 41, 1095–1097.

Hajnsek, I., Jagdhuber, T., Schön, H., Papathanassiou, K.P., 2009. Potential of estimating soil moisture under vegetation cover by means of PolSAR. IEEE Trans. Geosci. Remote Sens. 47, 442–454. doi:10.1109/TGRS.2008.2009642

Hudec, P.P., 1973. Weathering of rocks in Arctic and Sub-arctic environment, in: Proceedings of the Symposium on the Geology of the Canadian Arctic. pp. 313–335.

Kim, D., Moon, W.M., Kim, G., Park, S.-E., Lee, H., 2011. Submarine groundwater discharge in tidal flats revealed by space-borne synthetic aperture radar. Remote Sens. Environ. 115, 793–800. doi:10.1016/j.rse.2010.11.009

Kim, J., Kim, D., Hwang, B., 2012. Characterization of arctic sea ice thickness using high-resolution spaceborne polarimetric SAR data. IEEE Trans. Geosci. Remote Sens. 50, 13–22.

Lidmar-Bergström, K., 1997. A long-term perspective on glacial erosion. Earth Surf. Process. Landforms 22, 297–306. doi:10.1002/(SICI)1096-9837(199703)22:3<297::AID-ESP758>3.0.CO;2-R

Moghaddam, M., Saatchi, S., Cuenca, R.H., 2000. Estimating subcanopy soil moisture with radar. J. Geophys. Res. Atmos. 105, 14899–14911. doi:10.1029/2000JD900058

Oh, Y., 2004. Quantitative retrieval of soil moisture content and surface roughness from multipolarized radar observations of bare soil surfaces. IEEE Trans. Geosci. Remote Sens. 42, 596–601. doi:10.1109/TGRS.2003.821065

Oh, Y., Sarabandi, K., Ulaby, F.T., 2002. Semi-empirical model of the ensemble-averaged differential Mueller matrix for microwave backscattering from bare soil surfaces. IEEE Trans. Geosci. Remote Sens. 40, 1348–1355. doi:10.1109/TGRS.2002.800232

Oh, Y., Sarabandi, K., Ulaby, F.T., 1992. An empirical model and an inversion technique for radar scattering from bare soil surfaces. IEEE Trans. Geosci. Remote Sens. 30, 370–381. doi:10.1109/36.134086

Osinski, G.R., Lee, P., Spray, J.G., Parnell, J., Lim, D.S.S., Bunch, T.E., Cockell, C.S., Glass, B., 2005. Geological overview and cratering model for the Haughton impact structure, Devon Island, Canadian High Arctic. Meteorit. Planet. Sci. 40, 1759–1776. doi:10.1111/j.1945-5100.2005.tb00145.x

Park, S.E., Moon, W.M., Kim, D.J., 2009. Estimation of surface roughness parameter in intertidal mudflat using airborne polarimetric SAR data. IEEE Trans. Geosci. Remote Sens. 47, 1022–1031. doi:10.1109/TGRS.2008.2008908

Price, R.J., Clayton, K.M., 1973. Glacial and fluvioglacial landforms. Oliver and Boyd, London.

Schuler, D.L., Kasilingam, D., Nesti, G., 2002. Surface roughness and slope measurements using polarimetric SAR data. IEEE Trans. Geosci. Remote Sens. 40, 687–698. doi:10.1109/TGRS.2002.1000328

Shi, J., Dozier, J., 2000. Estimation of snow water equivalence using particle size. Water 38, 2475–2488. doi:10.1117/12.319499

Shi, J., Wang, J., Hsu, A.Y., O'Neill, P.E., Engman, E.T., 1997. Estimation of bare surface soil moisture and surface roughness parameter using L-band SAR image data. IEEE Trans. Geosci. Remote Sens. 35, 1254–1266. doi:10.1109/36.628792

Thompson, A.A., McLeod, I.H., 2004. The RADARSAT-2 SAR processor. Can. J. Remote Sens. 30, 336–344. doi:10.5589/m04-016

Tjuatja, S., Fung, A.K., Bredow, J., 1992. Scattering model for snow-covered sea ice. IEEE Trans. Geosci. Remote Sens. 30, 804–810. doi:10.1109/36.158876

Tornabene, L.L., Moersch, J.E., Osinski, G.R., Lee, P., Wright, S.P., 2005. Spaceborne visible and thermal infrared lithologic mapping of impact-exposed subsurface lithologies at the Haughton impact structure, Devon Island, Canadian High Arctic: Applications to Mars. Meteorit. Planet. Sci. 40, 1835–1858. doi:10.1111/j.1945-

5100.2005.tb00149.x

Ulaby, F.T., Moore, R.K., Fung, A.K., 1982. Microwave remote sensing : active and passive. Artech House, Norwood, MA.

Wu, T., Chen, K.S., Jiancheng Shi, Fung, A.K., 2001. A transition model for the reflection coefficient in surface scattering. IEEE Trans. Geosci. Remote Sens. 39, 2040–2050. doi:10.1109/36.951094

Chapter 4

4 Polarimetric SAR signatures for characterizing geological units in the Canadian Arctic*

Byung-Hun Choe, Gordon R. Osinski, Catherine D. Neish, and Livio L. Tornabene

4.1 Introduction

Rock surfaces in the Canadian Arctic are commonly weathered by glacial erosion and prolonged freeze-thaw cycles. These weathering processes can result in different surface roughness properties depending on rock properties (e.g., lithological composition, structure, and porosity) and their resistance to weathering (Bandis et al., 1983; Hudec, 1998, 1973; McCarroll and Nesje, 1996). For example, massive limestones often weather to very rough and blocky rock fragments and boulders, while thinly laminated shales and highly soluble gypsum rocks are weathered to relatively smooth and fine-grained plains (e.g., Dredge, 1992; Osinski et al., 2005). These different surface roughness properties translate to distinct scattering mechanisms from polarimetric synthetic aperture radar (SAR), which permits the better definition of geological units by integrating with the lithological properties derived from multispectral sensors (see Chapter 2). Surface roughness can be quantitatively estimated by computational inversion using radar

---

* This chapter article is currently in preparation to be submitted to *IEEE Transactions on Geoscience and Remote Sensing* for publication with the same title.

scattering models (e.g., Integral Equation Method (IEM) (Fung et al., 1992), Oh (Oh, 2004), and extended-Bragg (Hajnsek et al., 2003)). However, most radar scattering models have been developed based on bare soil surfaces, not weathered rock surfaces, so the inversion requires a new or modified radar scattering model with a much wider range of applicability (see Chapter 3).

Quad polarimetric SAR can generate radar backscattering responses at all polarizations including linear, elliptical, and circular polarization bases by the elliptical basis transformation of a quad polarimetric scattering matrix, which can be visualized in a 3-dimensional plot (Lee and Pottier, 2009; Zebker et al., 1987; Zyl et al., 1987). Polarization signatures have different shapes depending on the surface properties and physical structure of the targets, as their strong and weak backscattering responses occur at different polarizations (Lee and Pottier, 2009; Zebker et al., 1987; Zyl et al., 1987). The dominant scattering mechanism of target surfaces (e.g., single-bounce scattering from flat surfaces, double-bounce scattering from dihedral structures, multiple scattering from rough surfaces, or volume scattering from dense vegetation) can therefore be inferred from the different shapes of a surface's polarization signature (Lee and Pottier, 2009; Zebker et al., 1987; Zyl et al., 1987). There have been studies relating polarization signatures to vegetation density (Evans et al., 1988), crop residue monitoring (De Matthaeis et al., 1994; McNairn et al., 2002), ship detection (Touzi et al., 2015), and land classification (Huang et al., 2017; Jafari et al., 2015; Singhroy and Molch, 2004) based on distinct target structures and their polarization responses. For example, van Zyl et al. (1987), De Matthaeis et al. (1991), and McNairn et al. (2002) have reported that the pedestal height (i.e., the minimum backscattering power) of a polarization signature is related to surface roughness; pedestal height values are higher with increasing surface roughness.

In this chapter, we describe the polarization signatures of different geological units with varying surface roughness properties, from fine-grained fluvioglacial sediments to weathered carbonate bedrock, in the Tunnunik and Haughton impact structures in the Canadian Artic. We calculate the pedestal height and the standard deviation of the linear co-polarization responses to characterize the polarimetric SAR backscattering responses. Finally, we investigate how the polarization signature-derived parameters are correlated to surface roughness.

4.2 Polarimetric SAR data and ground truth collection

RADARSAT-2 (C-band, 5.405 GHz) Wide Fine Quad-polarimetric data were acquired from the Tunnunik and Haughton impact structures during the summers of 2015 and 2016, coincident with our field work. The Tunnunik acquisition was obtained with the FQ7W (i.e., 24.9~28.3° incidence angles) beam mode in a descending orbit on July 11, 2015, and the Haughton acquisition was obtained at the FQ19W (i.e., 37.7~40.4°) beam mode in an ascending orbit on August 8, 2016 (see Table 3.1). They were processed at the single look complex (SLC) level at a pixel spacing of 4.7 m (slant range) by 5.1 m (azimuth) for a swath of 50 km (ground range) by 25 km (azimuth) (Thompson and McLeod, 2004). The SLC products were radiometrically calibrated and processed into the 2 by 2 polarimetric scattering matrix [S] using the Polarimetric SAR Data Processing and Education Tool (PolSARpro) (Lee and Pottier, 2009).

A total of 27 high-resolution digital elevation models were also collected from the Tunnunik structure (11 scans, July–August, 2015) and the Haughton structure (16 scans, July–August, 2016) using a tripod-mounted LiDAR scanner (ILRIS-3D from Optech) during the associated field work (see Chapter 3.2 for details). The LiDAR scans were acquired as 3-dimensional point clouds at a spacing of 2 mm in X and Y and 1 mm in Z for an approximately 5 m wide and 10 m long area (Fig. 4.1). One-dimensional surface profiles with a length of 3 to 4 m were generated from the LiDAR scans to calculate surface roughness (i.e., root mean square (RMS) height; the standard deviation of surface height (Z) values). Ten surface profiles were extracted from each scan, and then averaged for a representative RMS height value.

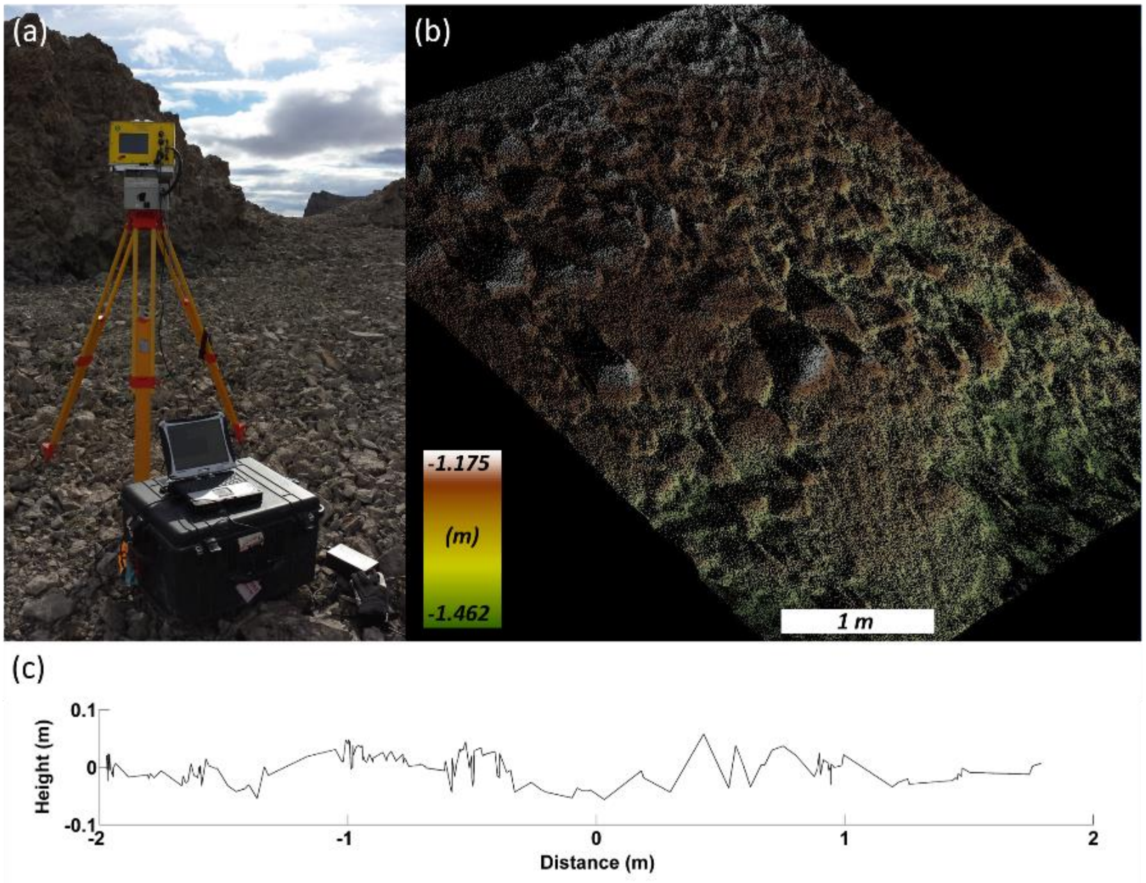

Figure 4.1. An example of in situ surface roughness measurements. (a) A tripod LiDAR was used to scan weathered rock surfaces at the Haughton impact structure (~1.7m tripod-mounted LiDAR for scale). (b) A 3-D point cloud representing surface topography was acquired from the LiDAR scan. The colour bar represents the elevation from the LiDAR scanner. (c) A series of 1-D surface profiles were extracted from the LiDAR scan to characterize the surface roughness of each site.

4.3 Methods

4.3.1 Polarization ellipse

The polarization state of electromagnetic wave propagation can be characterized by the orientation (ϕ) and ellipticity (τ) of the polarization ellipse (Lee and Pottier, 2009) (Fig. 4.2). The ellipse orientation is the angle between the major axis of the polarization ellipse and the x axis of the electromagnetic wave plane ranging from 0 to 180°. The ellipticity is the angle of the vector from the vertex to the co-vertex to determine the polarization ellipse shape (i.e., how nearly circular the polarization ellipse is) ranging from -45 to 45°. For example, horizontal polarization, 45°-rotated linear polarization, and vertical polarization are characterized by ϕ=0°, ϕ=45°, and ϕ=90°, respectively, with τ=0° for all (i.e., τ=0° means linear polarizations). The left and right circular polarizations are characterized by τ=45° and τ=-45°, respectively, regardless of ϕ.

4.3.2 Polarization basis change and 3-dimensional signature plot

Quad polarimetric SAR provides a single look complex (SLC) scattering matrix $[S]$ of HH, HV, VH, and VV polarizations for each pixel, which is given by

$$[S] = \begin{bmatrix} S_{hh} & S_{hv} \\ S_{vh} & S_{vv} \end{bmatrix}$$

(4.1)

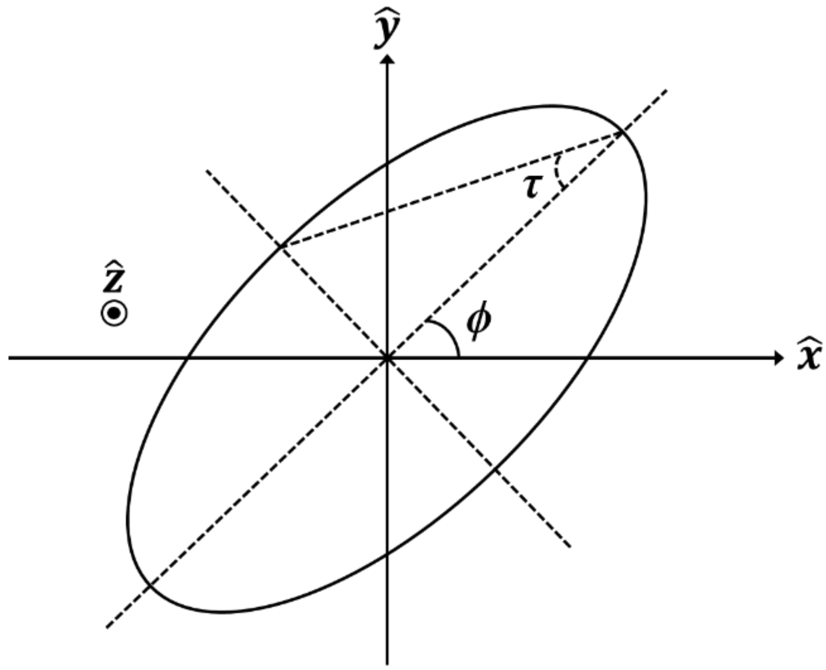

Figure 4.2. Polarization ellipse (ϕ: ellipse orientation angle, τ: ellipticity angle, modified from (Lee and Pottier, 2009)). $\hat{\boldsymbol{x}}$, $\hat{\boldsymbol{y}}$, and $\hat{\boldsymbol{z}}$ represent the axes of electromagnetic wave propagation plane.

where *Sij* is the complex scattering coefficient containing the amplitude and phase information for each polarization. Here, i=transmitting channel, j=receiving channel, h=horizontally polarized, and v=vertically polarized; for example, S_{hv} is the complex scattering coefficient transmitted through the horizontally polarized channel and received through the vertically polarized channel). The scattering matrix can be transformed to a different polarization state by the polarimetric basis change matrix $[U]$, which is given by

$$[U] = [U(\phi)][U(\tau)][U(\alpha)] = \begin{bmatrix} cos\,\phi & -sin\,\phi \\ sin\,\phi & cos\,\phi \end{bmatrix} \begin{bmatrix} cos\,\tau & isin\,\tau \\ isin\,\tau & cos\,\tau \end{bmatrix} \begin{bmatrix} e^{+i\alpha} & 0 \\ 0 & e^{-i\alpha} \end{bmatrix}$$

(4.2)

$$[S'] = [U]^T [S][U]$$

(4.3)

where α is the absolute phase term, and S' is a transformed matrix for a given ϕ and τ (Appendix G). The absolute phase α is an arbitrary parameter depending on the distance from a radar sensor to a target and does not affect the power of the polarization signature, so we considered α=0 here. Based on polarimetric scattering coefficients at a variety of orientations (ϕ) and ellipticity angles (τ) generated from a quad polarimetric scattering matrix, 3-dimensional co-polarization and cross-polarization power signature plots can be generated, and normalized between 0 and 1 by dividing the power responses by the maximum power (Fig. 4.3). A horizontal dipole produces the strongest backscattering at ϕ=0° (=180°) and τ=0°, and the weakest backscattering at ϕ=90° and τ=0° (Fig. 4.3a, vice versa for a vertical dipole). Likewise, a 45°-rotated dipole has a peak at ϕ=45° and τ=0° with a negative peak at ϕ=-45° (=135°) and τ=0° (Fig. 4.3b). The backscattering from a dihedral structure, common in urban buildings, is characterized by two negative peaks indicating no backscattering responses at ϕ=45°, -45° and τ=0°, with the strongest backscattering response at ϕ=0°, 90° for all τ angles (i.e., regardless of linear, ellipse, or circular polarization) (Fig. 4.3c). A trihedral structure such as a corner reflector produces the same strong backscattering at all linear polarizations (Fig. 4.3d).

4.3.3 Pedestal height and standard deviation of linear co-polarizations (SDLP)

The pedestal height of the 3-dimensional co-polarization signature plot represents the ratio of the minimum co-polarization power to the maximum co-polarization power (Zyl et al., 1987). It is related to the depolarization of the signal (i.e., the increase of unpolarized components in the wave scattered from the fully polarized transmitted wave) due to multiple scatterers (e.g., multiple scattering from rough surfaces and volume scattering from dense vegetation or forest) and/or noise (Evans et al., 1988; McNairn et al., 2002). While polarization signatures of fully polarized transmitted and received waves have a zero pedestal height as the examples shown in Figure. 4.3, the pedestal height rises with increasing the minimum power at all polarizations as depolarized backscattering increases (Evans et al., 1988; McNairn et al., 2002).

Different shapes of co-polarization signatures are also noted by significantly varying backscattering responses at linear polarizations. Here, besides the pedestal height, we calculated the standard deviation of linear co-polarization responses (SDLP) depending on different polarization signatures of geological units, and suggests it as a new parameter to characterize target surface properties. We then analyzed their sensitivities and correlations to in situ surface roughness measurements by calculating the least squares regression line. The region of interest (ROI) for each geological unit was delineated by building a polygon on the Pauli composite of the RADARSAT-2 quad polarimetric data (Cloude and Pottier, 1996). Next, the scattering matrices of pixels within the polygon (approximately 450~650 pixels) were integrated into an averaged scattering matrix $[\bar{S}]$, from which a representative polarization signature for each unit was generated. Surface roughness measurements collected within a delineated polygon were also averaged. The RMS height values were averaged from more than 2 LiDAR scans if applicable. The averaged RMS height value was compared to the pedestal height and the SDLP calculated from the co-polarization signature of each unit.

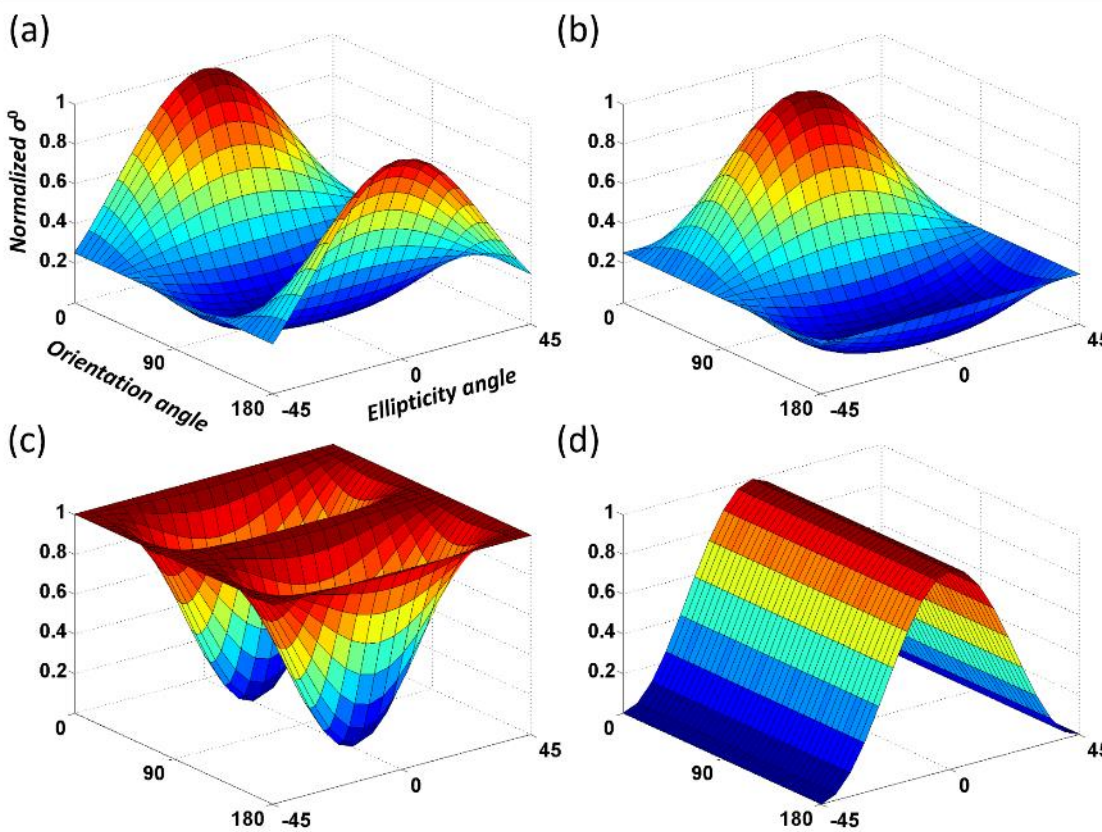

Figure 4.3. Normalized co-polarization signatures of a horizontal dipole (a), a 45°-rotated dipole (b), a dihedral structure (c), and a trihedral corner reflector (d).

4.4 Results and discussion

Figure 4.4 shows the co-polarization signatures of 4 different geological units in the Tunnunik impact structure: fine-grained fluvioglacial sediments (Fig. 4.4a), chert-bearing dolomites of the Victoria Island formation (Figs. 4.4b and 4.4c), dolomites of the Victoria Island formation (Fig. 4.4d), and dolomites covered by silica coatings of the Victoria Island formation (Fig. 4.4e) (see Chapter 2 for geological unit mapping of the Tunnuink impact structure). Figure 4.5 shows the co-polarization signatures from the Haughton structure, which has more diverse geological units: the Haughton formation of fine-grained lacustrine sediments (Fig. 4.5a), fine-grained impact melt rock deposits (Fig. 4.5b), the Bay Fiord formation (Fig. 4.5c), the Eleanor River formation (Fig. 4.5d), the Lower member of the Allen Bay formation (Figs. 4.5e and 4.5f), the Thumb Mountain formation (Fig. 4.5g), and Quaternary fluvioglacial sediments comprising gravels and cobbles (Figs. 4.5h and 4.5i) (see the Haughton geological map in Fig. 1.6).

The fine-grained sediments (Figs. 4.4a and 4.5a), impact melt rocks (Fig. 4.5b), and the outcrops of the Bay Fiord formation (Fig. 4.5c) within the Haughton structure all show dominant single-bounce surface scattering (coloured in dark blue) in the Pauli composites. In the co-polarization signatures, they are characterized by a peak centred at the VV polarization (i.e., ϕ=90° and τ=0°) with pedestal heights lower than ~0.2. In contrast, weathered carbonate rock units (i.e., the Victoria Island formation (Fig. 4.4b~4.4e), the Eleanor River formation (Fig. 4.5d), the Lower member of Allen Bay formation (Figs. 4.5e and 4.5f), and the Thumb Mountain formation (Figs. 4.5g)) and the Quaternary fluvioglacial sediments of gravels and cobbles (Figs. 4.5h and 4.5i) are characterized by multiple-diffused scattering and double-bounce scattering (coloured in yellow) in the Pauli composites. In the co-polarization signatures, they have higher pedestal heights and relatively little variation at linear polarizations.

Relatively smooth surfaces that produce single-bounce scattering show more variation between all polarization responses. This indicates that they produce strong backscattering only at a limited range of polarizations centred at the maximum at the VV polarization (Ulaby et al., 1982). Accordingly, they appear with lower pedestal heights due to the vertical difference between the minimum and the maximum backscattering responses, and higher horizontal variation at linear polarizations. In contrast, the variation in linear polarization decreases in the weathered carbonate rock units and fluvioglacial sediments of gravels and cobbles. These are typically rough surfaces represented by multiple-diffused and double-bounce scattering. Rough surfaces weathered to cobbles and coarse boulders have higher pedestal heights with increasingly depolarized backscattering components due to multiple scatterers. They produce similarly strong backscattering (approaching unity) in the normalized co-polarization power at any linear polarization, most similar to the idealized trihedral corner reflector backscattering (Fig. 4.3d).

The calculated pedestal heights and SDLPs were compared to the surface roughness measurements collected from the defined geological units (Fig. 4.6). The pedestal height is proportional to the RMS height with a correlation coefficient of ~0.6 (R^2=0.3721); it increases with the increase of the RMS height (Fig. 4.6a). The SDLP is inversely proportional to the RMS height with a correlation coefficient of ~-0.8 (R^2=0.6676); it decreases with the increase of the RMS height (Fig. 4.6b). The SDLP differentiates between fine-grained smooth surfaces (RMS heights < ~0.02 m) and weathered rock surfaces (RMS heights > ~0.03 m) well. The pedestal height also differentiates the fine-grained smooth surfaces well, but the variation is particularly significant at the RMS heights between 0.02 and 0.04 m. For the intermediate rough surfaces with RMS heights between 0.02 and 0.04 m, the SDLP also does not differentiate them from the rough surfaces with RMS heights > ~0.04 m, as they all are similarly distributed at the narrow range of SDLPs between 0.02 and 0.04. Thus, we applied a ratio of the pedestal height to the SDLP (PDH/SDLP) to maximize the differences between smooth, medium rough, and rough surfaces (marked by dot-dashed lines in Fig. 4.6c).

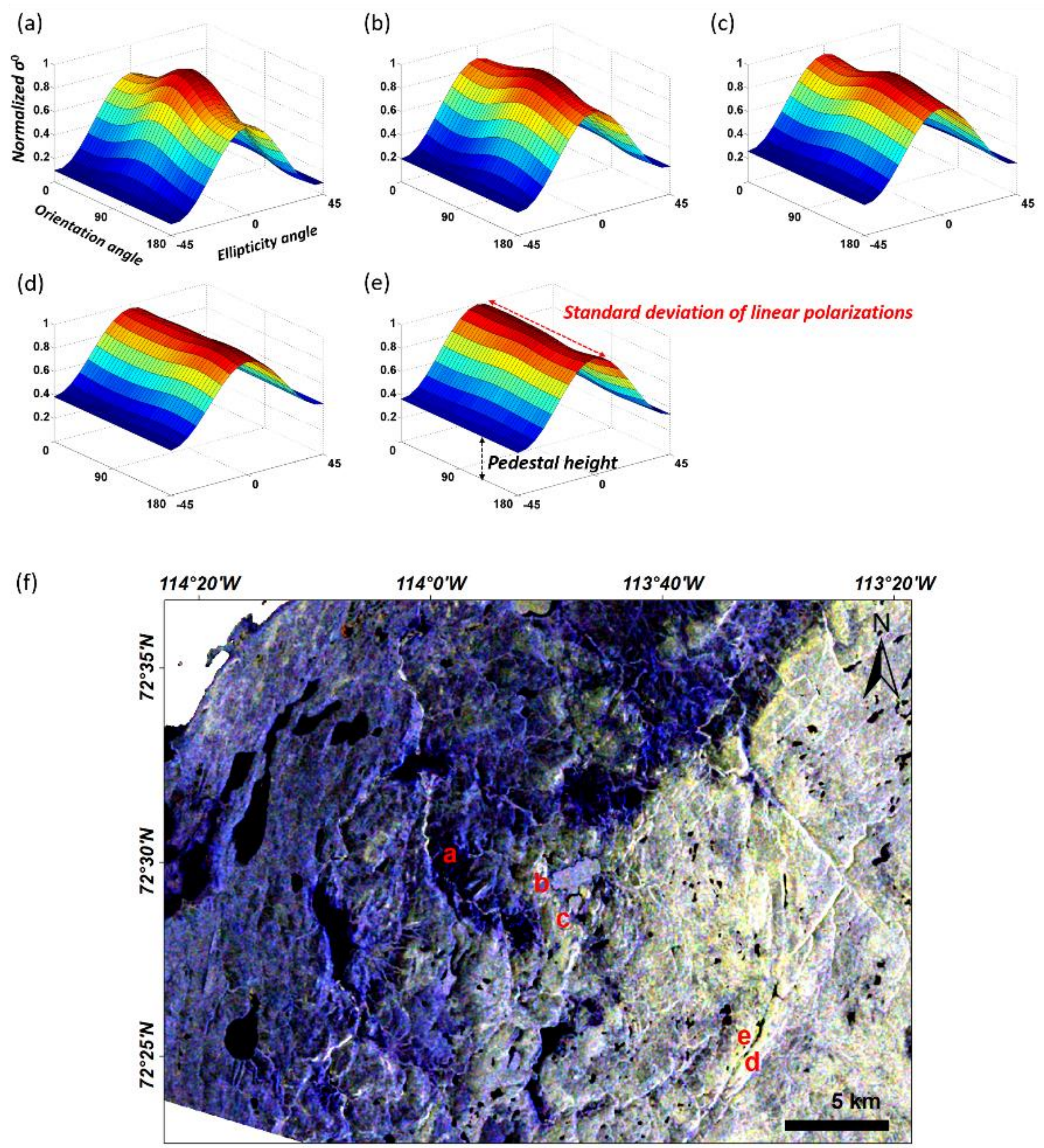

Figure 4.4. Co-polarization signatures of geological units in the Tunnunik structure ((a) fine-grained Quaternary fluvioglacial sediments (QS), (b), (c) Victoria Island formation (chert-bearing dolomites, VI1), (d) Victoria Island formation (dolomites, VI2)), and (e) Victoria Island formation (silica-coated dolomites, VI3)) and their locations on the Pauli RGB composite (f; double-bounce scattering (red, $|\boldsymbol{S_{hh}} - \boldsymbol{S_{vv}}|^2/2$), multiple-diffused scattering (green, $2|\boldsymbol{S_{hv}}|^2$), and single-bounce scattering (blue, $|\boldsymbol{S_{hh}} + \boldsymbol{S_{vv}}|^2/2$)). Field measurements were also collected from these locations. The black and red dashed lines with double headed-arrows in (e) denote the pedestal height and the basis of the standard deviation of linear polarizations, respectively.

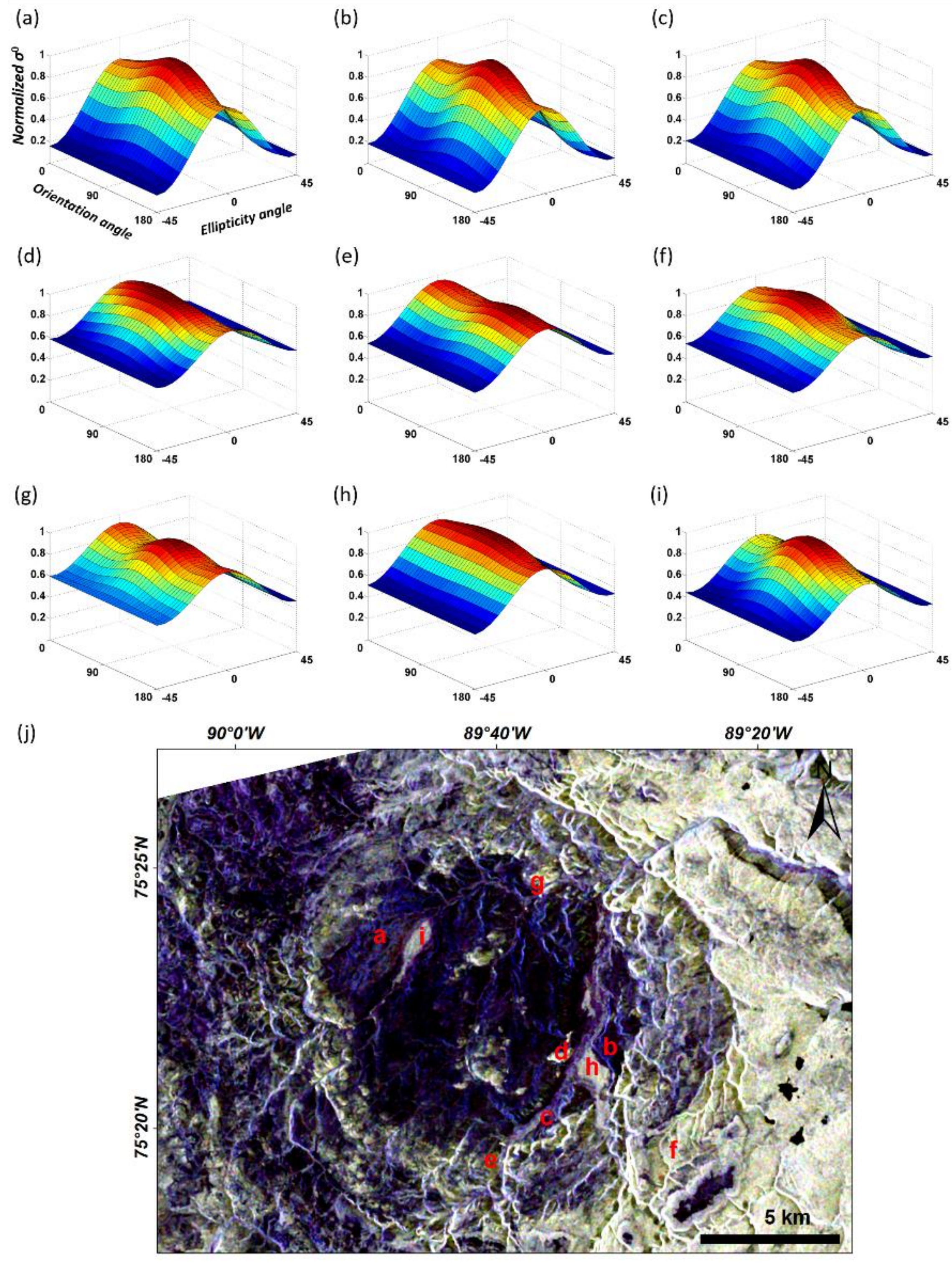

(a)
(b)
(c)
(d)
(e)
(f)
(g)
(h)
(i)
(j)
Normalized σ^0
Orientation angle
Ellipticity angle
90°0'W
89°40'W
89°20'W
75°25'N
75°20'N
N
a
b
c
d
e
f
g
h
i
5 km

(continued)

Figure 4.5. Co-polarization signatures of geological units in the Haughton structure ((a) Haughton formation (fine-grained lacustrine sediments, HF), (b) impact melt breccia deposits (IM), (c) Bay Fiord formation (BF), (d) Eleanor River formation (ER), (e), (f) Allen Bay formation (Lower member, AB), (g) Thumb Mountain formation (TM), and (h), (i) Quaternary fluvioglacial sediments (gravels and cobbles, QS2) and their locations on the Pauli composite (j; double-bounce scattering (red, $|\boldsymbol{S_{hh}} - \boldsymbol{S_{vv}}|^{\boldsymbol{2}}/\boldsymbol{2}$), multiple-diffused scattering (green, $\boldsymbol{2}|\boldsymbol{S_{hv}}|^{\boldsymbol{2}}$), and single-bounce scattering (blue, $|\boldsymbol{S_{hh}} + \boldsymbol{S_{vv}}|^{\boldsymbol{2}}/\boldsymbol{2}$)). Field measurements were also collected from these locations.

The geological units of the Tunnunik and Haughton structures were classified into three categories according to the PDH/SDLP as follows; 1) (smooth) fine-grained sediments (0~4; QS, HF, IM, BF), 2) (medium rough) unsorted sediments with weathered rocks interspersed (4~10; VI1, QS2), and 3) (rough) weathered rocks of cobbles and coarse boulders (> ~10; VI2, VI3, ER, AB, TM, QS2) (Figs. 4.6c and 4.7). It is notable that the two units of the Quaternary fluvioglacial deposits of gravels and cobbles (QS2) in the Haughton structure are classified into different groups (Fig. 4.6c); one (Fig. 4.5h) in the medium rough category and the other (Fig. 4.5i) in the rough category, respectively. The difference between the two QS2 units is more obvious in the SDLP (Fig. 4.6b) than in the pedestal height (Fig. 4.6a). This may be caused by the difference in sorting and angularity of the Quaternary fluvioglacial sediments (Fig. 4.7f). Relatively well sorted and rounded sediments of gravels and cobbles with lower RMS height values are more distinctly differentiated by the SDLP calculated by backscattering responses varying depending on different linear polarization, compared to the pedestal height determined by the difference between the maximum and the minimum backscattering responses.

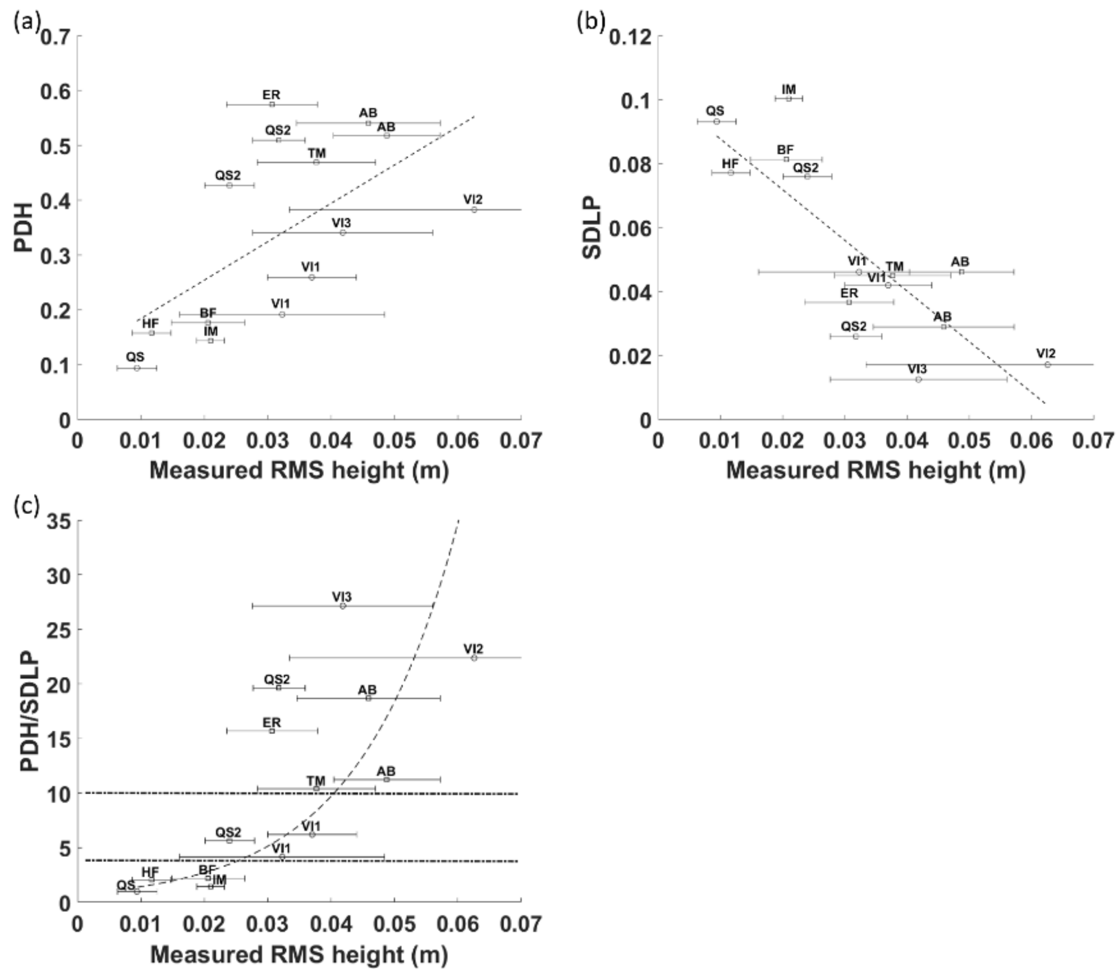

Figure 4.6. Comparison between polarization signature parameters and measured RMS heights with the least squares regression lines (dashed). The circles (Tunnunik) and squares (Haughton) denote the average of surface roughness measurements for each unit, and the error bars denote the standard deviations. (a) Pedestal height (PDH). (b) Standard deviation of linear co-polarizations (SDLP). (c) PDH/SDLP (the dot-dashed lines denote where the PDH/SDLP are 4 (medium rough) and 10 (rough), respectively). Abbreviations: QS=fine-grained Quaternary fluvioglacial sediments (Fig. 4.4a); VI1= Victoria Island formation (chert-bearing dolomites, Figs. 4.4b and 4.4c); VI2= Victoria Island formation (dolomites, Fig. 4.4d); VI3=Victoria Island formation (silica-coated dolomites, Fig. 4.4e); HF= Haughton formation (Fig. 4.5a); IM= impact melt breccia deposits (Fig. 4.5b); BF= Bay Fiord formation (Fig. 4.5c); ER= Eleanor River formation (Fig. 4.5d); AB= Allen Bay formation (Lower member, Figs. 4.5e and 4.5f); TM= Thumb Mountain formation (Fig. 4.5g); QS2= Quaternary fluvioglacial sediments (gravels and cobbles; Figs. 4.5h and 4.5i).

Figure 4.7. Field photos of the different geologic units studied in this work. (a) Fine-grained Quaternary fluvioglacial sediments (QS). (b) Impact melt breccia deposits (IM). (c) Victoria Island formation (chert-bearing dolomites, VI1). (d) Victoria Island formation (silica-coated dolomites, VI3). (e) Allen Bay formation (Lower member, AB). (f) Quaternary fluvioglacial sediments (gravels and cobbles, QS2). A ~9 by 5 cm card is placed for scale.

4.5 Conclusions

We investigated the surface roughness properties of geological units in the Tunnunik and Haughton impact structures in the Canadian Arctic. The surface roughness derived from in situ measurements was compared to the RADARSAT-2 polarization signature and its derived parameters, the pedestal height and the standard deviation of linear co-polarization responses (SDLP). The SDLP showed a better correlation with surface roughness measurements; it was able to discern the difference in the sorting and angularity of weathered rock surfaces. Based on the ratio of the PDH to the SDLP, the medium rough units, such as unsorted surfaces with fine-grained sediments and well sorted rounded cobble sediments, were differentiated from the roughest units that consist only of weathered rocks. Consequently, the geological units were classified into three different roughness groups. These results show a great potential to apply SAR polarization signatures to classify the surface roughness properties of geological units, though not as much detail as estimated surface roughness by radar scattering model inversion methods. Future work could compare the polarization signatures of weathered rock surfaces for radar frequencies besides the C-band RADARSAT-2.

4.6 References

Bandis, S.C., Lumsden, A.C., Barton, N.R., 1983. Fundamentals of rock joint deformation. Int. J. Rock Mech. Min. Sci. Geomech. Abstr. 20, 249–268.

Cloude, S.R., Pottier, E., 1996. A review of target decomposition theorems in radar polarimetry. IEEE Trans. Geosci. Remote Sens. 34, 498–518.

De Matthaeis, P., Ferraxzoli, P., Guerriero, L., Schiavon, G., Solimini, D., Tognolatti, P., 1991. Radar response to vegetation parameters: Comparison between theory and Maestro-1 results, in: IEEE Geoscience and Remote Sensing Symposium. pp. 685–688.

De Matthaeis, P., Schiavon, G., Solimini, D., 1994. Effect of scattering mechanisms on polarimetric features of crops and trees. Int. J. Remote Sens. 15, 2917–2930. doi:10.1080/01431169408954292

Dewing, K., Pratt, B.R., Hadlari, T., Brent, T., Bédard, J., Rainbird, R.H., 2013. Newly identified "Tunnunik" impact structure, Prince Albert Peninsula, northwestern Victoria Island, Arctic Canada. Meteorit. Planet. Sci. 48, 211–223. doi:10.1111/maps.12052

Dredge, L.A., 1992. Breakup of limestone bedrock by frost shattering and chemical weathering , eastern Canadian Arctic. Arct. Alp. Res. 24, 314–323.

Evans, D.L., Farr, T.G., Van Zyl, J.J., Zebker, H.A., 1988. Radar polarimetry: Analysis tools and applications. IEEE Trans. Geosci. Remote Sens. 26, 774–789. doi:10.1109/36.7709

Fung, A.K., Li, Z., Chen, K.S., 1992. Backscattering from a randomly rough dielectric surface. IEEE Trans. Geosci. Remote Sens. 30, 356–369. doi:10.1109/36.134085

Hajnsek, I., Cloude, S.R., Lek, J., Eric, P., 2003. Inversion of surface parameters from polarimetric SAR data 41, 1095–1097.

Huang, X., Wang, J., Shang, J., Liao, C., Liu, J., 2017. Application of polarization signature to land cover scattering mechanism analysis and classification using multi-temporal C-band polarimetric RADARSAT-2 imagery. Remote Sens. Environ. 193, 11–28. doi:10.1016/j.rse.2017.02.014

Hudec, P.P., 1998. Rock properties and physical processes of rapid weathering and deterioration, in: Proceedings of 8th International Congress of IAEG. pp. 335–341.

Hudec, P.P., 1973. Weathering of rocks in Arctic and Sub-arctic environment, in: Proceedings of the Symposium on the Geology of the Canadian Arctic. pp. 313–335.

Jafari, M., Maghsoudi, Y., Zoej, M.J.V., 2015. A new method for land cover characterization and classification of polarimetric SAR data using polarimetric signatures. Int. J. Appl. Earth Obs. Geoinf. 8, 3595–3607. doi:10.1109/jstars.2014.2387374

Lee, J.-S., Pottier, E., 2009. Polarimetric radar imaging: from basics to applications. CRC Press, New York.

McCarroll, D., Nesje, A., 1996. Rock surface roughness as an indicator of degree of rock surface weathering. Earth Surf. Process. Landforms 21, 963–977. doi:10.1002/(SICI)1096-9837(199610)21:10<963::AID-ESP643>3.0.CO;2-J

McNairn, H., Duguay, C., Brisco, B., Pultz, T., 2002. The effect of soil and crop residue characteristics on polarimetric radar response. Remote Sens. Environ. 80, 308–320. doi:10.1016/S0034-4257(01)00312-1

Newman, J.D., Osinski, G.R., 2016. Geological mapping of the Tunnunik impact structure, Victoria Island, Canadian High Arctic, in: 47th Lunar and Planetary Science Conference. p. Abstract #1591. doi:10.1038/ngeo2474.

Oh, Y., 2004. Quantitative retrieval of soil moisture content and surface roughness from multipolarized radar observations of bare soil surfaces. IEEE Trans. Geosci. Remote Sens. 42, 596–601. doi:10.1109/TGRS.2003.821065

Osinski, G.R., Spray, J.G., Lee, P., 2005. A case study of impact-induced hydrothermal activity: The Haughton impact structure, Devon Island, Canadian High Arctic. Meteorit. Planet. Sci. 40, 1789–1812. doi:10.1111/j.1945-5100.2005.tb00147.x

Singhroy, V., Molch, K., 2004. Geological case studies related to RADARSAT-2. Can. J. Remote Sens. 30, 893–902. doi:10.5589/m04-050

Thompson, A.A., McLeod, I.H., 2004. The RADARSAT-2 SAR processor. Can. J. Remote Sens. 30, 336–344. doi:10.5589/m04-016

Tornabene, L.L., Moersch, J.E., Osinski, G.R., Lee, P., Wright, S.P., 2005. Spaceborne visible and thermal infrared lithologic mapping of impact-exposed subsurface lithologies at the Haughton impact structure, Devon Island, Canadian High Arctic: Applications to Mars. Meteorit. Planet. Sci. 40, 1835–1858. doi:10.1111/j.1945-5100.2005.tb00149.x

Touzi, R., Hurley, J., Vachon, P.W., 2015. Optimization of the degree of polarization for enhanced ship detection using polarimetric RADARSAT-2. IEEE Trans. Geosci. Remote Sens. 53, 5403–5424.

Ulaby, F.T., Moore, R.K., Fung, A.K., 1982. Microwave remote sensing : active and passive. Artech House, Norwood, MA.

Zebker, H.A., van Zyl, J.J., Held, D.N., 1987. Imaging radar polarimetry from wave synthesis. J. Geophys. Res. 92, 683–701. doi:10.1029/JB092iB01p00683

Zyl, J.J. Van, Zebker, H.A., Elachi, C., 1987. Imaging radar polarization signatures: Theory and observation. Radio Sci. 22, 529–543.

Chapter 5

5 Conclusions

5.1 Summary and general discussion

This thesis examined the combined use of polarimetric SAR and multispectral sensors for remote predictive mapping in the Arctic. The research questions raised by this thesis are addressed by the major findings as follows:

1) Can the physical surface properties of different geological units in the Canadian Arctic be determined using radar scattering mechanisms investigated by polarimetric SAR decomposition techniques?

The Tunnunik impact structure was mapped in a more detailed scale than the 1:500,000 map of the Geological Survey of Canada by integrating multispectral analysis and polarimetric SAR decomposition (Chapter 2). The remote predictive map defined 4 different geological units in the Tunnunik structure as follows: 1) (smooth) fluvioglacial deposits; 2) (moderately rough) cherty limestones; 3) (rough) dolomitic limestones; and 4) (rough) silica-bearing unit possibly representing mudstones and siltstones. Field observations and XRD analysis of rock samples collected from each unit confirmed that the fluvioglacial deposit unit matches well. The cherty limestone unit turned out to be chert-bearing dolostone with minor quartz and calcite, and the dolomitic limestone unit consisted predominantly of dolostone. The rough silica-bearing unit was revealed to be dolostone with minor calcite covered by thin, silicified surface coatings. The rough surfaces characterized by multiple scattering in the polarimetric SAR decomposition were related to occurrences of resistant dolostone weathered to blocky boulders. In the Haughton structure, thick-bedded limestone and dolomite units (i.e., Allen Bay Formation, Thumb Mountain Formation, Eleanor River formation) weathered to cobbles and coarse boulders were characterized by multiple scattering, while fine-grained deposits (i.e., impact melt rocks, Haughton Formation) and evaporite-rich units weathered to fine-grained plains (i.e, Bay Fiord Formation) were characterized by single-bounce scattering (Chapter 4).

2) How can quantitative surface parameters, such as surface roughness and soil moisture, be estimated using a radar scattering model inversion method? And how can the semi-empirical radar scattering model developed based on bare soil surfaces be modified for weathered rock surfaces much rougher than soil sediments?

A newly modified semi-empirical radar scattering model to estimate the surface roughness of weathered rocks was suggested (Chapter 3). The radar scattering models developed based on bare soil surfaces are applied to a very limited range of surface roughness. A semi-empirical scattering model proposed by Oh (2004) was applied well to fine-grained deposits, but underestimated the surface roughness for roughly weathered rocks showing a rapid saturation at the range of $ks > 3$. Thus, the Oh model was modified based on the least square curve fit of the cross-polarization ratios for surface roughness measurements from weathered rock units in the Tunnunik and Haughton structures. The modified model was successfully applied to estimate the surface roughness of roughly weathered rock units up to approximately 9 in ks without the rapid saturation feature at $ks > 3$.

3) How do the radar backscattering responses from different geological units vary depending on polarizations? And can the polarization signatures be parameterized to characterize the surface roughness of geological units?

Different polarimetric SAR signatures were investigated from a number of geological units in the Tunnunik and Haughton structures and characterized by calculating the pedestal height and the standard deviation of linear co-polarization responses (SDLP) (Chapter 4). The pedestal height showed a positive correlation coefficient of ~0.6 with surface roughness, while the SDLP showed a negative correlation coefficient of ~0.8 with surface roughness. The variation between the different polarization responses was highly dependent on the surface roughness of the geological units. The SDLP was thus suggested as a promising parameter to characterize surface roughness, in addition to the pedestal height that has been commonly used.

4) Can the polarimetric SAR-derived physical surface properties be associated with mineralogical and lithological properties characterized from multispectral sensors? How can they be combined for remote predictive geological mapping of the Canadian Arctic?

The surface roughness properties of the geological units were characterized by polarimetic SAR scattering mechanism and polarization signature analysis, and the surface roughness and volumetric soil moisture were estimated by the modified semi-empirical scattering model inversion. However, the surface roughness properties derived from polarimetric SAR could classify the geological units into only three categories relative to the radar wavelength: smooth, medium rough, and rough units. The volumetric soil moisture is estimated only for smooth bare soil surfaces such as fine-grained fluvioglacial deposits, not for weathered rock surfaces insensitive to the moisture content. Thus, it is very difficult to describe diverse geological units by polarimetric SAR alone.

A number of geological units are well defined by data from multispectral sensors, as the spectral signatures are more varied than the roughness properties derived from SAR. The spectral signatures, however, are subject to common cloud, snow, and ice cover due to the extreme weather in the Arctic and even sparse vegetation on surfaces. Also, as shown in the Tunnunik mapping (Chapter 2), surficial coatings can mislead the geological mapping. One of the carbonate rock units in the Victoria Island Formation (i.e., Unit 4) was interpreted as a silica-rich unit by multispectral analysis due to the silica coatings showing the similar spectral signature with the fluvioglacial deposits (i.e., Unit 1), even though it is mainly comprised of dolomite. However, the spectrally similar units were clearly differentiated by their different surface roughness properties from polarimetric SAR. Different surface roughness properties of geological units in the Canadian Arctic are attributed to their resistance to weathering, which also depends on their lithological properties. Thus, surface roughness properties derived from polarimetric SAR can play a complementary role to the spectral mapping on lithological properties. Polarimetric SAR combined with multispectral sensors can define geological units better by investigating both physical surface properties and lithology.

For future remote predictive mapping, it is suggested that the main composition of target lithology is best defined by TIR emissivity features. VNIR and SWIR reflectance can additionally contribute to the detection of the presence of surficial weathering (i.e., iron oxides) and clay minerals. While the scattering mechanisms and polarization signatures (i.e., pedestal height, SDLP) are indirect parameters relating to the surface roughness, the scattering model inversion method directly provides the quantitative surface roughness value itself with a more specified range. Thus, the estimated surface roughness parameter is more recommendable to characterize the surface roughness properties of geological units and integrate them into an automated mapping algorithm with the spectral parameters. Also, it is recommended to produce a 3-dimensional remote predictive map rendered on a DEM, as weathering and deposition processes by glacial activity in the Canadian Arctic and resultant surface roughness properties depend on elevation. High-resolution imagery such as Quickbird can provide very detailed surface texture and glacial and periglacial morphology that not visible from multispectral and polarimetric SAR data.

5.2 Future work

In this work, a remote predictive mapping approach based on meteorite impact structures was utilized as they expose the regional bedrocks of the Canadian Arctic. Based on the results of this study, new techniques and algorithms have been proposed. A logical next step is to extend the polarimetric SAR mapping combined with multispectral mapping to map the regional geology of western Victoria Island surrounding the Tunnunik impact structure and central Devon Island surrounding the Haughton impact structure. Pauli decomposition mosaics have been produced with multiple SAR acquisitions over northwestern Victoria Island and central Devon Island (Fig. 5.1). The central Devon Island mosaic shows a great match with vertically parallel regional stratigraphic layers and the outcrops preserved in the Haughton structure are also well observed with different scattering mechanisms. The Haughton impact structure and central Devon Island are an ideal region to show how effectively impact structure mapping can be extended to regional stratigraphy. A decision-tree mapping algorithm can be constructed for the Haughton structure as suggested in Chapter 2, and then a regional-scale remote predictive map can be produced by combining the Pauli decomposition mosaic (or surface roughness map) and spectral maps by Landsat and ASTER data covering central Devon Island into the decision-tree mapping algorithm. The geological units exposed in the Haughton structure can be compared to the regional bedrocks where they originated from. In addition to classifying geological units, polarimetric SAR can quantitatively assess the weathering and deposition processes in the Canadian Arctic by producing the surface roughness map. Northwestern Victoria Island reveals extensive glacial striation features toward Richard Collinson Inlet and Wynniatt Bay from Shaler Mountains. This indicates that glacial movement on the way to the Richard Collinson Inlet has deeply eroded the Tunnunik impact structure, which is quite distinct from the well-preserved Haughton structure. Thus, it is necessary to extract the glacial striation features on the SAR image using an automated lineament extraction algorithm (e.g., Wang and Howarth, 1990), and investigate how they effect the surface roughness. It would also be worthwhile to compare the difference in surface roughness between northwestern Victoria Island and central Devon Island. Furthermore, melting of snow cover and glaciers accelerated by rapid and ongoing climate change in the Arctic (Otto-Bliesner, 2006; Overpeck et al., 1997) and its subsequent surface changes in morphology, roughness, and moisture can be monitored by time-series mapping of polarimetric SAR.

Besides applying polarimetric SAR, further studies need to consider InSAR techniques to measure the movement of geological features in the Canadian Arctic (e.g., salt diapir rising, permafrost subsidence, glacier melting and retreat) (Mouginot et al., 2017; Rignot, 2006; Samsonov et al., 2016; Short et al., 2011). For example, Axel Heiberg Island in Nunavut is well known for the second highest concentration of salt diapirs in the world (Harrison and Jackson, 2014). A preliminary study to monitor the motion of salt diapirs on Axel Heiberg Island shows great potential for the quantitative measure of salt motion by applying time-series InSAR analysis (Fig. 5.2). This may be useful for locating salt diapirs as a potential reservoir for oil and gas resource exploration (Harrison and Jackson, 2014). However, the initial results show no correlation between motion in this region and the location of salt diapirs. Nonetheless, glacial movement was observed in this region through very fine fringe patterns from glacial inlets on Axel Heiberg Island (Fig. 5.2). InSAR monitoring of glacier melting and retreat and permafrost subsidence can provide important sources for land risk management and climate change assessment in the Canadian Arctic.

In conclusion, future remote predictive geological mapping needs to implement a multifaceted approach with all the information on mineralogical and lithological composition, morphology, roughness, moisture, and deformation of target surfaces. This can be accomplished by integrating polarimetric and interferometric SAR techniques with multi and hyperspectral analysis.

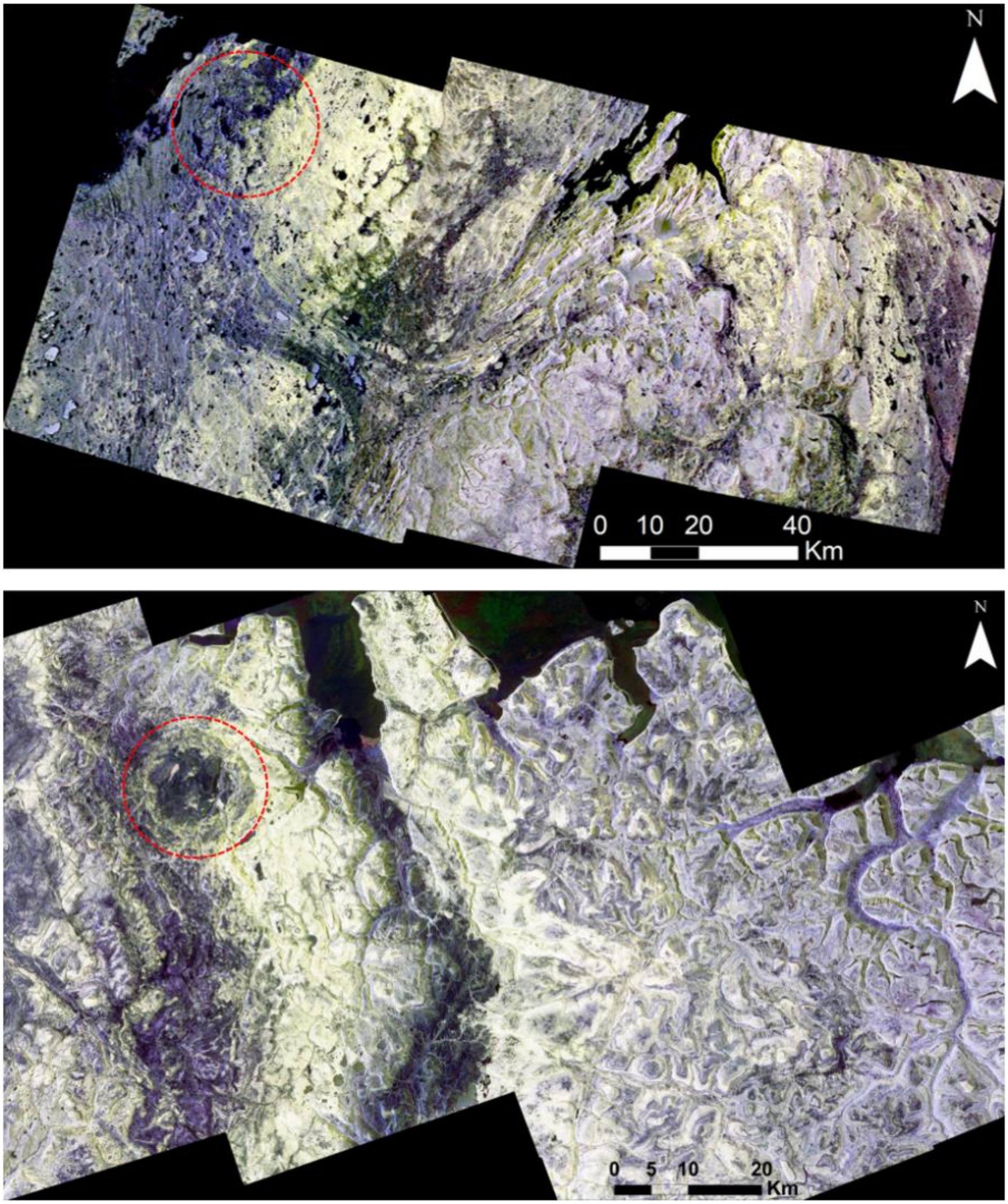

Figure 5.1. RADARSAT-2 Pauli decomposition mosaics of northwestern Victoria Island (upper, 18 acquisitions from July 2015) and central Devon Island (lower, 14 acquisitions from July 2015). The RGB channels represent double-bounce (red), multiple-diffused (green), and single-bounce (blue) scattering, respectively. The red circular dashed lines denote impact structures.

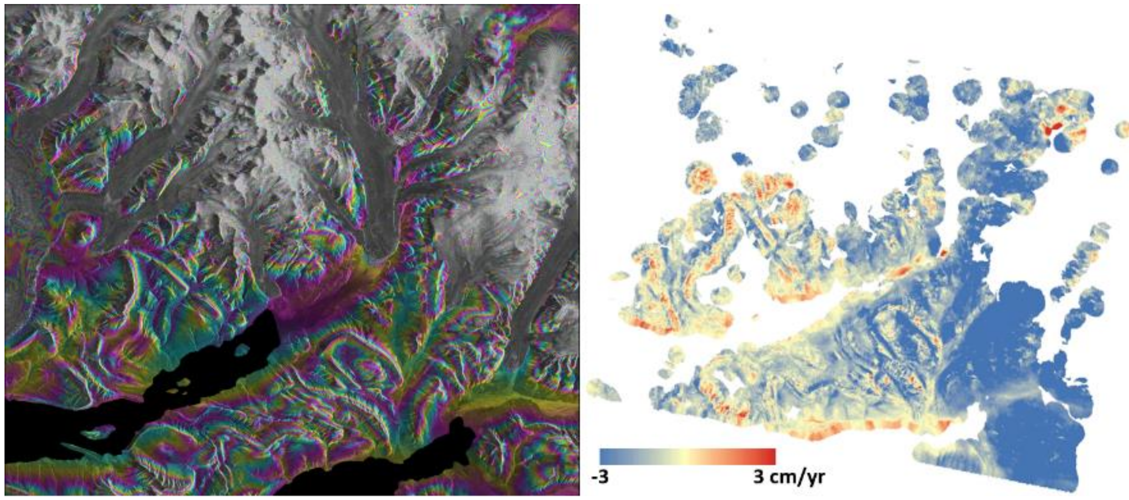

Figure 5.2. Example of RADARSAT-2 (HH, F5 mode) interferograms generated from Axel Heiberg Island (left, very fine fringes correspond to the locations of glaciers) and the average deformation rate map estimated from a total of 46 RADARSAT-2 InSAR pairs (right, positive values toward the red represent rising).

5.3 References

Harrison, J.C., Jackson, M.P.A., 2014. Exposed evaporite diapirs and minibasins above a canopy in central Sverdrup Basin, Axel Heiberg Island, Arctic Canada. Basin Res. 26, 567–596. doi:10.1111/bre.12037

Mouginot, J., Rignot, E., Scheuchl, B., Millan, R., 2017. Comprehensive annual ice sheet velocity mapping using Landsat-8, Sentinel-1, and RADARSAT-2 data. Remote Sens. 9, 1–20. doi:10.3390/rs9040364

Otto-Bliesner, B.L., 2006. Simulating Arctic climate warmth and icefield retreat in the last interglaciation. Science (80-.). 311, 1751–1753. doi:10.1126/science.1120808

Overpeck, J., Hughen, K., Hardy, D., Bradley, R., Case, R., Douglas, M., Finney, B., Gajewski, K., 1997. Arctic environmental change of the last four centuries. Science (80-.). 278, 1251–1256. doi:10.1126/science.278.5341.1251

Rignot, E., 2006. Changes in the velocity structure of the Greenland ice sheet. Science (80-.). 311, 986–990. doi:10.1126/science.1121381

Samsonov, S. V., Lantz, T.C., Kokelj, S. V., Zhang, Y., 2016. Growth of a young pingo in the Canadian Arctic observed by RADARSAT-2 interferometric satellite radar. Cryosphere 10, 799–810. doi:10.5194/tc-10-799-2016

Short, N., Brisco, B., Couture, N., Pollard, W., Murnaghan, K., Budkewitsch, P., 2011. A comparison of TerraSAR-X, RADARSAT-2 and ALOS-PALSAR interferometry for monitoring permafrost environments, case study from Herschel Island, Canada. Remote Sens. Environ. 115, 3491–3506. doi:10.1016/j.rse.2011.08.012

Wang, J., Howarth, P.J., 1990. Use of the Hough transform in automated lineament detection. IEEE Trans. Geosci. Remote Sens. 28, 561–567. doi:10.1109/TGRS.1990.572949

Appendices

Appendix A. Polarimetric SAR scattering matrix

The 2 by 2 quad polarimetric scattering matrix ($\boldsymbol{S}$) is given by

$$\boldsymbol{S} = \begin{bmatrix} S_{hh} & S_{hv} \\ S_{vh} & S_{vv} \end{bmatrix}$$

(A.1)

To fully exploit the amplitude and phase characteristics of the polarimetric SAR scattering vectors, the 2 by 2 polarimetric scattering matrix ($\boldsymbol{S}$) can be converted to the second-order 3 by 3 coherency ($\boldsymbol{T}$) and covariance ($\boldsymbol{C}$) matrices by applying the Pauli spin target vector ($\boldsymbol{k}$) and the Lexicographic target vector ($\boldsymbol{\Omega}$), respectively, given by

$$\underline{\boldsymbol{k}} = \frac{1}{\sqrt{2}}[S_{hh} + S_{vv} \quad S_{hh} - S_{vv} \quad 2S_{hv}]^T$$

(A.2)

$$\underline{\boldsymbol{\Omega}} = \begin{bmatrix} S_{hh} & \sqrt{2}S_{hv} & S_{vv} \end{bmatrix}^T$$

(A.3)

$$\boldsymbol{T_3} = \langle \underline{\boldsymbol{k}} \cdot \underline{\boldsymbol{k}}^{*T} \rangle$$
$$= \frac{1}{2}\begin{bmatrix} \langle |S_{hh} + S_{vv}|^2 \rangle & \langle (S_{hh} + S_{vv})(S_{hh} - S_{vv})^* \rangle & 2\langle (S_{hh} + S_{vv}) S_{hv}{}^* \rangle \\ \langle (S_{hh} - S_{vv})(S_{hh} + S_{vv})^* \rangle & \langle |S_{hh} - S_{vv}|^2 \rangle & 2\langle (S_{hh} - S_{vv}) S_{hv}{}^* \rangle \\ 2\langle S_{hv}(S_{hh} + S_{vv})^* \rangle & 2\langle S_{hv}(S_{hh} - S_{vv})^* \rangle & 4\langle |S_{hv}|^2 \rangle \end{bmatrix}$$

(A.4)

$$\boldsymbol{C_3} = \langle \underline{\boldsymbol{\Omega}} \cdot \underline{\boldsymbol{\Omega}}^{*T} \rangle = \begin{bmatrix} \langle |S_{hh}|^2 \rangle & \sqrt{2}\langle S_{hh} S_{hv}{}^* \rangle & \langle S_{hh} S_{vv}{}^* \rangle \\ \sqrt{2}\langle S_{hv} S_{hh}{}^* \rangle & 2\langle |S_{hv}|^2 \rangle & \sqrt{2}\langle S_{hv} S_{vv}{}^* \rangle \\ \langle S_{vv} S_{hh}{}^* \rangle & \sqrt{2}\langle S_{vv} S_{hv}{}^* \rangle & \langle |S_{vv}|^2 \rangle \end{bmatrix} \tag{A.5}$$

where $\langle ... \rangle$ denotes spatial averaging and the reciprocity theorem assuming the symmetrical reflection in the monostatic backscattering (i.e., $S_{hv} = S_{vh}$) was applied (Lee and Pottier, 2009). A number of parameters from the coherency and covariance matrices are used to examine the correlation between the polarizations and the polarimetric nature of a target and applied for various polarimetric techniques including polarimetric decomposition and eigenvector and eigenvalue analysis (Lee and Pottier, 2009).

Appendix B. Polarimetric SAR decomposition

Polarimetric SAR can decompose target surfaces into different scattering mechanisms depending on the physical structure of scatterers and their distinct polarimetric nature, which is called polarimetric SAR target decomposition (Lee and Pottier, 2009). There are 2- or 4-component decomposition theorems, but 3-component (i.e., single-bounce surface scattering, double-bounce dihedral scattering, and multiple-diffused volume scattering) decompositions are commonly used. Here Pauli, Freeman-Durden, and Entropy-Anisotropy-Alpha angle decompositions are introduced.

1. Pauli decomposition

The Pauli decomposition reconstructs the scattering matrix $\boldsymbol{S}$ with the Pauli spin matrix basis as follows,

$$\boldsymbol{S} = \begin{bmatrix} S_{hh} & S_{hv} \\ S_{vh} & S_{vv} \end{bmatrix} = \frac{a}{\sqrt{2}}\begin{bmatrix} 1 & 0 \\ 0 & 1 \end{bmatrix} + \frac{b}{\sqrt{2}}\begin{bmatrix} 1 & 0 \\ 0 & -1 \end{bmatrix} + \frac{c}{\sqrt{2}}\begin{bmatrix} 0 & 1 \\ 1 & 0 \end{bmatrix} + \frac{d}{\sqrt{2}}\begin{bmatrix} 0 & -i \\ i & 0 \end{bmatrix}$$

$$\text{with} \quad \mathrm{a} = \frac{S_{hh} + S_{vv}}{\sqrt{2}}, \mathrm{b} = \frac{S_{hh} - S_{vv}}{\sqrt{2}}, \qquad \mathrm{c} = \frac{S_{hv} + S_{vh}}{\sqrt{2}}, \qquad d = \mathrm{i}\frac{S_{hv} + S_{vh}}{\sqrt{2}}$$

(A. 6)

where a, b, and c represent the single-bounce scattering characterized by $S_{hh} \approx S_{vv}$, the double-bounce scattering characterized by $S_{hh} = -S_{vv}$ due to the π phase difference between S_{hh} and S_{vv} from the dihedral reflection, and the multiple scattering characterized by the cross polarized component, S_{hv}, respectively (Cloude and Pottier, 1996). The total power (P) is described by the sum of each scattering power as follows,

$$\mathrm{P} = |S_{hh}|^2 + |S_{vv}|^2 + 2|S_{hv}|^2 = |a|^2 + |b|^2 + |c|^2 \tag{A.7}$$

2. Freeman-Durden decomposition

The Freeman-Durden decomposition describes the single-bounce surface scattering (Fig. A.1) by the first-order Bragg scattering matrix given by

$$\boldsymbol{S}_{single} = \begin{bmatrix} R_h & 0 \\ 0 & R_v \end{bmatrix}$$

$$R_h = \frac{cos\theta - \sqrt{\varepsilon - sin^2\theta}}{cos\theta + \sqrt{\varepsilon - sin^2\theta}}, \quad R_v = \frac{(\varepsilon - 1)\{sin^2\theta - \varepsilon(1 + sin^2\theta)\}}{\left(\varepsilon cos\theta + \sqrt{\varepsilon - sin^2\theta}\right)^2}$$

(A.8)

where R_h and R_v are the Bragg scattering coefficients for horizontal and vertical polarizations, respectively (Freeman et al., 1998). ε is the dielectric constant of a target surface, θ is the incidence angle of a radar sensor. The 2 by 2 scattering matrix can be described in the form of the covariance matrix as follows,

$$\boldsymbol{C}_{\boldsymbol{3}_{single}} = \begin{bmatrix} |R_h|^2 & 0 & R_h {R_v}^* \\ 0 & 0 & 0 \\ R_v {R_h}^* & 0 & |R_v|^2 \end{bmatrix} = f_s \begin{bmatrix} |\beta|^2 & 0 & \beta \\ 0 & 0 & 0 \\ \beta^* & 0 & 1 \end{bmatrix}$$

$$\text{with} \quad f_s = |R_v|^2, \quad \beta = \frac{R_h}{R_v}$$

(A. 9)

The double-bounce scattering is modeled based on a ground-tree trunk scatterer with two different dielectric properties (Fig. A.1) as follows,

$$\boldsymbol{S}_{double} = \begin{bmatrix} e^{2i\gamma h} R_{Th} R_{Gh} & 0 \\ 0 & e^{2i\gamma v} R_{Tv} R_{Gv} \end{bmatrix}$$

(A. 10)

where R_{Gh} and R_{Gv} are the horizontal ground reflection coefficients for horizontal and vertical polarizations, and R_{Th} and R_{Tv} are the vertical truck reflection coefficients for horizontal and vertical polarizations, respectively (Freeman et al., 1998). $e^{2i\gamma h}$ and $e^{2i\gamma v}$ are the radar attenuation effect terms for horizontal and vertical polarizations, respectively. Its covariance matrix is given by

$$\boldsymbol{C}_{\boldsymbol{3}_{double}} = \begin{bmatrix} |R_{Th} R_{Gh}|^2 & 0 & e^{2i(\gamma h - \gamma v)} R_{Th} R_{Gh} {R_{Tv}}^* {R_{Gv}}^* \\ 0 & 0 & 0 \\ e^{2i(\gamma h - \gamma v)} R_{Th} R_{Gh} {R_{Tv}}^* {R_{Gv}}^* & 0 & |R_{Tv} R_{Gv}|^2 \end{bmatrix}$$

$$= f_d \begin{bmatrix} |\alpha|^2 & 0 & \alpha \\ 0 & 0 & 0 \\ \alpha^* & 0 & 1 \end{bmatrix}$$

$$\text{with} \quad f_d = |R_{Tv} R_{Gv}|^2 , \quad \alpha = e^{2i(\gamma h - \gamma v)} \frac{R_{Th} R_{Gh}}{R_{Tv} R_{Gv}}$$

(A.11)

The volume scattering is modeled based on a cloud of cylinder-shaped dipole scatterers in random orientations (Fig. A.1) with the scattering matrix given by

$$\boldsymbol{S}_{volume} = \begin{bmatrix} a & 0 \\ 0 & b \end{bmatrix}_{a \gg b}$$

(A.12)

where a and b are the scattering coefficients in the length and width directions of a dipole scatter, respectively (Freeman et al., 1998). For a randomly oriented scatter, the scattering matrix is rotated by an orientation angle (ϕ) and given by

$$\boldsymbol{S}_{volume}(\emptyset) = \begin{bmatrix} cos\emptyset & sin\emptyset \\ -sin\emptyset & cos\emptyset \end{bmatrix} \begin{bmatrix} a & 0 \\ 0 & b \end{bmatrix} \begin{bmatrix} cos\emptyset & -sin\emptyset \\ sin\emptyset & cos\emptyset \end{bmatrix}$$

$$= \begin{bmatrix} acos^2\emptyset + bsin^2\emptyset & (b-a)sin\emptyset cos\emptyset \\ (b-a)sin\emptyset cos\emptyset & asin^2\emptyset + bcos^2\emptyset \end{bmatrix}$$

(A.13)

Assuming the probability density of the orientation angles to be uniform and very thin horizontal dipole scatters with a negligible width (i.e., b=0), the covariance matrix of the volume scattering component is simplified as follows

$$\boldsymbol{C_3}_{voulume} = \frac{f_v}{8} \begin{bmatrix} 3 & 0 & 1 \\ 0 & 2 & 0 \\ 1 & 0 & 3 \end{bmatrix} \quad \text{with } f_v = |a|^2$$

(A.14)

where f_v corresponds to the volume scattering portion of the total scattering components (Freeman et al., 1998).

Finally, the covariance matrix of the total scattering components is composed of the sum of the three scattering covariance matrices above and given by

$$\boldsymbol{C_3} = \boldsymbol{C_3}_{single} + \boldsymbol{C_3}_{double} + \boldsymbol{C_3}_{volume}$$

$$= \begin{bmatrix} \langle|S_{hh}|^2\rangle & \sqrt{2}\langle S_{hh}S_{hv}{}^*\rangle & \langle S_{hh}S_{vv}{}^*\rangle \\ \sqrt{2}\langle S_{hv}S_{hh}{}^*\rangle & 2\langle|S_{hv}|^2\rangle & \sqrt{2}\langle S_{hv}S_{vv}{}^*\rangle \\ \langle S_{vv}S_{hh}{}^*\rangle & \sqrt{2}\langle S_{vv}S_{hv}{}^*\rangle & \langle|S_{vv}|^2\rangle \end{bmatrix}$$

$$= \begin{bmatrix} f_s\beta^2 + f_d\alpha^2 + \frac{3}{8}f_v & 0 & f_s\beta + f_d\alpha + \frac{1}{8}f_v \\ 0 & \frac{2}{8}f_v & 0 \\ f_s\beta^* + f_d\alpha^* + \frac{1}{8}f_v & 0 & f_s + f_d + \frac{3}{8}f_v \end{bmatrix}$$

(A.15)

The covariance matrix leaves 4 equations with 5 unknown parameters. Here, an additional assumption is used to solve the problem. β is fixed at 1 if the double bounce scattering is dominant, while α is fixed at -1 if the surface scattering is dominant (Freeman et al., 1998). Then, the contribution of each scattering mechanism to the total power is defined as follows,

$$\mathrm{P} = |S_{hh}|^2 + |S_{vv}|^2 + 2|S_{hv}|^2 = P_s + P_d + P_v$$

$$\text{with} \quad P_s = f_s(1+\beta^2)\,, \quad P_d = f_d(1+\alpha^2)\,, \quad P_v = f_v$$

(A. 16)

where P_s, P_d, and P_v are the power of single-bounce, double-bounce, and volume scattering components, respectively (Freeman et al., 1998).

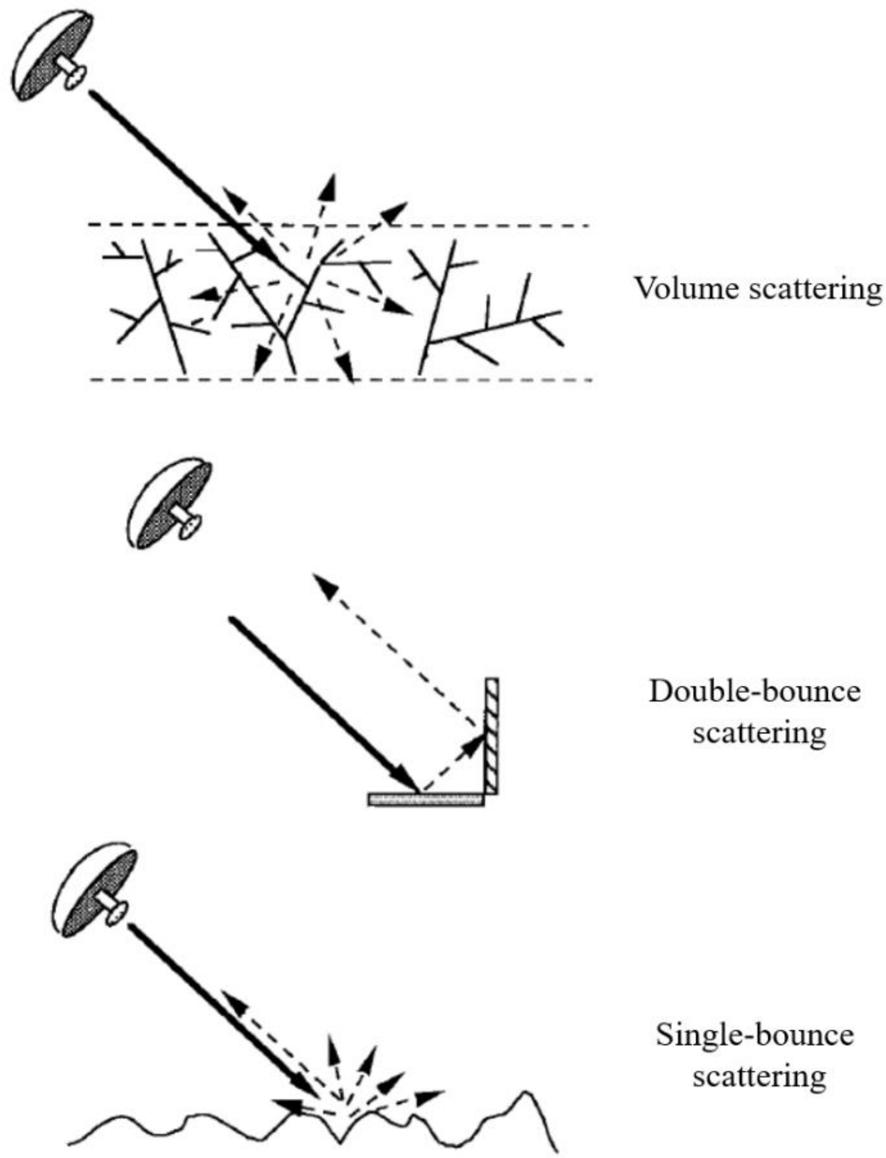

Figure A.1. Three scattering components of the Freeman-Durden decomposition (volume scattering from a canopy layer (top), double-bounce scattering from a dihedral surface (middle), and single-bounce scattering from a Bragg surface with small perturbations relative to a radar wavelength (bottom)). Figure from Freeman et al. (1998).

3. Entropy (H)-Anisotropy (A)-Alpha angle (α) decomposition

The H-A-α decomposition is based on the eigenvalues and eigenvectors of the coherency matrix. The 3 by 3 coherency matrix $\boldsymbol{T_3}$ can be decomposed into a diagonal matrix of eigenvalues and matrices of corresponding eigenvectors in the form of

$$\boldsymbol{T_3} = [U_3][\Lambda][U_3]^{-1}$$

$$\text{with} \qquad [\Lambda] = \begin{bmatrix} \lambda_1 & 0 & 0 \\ 0 & \lambda_2 & 0 \\ 0 & 0 & \lambda_3 \end{bmatrix}$$

$$[U_3] = [\underline{u}_1 \quad \underline{u}_2 \quad \underline{u}_3] = \begin{bmatrix} \cos\alpha_1 & \cos\alpha_2 & \cos\alpha_3 \\ \sin\alpha_1 \cos\beta_1 \, e^{i\delta_1} & \sin\alpha_2 \cos\beta_2 \, e^{i\delta_2} & \sin\alpha_3 \cos\beta_3 \, e^{i\delta_3} \\ \sin\alpha_1 \sin\beta_1 \, e^{i\gamma_1} & \sin\alpha_2 \cos\alpha_2 \, e^{i\gamma_2} & \sin\alpha_3 \cos\alpha_3 \, e^{i\gamma_3} \end{bmatrix}$$

(A.17)

where $[\Lambda]$ is the diagonal matrix of eigenvalues ($\lambda_1 > \lambda_2 > \lambda_3 > 0$) and $[U_3]$ is the unitary matrix of the orthogonal eigenvectors $\underline{u}_1$, $\underline{u}_2$, and $\underline{u}_3$ (Cloude and Pottier, 1997). Here, α_i is the alpha angle to determine the type of scattering mechanism, β_i is the beta angle related to the orientation of the target surface plane, and δ_i and γ_i are the delta and gamma angles related to phase, respectively (Cloude and Pottier, 1997). Based on the eigenvalues, the entropy and the anisotropy of polarimetric scattering are defined as follows,

$$H = -\sum_{1}^{3} p_i \log_3 p_i \qquad \text{with} \quad p_i = \frac{\lambda_i}{\lambda_1 + \lambda_2 + \lambda_3}$$

(A. 18)

$$A = \frac{p_2 - p_3}{p_2 + p_3}$$

(A.19)

where p_i represents the scattering probability based on the portion of each eigenvalue (Cloude and Pottier, 1997). The entropy (*H*) represents the randomness of the scattering mechanisms ranging 0 to 1 (Cloude and Pottier, 1997). H approaches to 0 for a single dominant scattering, while it increases with more mixed scattering components. The anisotropy (A) is the normalized difference between the second and the third eigenvalues, which provides additional information on the relative strength of the secondary and the tertiary scattering components besides the primary scattering component (Cloude and Pottier, 1997). For example, *A* also approaches 0 for a single dominant scattering with *H*=0. For mixed scattering processes with higher *H*, higher *A* indicates a dominance of the secondary scattering relative to the tertiary scattering, while lower *A* indicates an equivalence of the secondary and the tertiary scatterings.

The mean alpha angle (α) is derived from eigenvectors as follows,

$$\alpha = p_1\alpha_1 + p_2\alpha_2 + p_3\alpha_3$$

(A.20)

α determines whether the scattering process is single-bounce, double-bounce, or multiple scattering (Cloude and Pottier, 1997). The single-bounce scattering corresponds to $\alpha \rightarrow 0°$, the double-bounce scattering corresponds to $\alpha \rightarrow 90°$, and the multiple scattering corresponds to $\alpha \rightarrow 45°$ (Cloude and Pottier, 1997).

Cloude and Pottier (1997) proposed the entropy-alpha unsupervised classification plane with a total of 9 zones by combining the characteristics of the entropy and the mean alpha angle (Fig. A.2).

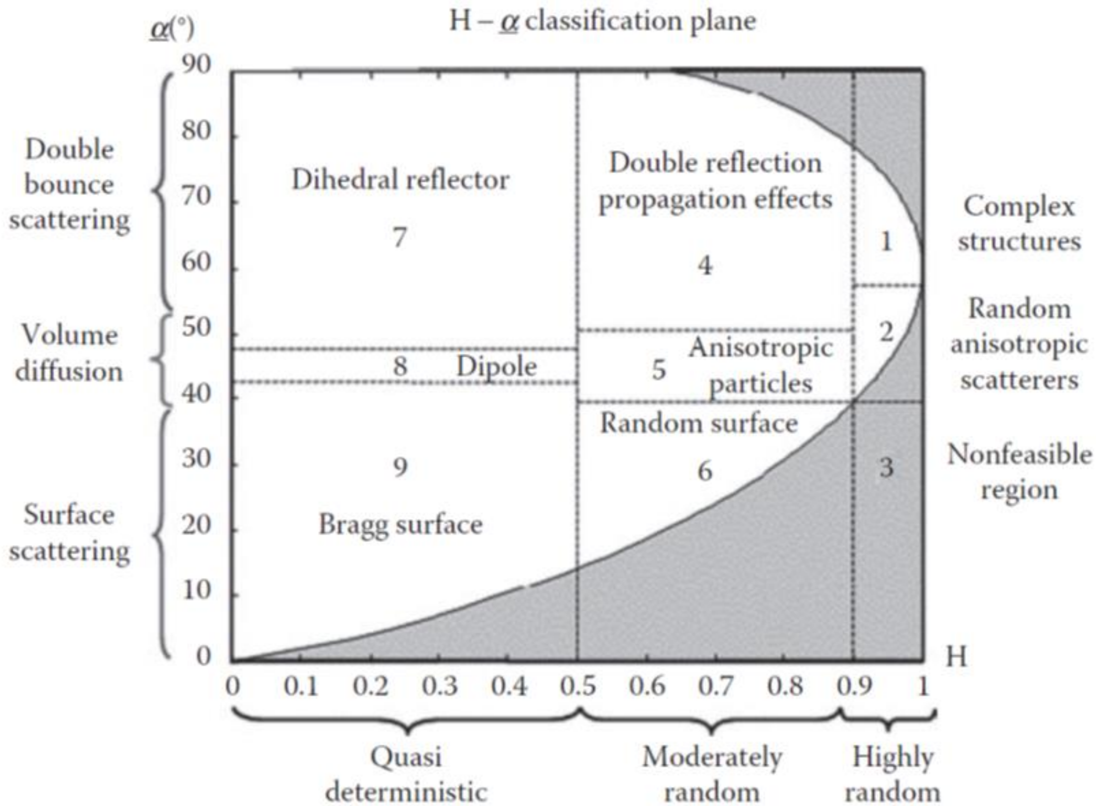

Figure A.2. Entropy (H)-Alpha angle (α) classification plane. Figure from Lee and Pottier (2009).

Appendix C. Integral Equation Method (IEM) scattering model

The IEM is a theoretical scattering model to calculate radar backscattering coefficients from randomly rough dielectric surfaces according to surface parameters (i.e., RMS height, correlation length, dielectric constant) and radar sensor parameters (i.e., radar frequency, polarization, incidence angle) based on an approximate solution of integral equations (Fung et al., 1992).

The IEM composes the backscattering coefficients with the single scattering and multi scattering terms given by

$$\sigma_{qp}^{0} = \sigma_{qp}^{S} + \sigma_{qp}^{M}$$

(A.21)

where σ_{qp}^{0}, σ_{qp}^{S}, and σ_{qp}^{M} are the total backscattering coefficient, single scattering coefficient, and multi scattering coefficient, respectively. p and q denote transmitting polarization and receiving polarization (=horizontal (h) or vertical (v)). Note that the contribution of the single scattering is zero for the cross-polarization backscattering coefficients (i.e., σ_{hv}^{0}, σ_{vh}^{0}), thus the cross-polarization backscattering coefficients is modeled by only the multiple scattering term (Fung et al., 1992).

The single scattering term is given by

$$\sigma_{qp}^{S} = \frac{k^2}{2}\exp\left(-2{k_z}^2 s^2\right)\sum_{n=1}^{\infty}\left|I_{qp}^{n}\right|^2 \frac{W^{(n)}(-2k_x, 0)}{n!}$$

(A.22)

where $k_z = kcos\theta$ and $k_x = ksin\theta$. θ is the incidence angle of a radar, k is the radar wavenumber, s is the root mean square (RMS) height of a target surface, $W^{(n)}$ is the Fourier transform of the n^{th} power of the surface autocorrelation function (Fung et al., 1992).

I_{qp}^{n} is the function of the RMS height and dielectric properties given by

$$I_{qp}^{n} = (2k_z s)^n f_{qp} \exp\left(-{k_z}^2 s^2\right) + \frac{(k_z s)^n \left[F_{qp}(-k_x, 0) + F_{qp}(k_x, 0)\right]}{2}$$

with

$$R_h = \frac{\mu cos\theta - \sqrt{\mu\varepsilon - sin^2\theta}}{\mu cos\theta + \sqrt{\mu\varepsilon - sin^2\theta}}, \quad R_v = \frac{\varepsilon cos\theta - \sqrt{\mu\varepsilon - sin^2\theta}}{\varepsilon cos\theta + \sqrt{\mu\varepsilon - sin^2\theta}}$$

$$f_{hh} = \frac{-2R_h}{cos\theta}, \quad f_{vv} = \frac{2R_v}{cos\theta}$$

$$F_{hh}(-k_x, 0) + F_{hh}(k_x, 0) = \frac{2\sin^2\theta\,(1 + R_h)^2}{cos\theta}\left[\left(1 - \frac{1}{\mu}\right) + \frac{\mu\varepsilon - \sin^2\theta - \mu\cos^2\theta}{\mu^2\cos^2\theta}\right]$$

$$F_{vv}(-k_x, 0) + F_{vv}(k_x, 0) = \frac{2\sin^2\theta\,(1 + R_v)^2}{cos\theta}\left[\left(1 - \frac{1}{\varepsilon}\right) + \frac{\mu\varepsilon - \sin^2\theta - \varepsilon\cos^2\theta}{\varepsilon^2\cos^2\theta}\right]$$

(A.23)

where R_h and R_v are the Fresnel reflection coefficients for horizontal and vertical polarizations, respectively. ε is the relative dielectric constant and μ is the relative permeability. f_{qp} is the Kirchhoff tangential field coefficient and F_{qp} is its complementary tangential coefficient (Fung et al., 1992; Fung and Chen, 2004).

The surface autocorrelation function $W^{(n)}$ applying the generalized power law spectrum is given by

$$W^{(n)}(-2k_x,0)=\frac{\left(\frac{l}{n^{f_p}}\right)^2}{2}(p-1)\frac{{a_p}^2}{{b_p}^2}\left[1+\frac{{a_p}^2}{{b_p}^2}\frac{(-2k_x)^2\left(\frac{l}{n^{f_p}}\right)^2}{4}\right]^{-p}$$

$$\text{with} \qquad f_p=0.5\left[1+\left(\frac{1.5}{p}\right)^2\right]$$

(A.24)

where l is the correlation length derived from the surface autocorrelation function, which is one of the surface roughness parameters. p is the power index of the generalized power law spectrum, and a_p and b_p are the p-dependant coefficients determined by the Gamma function and the Bessel function, respectively, to simulate various cases between the Gaussian autocorrelation function and the exponential autocorrelation function (Li et al., 2002). The multiple scattering terms is modeled by integrating two scattering vectors (u , v) in different directions to describe the different interactions from target surfaces equations (Fung et al., 1992), and given by

$$\sigma_{qp}^{M}=\frac{k^2}{16\pi}\exp\left(-2{k_z}^2s^2\right)\sum_{n=1}^{\infty}\sum_{m=1}^{\infty}\frac{\left({k_z}^2s^2\right)^{n+m}}{n!\,m!}$$

$$\cdot\int\left[\left|F_{qp}(u,v)\right|^2+F_{qp}(u,v)F_{qp}^{*}(u,v)\right]W^{(n)}(u-k_x,v)W^{(m)}(u+k_x,v)dudv$$

(A.25)

Appendix D. Extended-Bragg scattering model

The extended-Bragg model extends the range of the small perturbation model (SPM) by modelling induced roughness through rotational transformation of the coherency matrix of the Bragg scattering (A.11) given by

$$\boldsymbol{T_3} = \frac{1}{2}\begin{bmatrix} \langle |R_h + R_v|^2 \rangle & \langle (R_h - R_v)(R_h + R_v)^* \rangle & 0 \\ \langle (R_h + R_v)(R_h - R_v)^* \rangle & \langle |R_h - R_v|^2 \rangle & 0 \\ 0 & 0 & 0 \end{bmatrix}$$

$$\text{with} \quad R_h = \frac{cos\theta - \sqrt{\varepsilon - sin^2\theta}}{cos\theta + \sqrt{\varepsilon - sin^2\theta}}, \quad R_v = \frac{(\varepsilon - 1)\{sin^2\theta - \varepsilon(1 + sin^2\theta)\}}{\left(\varepsilon cos\theta + \sqrt{\varepsilon - sin^2\theta}\right)^2}$$

(A.26)

where R_h and R_v are the Bragg scattering coefficients for horizontal and vertical polarizations, respectively (Hajnsek et al., 2003). $\boldsymbol{\varepsilon}$ is the dielectric constant of a target surface, θ is the incidence angle of a radar sensor.

The coherency matrix rotated by an angle β is given by

$$\boldsymbol{T_3}(\beta) = [U(\beta)]^T \boldsymbol{T_3} [U(\beta)]$$

$$\text{with } [U(\beta)] = \begin{bmatrix} 1 & 0 & 0 \\ 0 & cos2\beta & -sin2\beta \\ 0 & sin2\beta & cos2\beta \end{bmatrix}$$

(A.27)

where β is the azimuthally oriented angle of a target surface (e.g., β_1=0 for Bragg surfaces) (Hajnsek et al., 2003, Fig. A.3).

Then, induced surface roughness is modeled by the distribution of β angles based on a probability density function

$$\boldsymbol{T_3} = \int_{\boldsymbol{0}}^{\boldsymbol{2\pi}} \boldsymbol{T_3}(\beta)P(\beta)d\beta$$

$$\text{with} \quad P(\beta) = \begin{cases} \dfrac{1}{2\beta_1} |\beta| \leq \beta_1 \\ 0 \leq \beta_1 \leq \dfrac{\pi}{2} \end{cases}$$

(A.28)

Here, $P(\beta)$ is the probability density function of β assuming a uniform distribution, and β_1 is the width of distribution of β angles (Hajnsek et al., 2003, Fig. A.3).

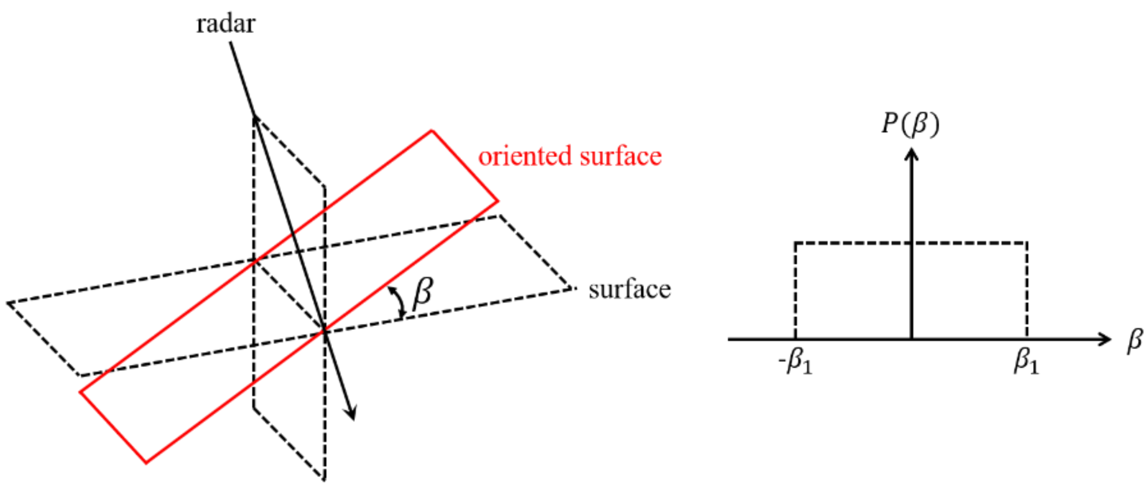

Figure A.3. Orientation angle of a target surface (β, left) and probability density function of β(right). Figure modified from Hajnsek et al. (2003).

Finally, the extended-Bragg coherency matrix is given by,

$$\boldsymbol{T}_{\boldsymbol{3\ Xbragg}} = \frac{1}{2}\begin{bmatrix} C_1 & C_2 sinc(2\beta_1) & 0 \\ C_2 sinc(2\beta_1) & C_3(1 + sinc(4\beta_1)) & 0 \\ 0 & 0 & C_3(1 + sinc(4\beta_1)) \end{bmatrix}$$

$$\text{with} \quad C_1 = |R_h + R_v|^2, \qquad C_2 = (R_h + R_v)(R_h - R_v)^*, \qquad C_3 = \frac{|R_h - R_v|^2}{2}$$

$$sinc(x) = \frac{\sin(x)}{x}$$

(A.29)

Based on the extended-Bragg coherency matrix, the eigenvalue-eigenvector parameters (i.e., entropy (*H*), anisotropy (*A*), alpha angle (α)) can be derived according to a range of surface roughness (β_1) and dielectric constants (ε) (Hajnsek et al., 2003). The *H*-*A*-α look up tables (LUTs) can be used to invert the surface parameters from SAR data (Fig.A.4). Hajnsek et al. (2003) also suggested an empirical formula between surface roughness (*ks*) and anisotropy (*A*) given by

$$ks = 1 - A$$

(A.30)

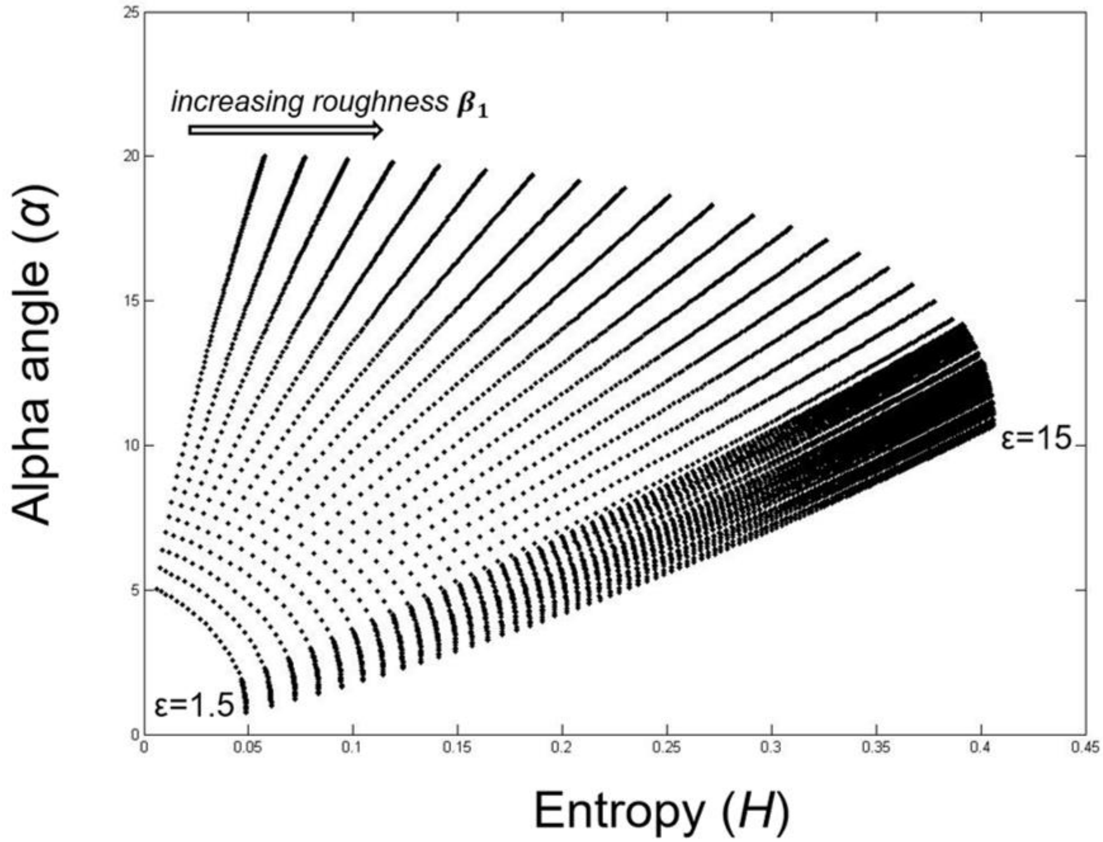

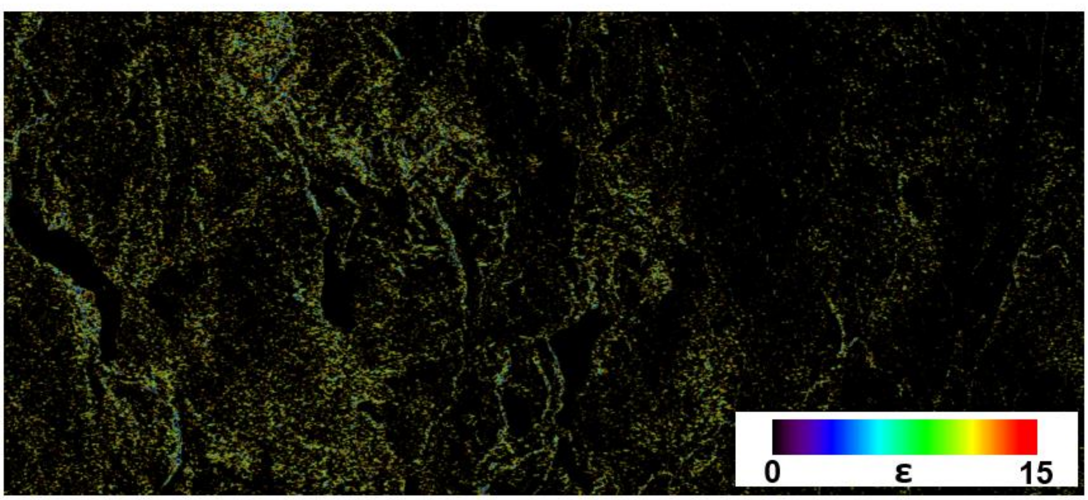

Figure A.4. Entropy (H)-alpha angle (α) look up table (LUT) according to a range of surface roughness (β_1: 5~90°) and dielectric constant (ε: 1.5~15) at 45° incidence angle (upper) and dielectric constant inversion map of the Tunnunik impact structure by the extended-Bragg model and RADARSAT-2 data (lower). Pixels with H >0.4 or α >20° out of the LUT range were masked out in black.

Appendix E. X-Ray Diffraction (XRD) analysis of the Tunnnik impact structure samples

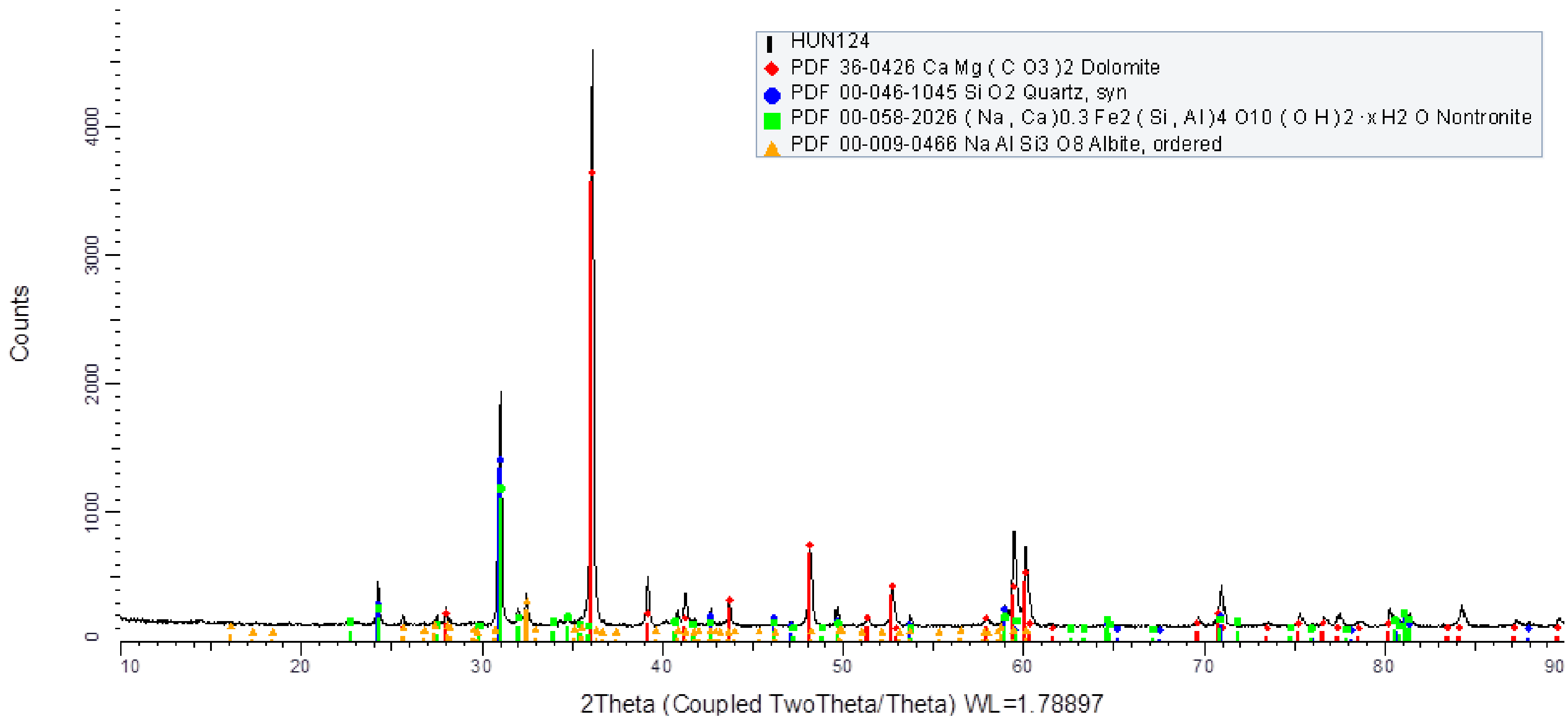

Figure A.5. XRD analysis (Sample HUN124 from Unit 1)

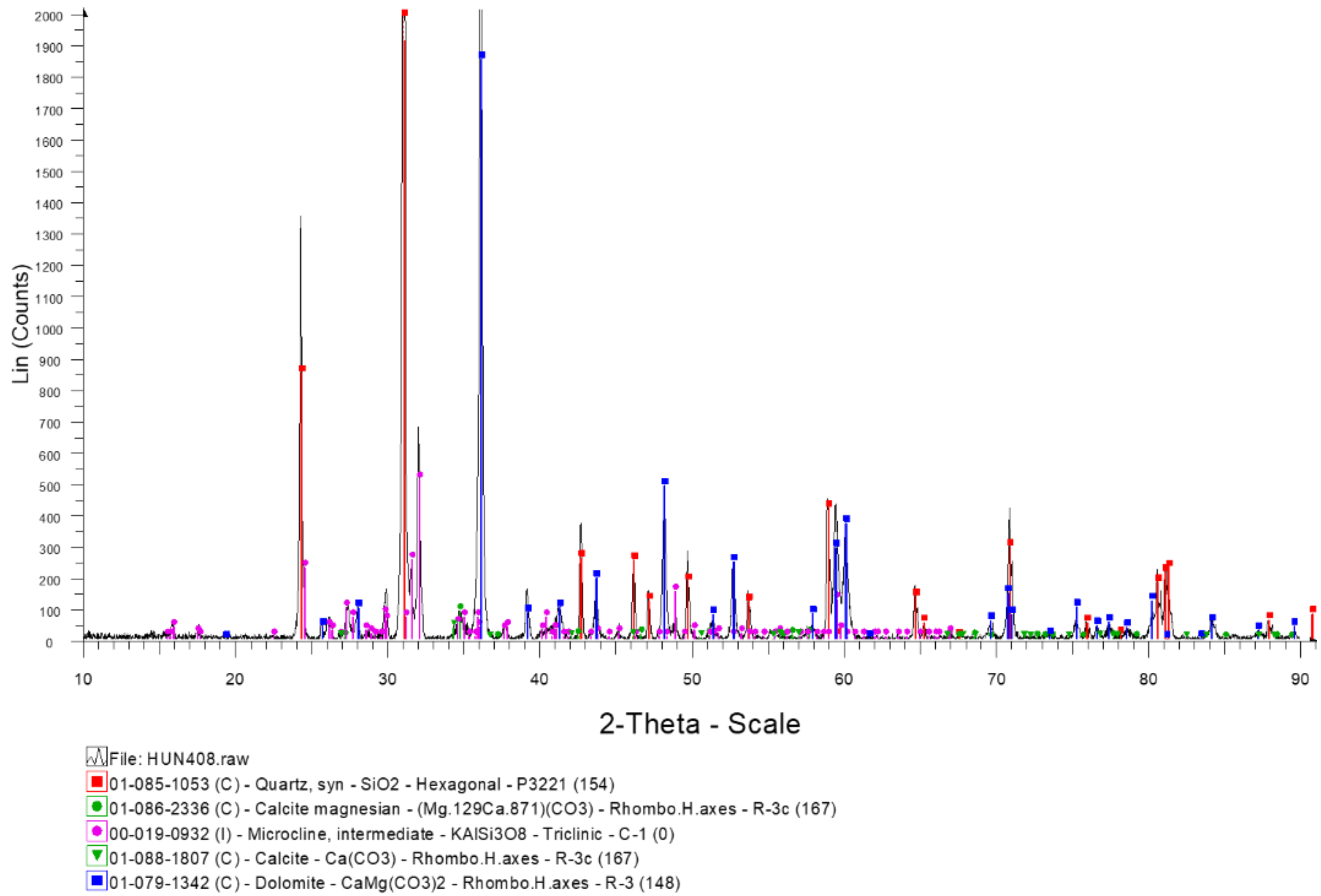

Figure A.6. XRD analysis (Sample HUN408 from Unit 2)

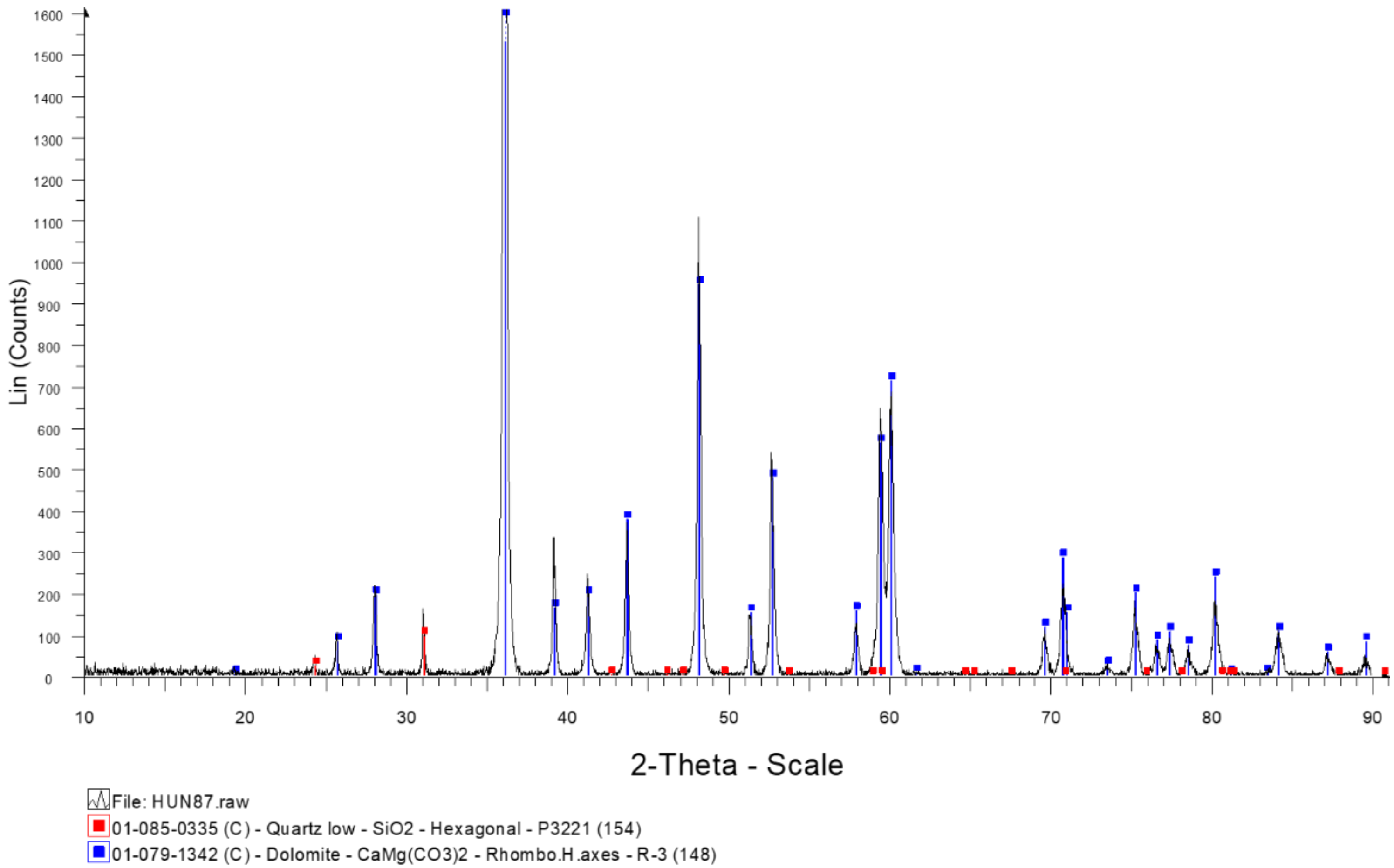

Figure A.7. XRD analysis (Sample HUN87 from Unit 3)

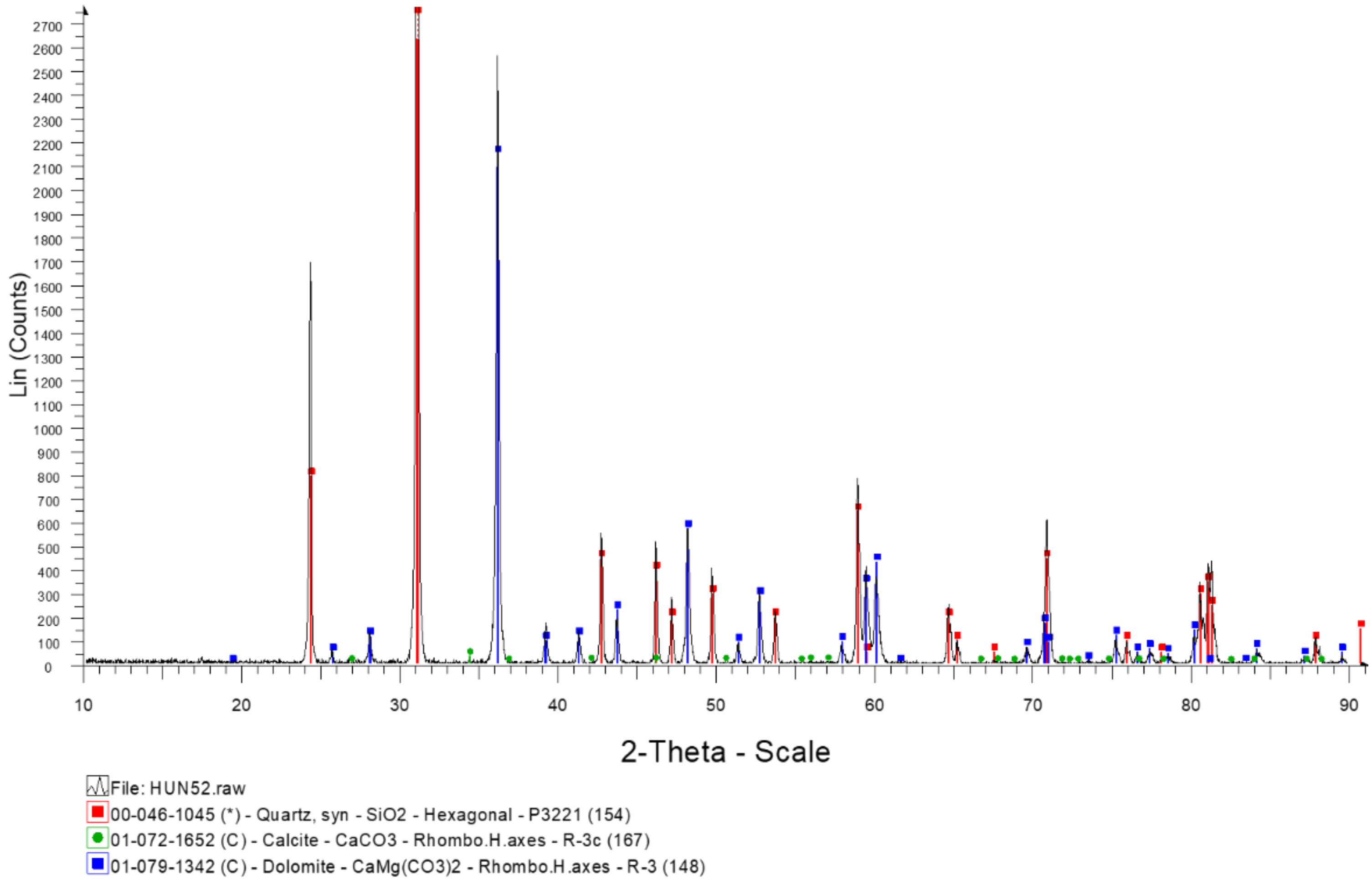

Figure A.8. XRD analysis (Sample HUN52 from Unit 4)

Appendix F. MATLAB code for a modified semi-empirical scattering model. Available in the attachment 'Choe_Oh_modified.m'.

Appendix G. MATLAB code for polarization signature plots. Available in the attachment ‘Choe_Polsignatures.m’.

References

Cloude, S.R., Pottier, E., 1997. An entropy based classification scheme for land applications of polarimetric SAR. IEEE Trans. Geosci. Remote Sens. 35, 68–78.

Cloude, S.R., Pottier, E., 1996. A review of target decomposition theorems in radar polarimetry. IEEE Trans. Geosci. Remote Sens. 34, 498–518.

Freeman, A., Member, S., Durden, S.L., 1998. A three-component scattering model for polarimetric SAR data. IEEE Trans. Geosci. Remote Sens. 36, 963–973.

Fung, A.K., Chen, K.S., 2004. An update on the IEM surface backscattering model. IEEE Geosci. Remote Sens. Lett. 1, 75–77. doi:10.1109/LGRS.2004.826564

Fung, A.K., Li, Z., Chen, K.S., 1992. Backscattering from a randomly rough dielectric surface. IEEE Trans. Geosci. Remote Sens. 30, 356–369. doi:10.1109/36.134085

Hajnsek, I., Cloude, S.R., Lek, J., Eric, P., 2003. Inversion of surface parameters from polarimetric SAR data 41, 1095–1097.

Lee, J.-S., Pottier, E., 2009. Polarimetric radar imaging: from basics to applications. CRC Press, New York.

Li, Q., Shi, J., Chen, K.S., 2002. A generalized power law spectrum and its applications to the backscattering of soil surfaces based on the integral equation model. IEEE Trans. Geosci. Remote Sens. 40, 271–280. doi:10.1109/36.992784

Curriculum Vitae

Name:	**BYUNG-HUN CHOE**
Post-secondary Education and Degrees:	The University of Western Ontario London, Ontario, Canada 2013-2017 Ph.D. in Geology and Planetary Science Seoul National University Seoul, South Korea 2009-2011 M.Sc. in Earth and Environmental Science Seoul National University Seoul, South Korea 1999-2006 B.Sc. in Earth Science Education
Honours and Awards:	Robert and Ruth Lumsden Graduate Fellowship in Science 2017 Northern Scientific Training Program (NSTP) research grant 2015, 2016 Ontario Graduate Scholarship (OGS) 2015-2016, 2016-2017 Queen Elizabeth II Graduate Scholarship 2014-2015
Related Work Experiences:	Research Assistant The University of Western Ontario 2016-2017 'Monitoring salt diapir evolution on Axel Heiberg Island with InSAR' funded by Canadian Space Agency 2015-2017 'Application of RASARSAT-2 polarimetric SAR for geological mapping and resource exploration in the Canadian Arctic' funded by Canadian Space Agency Teaching Assistant The University of Western Ontario 2013-2017

Publications:

Choe B.-H., Osinski G. R., Neish C. D. (*in preparation*) Polarimetric SAR signatures for characterizing geoloigical units in the Canadian Arctic. *IEEE Trans. Geosci. Remote Sensing.*

Choe B.-H., Osinski G. R., Neish C. D. (*in preparation*) A modified semi-empirical radar scattering model for weathered rock surfaces. *IEEE Trans. Geosci. Remote Sensing.*

Choe B.-H., Tornabene L. L., Osinski G. R., Newman J. D. (*in revision*) Remote predictive mapping of the Tunnunik impact structure in the Canadian Arctic using multispectral and polarimetric SAR data fusion. *Canadian Journal of Remote Sensing*.

Choe B.-H. and Kim D. (*accepted*) SAR remote sensing of intertidal flats in Korea. In Barale V. and Gade M. (Eds.) Remote sensing of the Asian Seas. Springer: Netherlands.

Choe B.-H., Kim D., Hwang J.-H., Oh Y., Moon W. M. (2012) Detection of oyster habitat in tidal flats using multi-frequency polarimetric SAR data. *Estuarine, Coastal and Shelf Science*, vol. 97, pp. 28-37.

Choe B.-H. and Kim D. (2011) Retrieval of surface parameters in tidal flats using radar backscattering model and multi-frequency SAR data. *Korean Journal of Remote Sensing*, vol. 27(3), pp. 225-234.

Conference presentations:

Choe B.-H., Osinski G. R., Neish C. D., Zanetti M., Tornabene L. L., Wang J. (2017) A multifrequency SAR study of the Haughton impact structure, Arctic Canada. *IEEE International Geoscience and Remote Sensing Symposium 2017 (IGARSS 2017)*. Fort Worth, Texas, USA (oral).

Choe B.-H., Osinski G. R., Neish C. D., Zanetti M., Tornabene L. L., Wang J. (2017) Surface roughness and polarimetric SAR signatures of geologic units in the Canadian Arctic. *11th Advanced SAR workshop.* Montreal, Quebec (oral).

Zanetti M., Neish C. D., Kukko A., **Choe B.-H.**, Osinski G. R., Harrington E., Mahathantila N. (2017) Polarimetric SAR signatures and kinematic LiDAR scanning surface roughness of periglacial patterned ground in the Canadian Arctic. *11th Advanced SAR workshop.* Montreal, Quebec, June 22-24, 2017 (oral).

Zanetti M., Neish C. D., Kukko A., **Choe B.-H.**, Osinski G. R., Harrington E., Mahathantila N. (2017) Surface roughness and radar scattering properties of periglacial terrain: geological application of personal mobile LiDAR scanning. *48th Lunar and Planetary Science Conference*, Houston, Texas, USA, March 20-24, 2017 (oral).

Choe B.-H., Neish C. D., Osinski G. R., Tornabene L. L., Zanetti M., Wang J. (2017) Characterizing geologic units in the Canadian Arctic using polarimetric SAR, *8th POLINSAR workshop.* European Space Agency-ESRIN, Italy (oral).

Harrington E., Neish C. D., **Choe B.-H.**, Shaposhnikova M., Zanetti M., Osinski G. R., Tiampo K. F., Samsonove S., Budkewitsch P., Zentilli M. (2016) InSAR investigations of salt diapir motion on Axel Heiberg Island, Canada. *American Geophysical Union (AGU) fall meeting.* San Francisco, USA, December 12-16, 2016 (oral).

Choe B.-H., Osinski G. R., Tornebene L. L. (2015) Surface properties of Arctic meteorite impact structures observed by RADARSAT-2 polarimetric SAR. *10th Advanced SAR workshop,* Saint-Hubert Canadian Space Agency, Quebec, Canada (oral).

Choe B.-H., Tornabene L. L., Osinski G. R. (2015) RADARSAT-2 and COSMO-SkyMed SAR investigation for geological mapping of the Tunnunik impact structure in the Canadian Arctic. *IEEE International Geoscience and Remote Sensing Symposium 2015 (IGARSS 2015)*, Milan, Italy (oral).

Choe B.-H., Tornabene L. L., Osinski G. R. (2014) Multispectral analysis of the Tunnunik impact structure in the Canadian Arctic using Landsat ETM 7+ and ASTER data (abstract #290). *Geological Association of Canada – Mineralogical Association of Canada (GAC-MAC) Annual Meeting*, Fredericton, New Brunswick, Canada (oral).

Choe B.-H., Tornabene L. L., Osinski G. R. (2014) Mineral and lithologic spectral mapping of the Tunnunik impact structure in the Canadian Arctic using Landsat ETM 7+ and ASTER data (abstract #2354). *45th Lunar and Planetary Science Conference*, Houston, Texas, USA (poster).

Kim D., **Choe B.-H.**, Moon W. M. (2013) Remote sensing of oyster reefs and groundwater discharge in coastal area using Synthetic Aperture Radar. *IEEE International Geosciece And Remote Sensing Symposium 2013 (IGARSS 2013*), Melbourne, Australia (oral).

Choe B.-H., Kim D., Hwang J.-H., Oh Y., Moon W. M. (2011) Oyster reef signature in tidal flats detected by multi-frequency polarimetric SAR data. *IEEE International Geosciece And Remote Sensing Symposium 2011 (IGARSS 2011*), Vancouver, British Columbia, Canada (oral).

Kim D., **Choe B.-H.**, Moon W. M., Park S.-E., Hwang J.-H., Oh Y. (2011) Detection of groundwater discharge and oyster reef in tidal flat using synthetic aperture radar. *TerraSAR-X Science Team meeting, Oberpfaffenhofen, Germany* (oral).

Choe B.-H., Kim D., Hwang J.-H., Oh Y., Moon W. M. (2011) Extraction of benthic fauna habitat in tidal flats using multi-frequency polarimetric SAR data. *POLINSAR workshop, European Space Agency, Frascati, Italy* (oral).

Choe B.-H., Kim D. (2010) Estimation of surface parameters in tidal flats using multi-frequency and multi-polarization SAR data. *Korean Society of Remote Sensing conference*, Incheon, Korea (oral, best student paper award).